INTEGRATING ROCK PHYSICS AND FLOW SIMULATION TO REDUCE UNCERTAINTIES IN SEISMIC RESERVOIR MONITORING

A DISSERTATION
SUBMITTED TO THE DEPARTMENT OF GEOPHYSICS
AND THE COMMITTEE ON GRADUATE STUDIES
OF STANFORD UNIVERSITY
IN PARTIAL FULFILLMENT OF THE REQUIREMENTS
FOR THE DEGREE OF
DOCTOR OF PHILOSOPHY

Madhumita Sengupta
June 2000

I certify that I have read this dissertation and that in my opinion it is fully adequate, in scope and quality, as a dissertation for the degree of Doctor of Philosophy.

Gary Mavko
(Principal Adviser)

I certify that I have read this dissertation and that in my opinion it is fully adequate, in scope and quality, as a dissertation for the degree of Doctor of Philosophy.

Amos Nur

I certify that I have read this dissertation and that in my opinion it is fully adequate, in scope and quality, as a dissertation for the degree of Doctor of Philosophy.

Jack Dvorkin

Approved for the University Committee on Graduate Studies:

Preface

The effect of pore fluids on seismic signatures has been known for years. However, over the last decade, with the increasing need to interpret seismic attributes for hydrocarbon detection and reservoir management, it has become most critical to reliably and accurately *quantify* not only the effects of pore fluids, but also the associated uncertainties. While the effect of fluid saturation on seismic velocities has been studied extensively, the effect of spatial *saturation scales* on seismic velocities is much less understood. Uncertainty in subresolution saturation scales introduce uncertainties in interpretation of seismic signatures in terms of fluid saturations. The goal of this thesis is to identify and quantify uncertainties in the seismic response of pore fluid properties and distributions, and to reduce these uncertainties by integrating traditional rock physics techniques with knowledge of reservoir fluid flow.

Gassmann's fluid substitution recipe is commonly used to predict velocities in saturated rocks. More often than not, at least some of the fluid substitution inputs are uncertain, owing to measurement errors, unavailability of data, and natural lithologic variation. We combine deterministic fluid substitution equations with stochastic Monte Carlo methods to assess uncertainties in the seismic velocity and Amplitude Variation with Offset (AVO) response due to uncertainties and inherent variability in rock and fluid properties. The question we address is: How sensitive are the predictions of seismic velocity and AVO to uncertainties in rock properties, fluid properties, and spatial fluid distributions?

The most striking fluid effect on seismic wave propagation occurs when gas appears in the subsurface. Flow simulators may predict the correct total mass of gas in a simulator block, but often do not correctly predict the seismically significant details such as the

saturation distribution within a simulator cell, or the relative amounts of free gas and dissolved gas. In this thesis, we identify the production scenarios where such uncertainties can significantly affect the seismic modeling and interpretation, and recommend strategies for dealing with such situations.

A coarse-scale, or patchy mix of fluids always has a higher P-wave velocity than a fine-scale, or uniform mix. Therefore, if we do not know the sub-seismic scales of fluid distribution, the question that arises is: When is the uniform saturation model appropriate, and when should we use the patchy saturation model? We use fine-scale flow simulations to constrain the sub-seismic scales of fluid distribution and identify the critical reservoir parameters that impact the sub-resolution saturation scales.

A very important conclusion of this thesis is that when gas is injected into oil-reservoirs, gravitational forces dominate, leading to the formation of sub-resolution gas-caps, and hence causing *patchy saturation* at field scales. On the other hand, we conclude that the *uniform* saturation model is appropriate for most waterfloods and for primary production scenarios when gas comes out of solution.

Another important result shows how knowledge of fluid *relative permeabilities* reduces the uncertainty in *seismic velocity*. We define a new upper bound, called *the modified patchy bound*, which uses residual saturations to narrow the bounds on seismic velocities of rocks with multiphase fluid saturations. This bound gives a much better approximation of the velocity-saturation response in cases of gas injection, and is also a valid upper bound for other production scenarios such as waterfloods and primary oil production leading to gas dissolution. Other factors that also affect the saturation scale, but to a lesser degree, are wettability of the rock, the mobility ratios of the fluids, and the permeability distribution in the reservoir.

We present a reservoir monitoring case study in which we interpret time-lapse offshore seismic data in terms of changes in the pore fluids. Seismic signatures of saturation changes definitely are sensitive to the saturation scales. *Downscaling* of smooth saturation outputs from the flow simulator to a more realistic patchy distribution was required to provide a good quantitative match with the near and far offset time-lapse data, even though the fine details in the saturation distribution were below seismic resolution. Of course, there are many issues in seismic acquisition, repeatability, and processing that impact amplitudes

and their interpretations. Nevertheless, the seismic response is significantly affected by the subresolution saturation heterogeneities. These heterogeneities can be estimated using well log data but are not present in the smooth flow simulator outputs.

Fine scale flow simulations help us to determine scales of saturation which are finer than the seismic resolution, while in the monitoring case study, the seismic response enables the estimation of saturation scales which are finer than the flow simulation blocks. This thesis demonstrates the feasibility of using seismic and well log data to constrain sub-block saturation scales, unobtainable from flow simulation alone. This important result has the potential to significantly impact and enhance the applicability of seismic data in reservoir monitoring. Interdisciplinary integration of *seismic* measurements and *rock physics* with multiphase *fluid flow* helps to reduce uncertainties in sub-resolution spatial fluid distributions, and as a result, reduces uncertainties in interpreting seismic attributes for reservoir management.

Acknowledgements

The work described in this thesis was funded by the Stanford Rock and Borehole Geophysics Project (SRB) and the Department of Energy (DOE). In the first two years, I was supported by Geophysics Department fellowships. Saga Petroleum provided the field data used in Chapter 4. I convey sincere thanks to the members of my dissertation reading committee: Gary Mavko, Amos Nur, and Jack Dvorkin, and to the members of my thesis defense committee: Jerry Harris, Biondo Biondi, and Jef Caers, for their valuable advice, comments, and feedback.

Gary's ideas have inspired this work, his guidance has steered it in the right direction, and his feedback has improved it. Gary is a brilliant teacher and the most wonderful adviser that any student can hope for. I have always considered myself extremely lucky to be his student. Gary is nothing remotely near the stereotypical adviser that features in grad student horror stories. He is of a very very rare class, the "nice adviser" class. Not only is he bright and smart and full of ideas (ok, maybe you expect that from advisers), but he is also kind, funny, considerate, and helpful (you don't expect that, do you?). Gary is one of the most entertaining as well as educative lecturers that I have come across at Stanford. TAing his class was also a fun experience. Even apart from academics, I could always rely on excellent advice from Gary and Barbara on diverse and complex important topics such as which car mechanics to trust, when to go house hunting, and where to gamble in Las Vegas. Gary, thanks for letting me take courses from other departments, for being so patient with my writing, and most of all, a zillion thanks for being such a cool adviser.

Amos, Gary, and Jack have made SRB a wonderful group to be in. Amos is remarkable not only because of his vision and insight, but also because in spite of being Department Chairperson, SRB Director, and adviser of so many graduate students, he always has time

to stop and say Hi to students, and is always encouraging and supportive. I am perpetually amazed at how quickly Amos can understand and appreciate any idea that I ever try to convey to him. Thanks to Jack for providing useful feedback whenever I needed it. I am grateful to Professor Martin Blunt and Marco Thiele for several vital dicussions on Petroleum Engineering concepts.

Margaret Muir keeps the SRB activities running like clockwork: everything from setting up new students in their offices, providing computer supplies, arranging annual meetings and making travel arrangements to organizing post-defense parties. She even magically produced acid-free thesis paper when the bookstore ran out of supply, just before the thesis submission deadline! Here in SRB, we all run to Margaret when we get into trouble and she always knows exactly what to do. Thanks a ton, Margaret, for your constant support, help, and advice. If you can find any clarity or crispness of language in this thesis, it is because of my editors, Ranie Lynds and Mary McDevitt, who practically rewrote my words and framed them into intelligible sentences. Thanks Ranie and Mary for all your help.

If Gary inspired me to build the framework of this thesis, it was Tapan Mukerji who helped me put every brick in place. Tapan has been my mentor and my prime source of motivation during all my years in Stanford. He got me started on my first research project, introduced me to Matlab, and constantly bugged me to be more productive. He has this terrible habit of always catching my mistakes (which I'd call approximations). Discussions with Tapan have often resulted in my having to redo all my research and regenerate all the figures. Thankfully, we had these discussions early enough so that I didn't have to rewrite all the conclusions! The most remarkable thing about discussing research problems with Tapan is that he always has time to discuss and suggest solutions to everybody's research problems which makes me wonder how (or if) he ever gets any of his own research done. Tapan always pointed me in the right direction whenever I got lost in my research or homework or ran into computer problems. In the last few months, he has reviewed drafts of my thesis chapters and provided many valuable suggestions. Tapan, thanks also for the cooking lessons and that once cup of coffee that I managed to extract from you in five years!

I greatly benefitted from collaborations with members of our industrial sponsors. I would like to acknowledge Ingrid Magnus, Jan Helgesen, and the other scientists at Saga

Petroleum who helped to put together the field data used in Chapter 4 of this thesis. Sincere thanks to Ingrid for useful discussions about the data and the problem, and for taking all the trouble. I am grateful to Chandra Rai and Carl Sondergeld of Amoco, who inspired and guided Chapter 2.3 of this thesis. I really enjoyed working with them in the summer of 1997.

I have been fortunate to have encountered some of the world's best teachers here at Stanford. Among the Professors whose lectures I've enjoyed the most were Professor Stuart of Mechanical Engineering who taught me Continuum Mechanics, Professors Henessey and Nishimura of Electrical Engineering, Professor Fox of Computer Science, and Professors Martin Blunt and Tom Hewett of Petroleum Engineering.

There is a long list of friends at Stanford who made my stay here enjoyable. I'll remember Manika Prasad not only for her terrible grilling session the day before my defence (the real grilling paled in comparison!) but also for the many barbecues and dinners at her place, and especially the SEG meetings where we'd share a room and then mess up the hotel billing. Of course, Margaret was always nice enough to clear it up for us. Manika is funny and helpful, and a wonderful person to have in SRB. Li Teng was my first officemate, and helped me with everything from settling down at Stanford and driving me to the supermarket, to designing interactive class web pages when we TAed Gary's course together. Thanks Li, for the awesome Chinese food, too! Per Avseth, Mario Gutierrez, Ran Bachrach, Sandra Vega, Wendy Wempe, and Diana Sava were among the graduate students in SRB with whom I had many interesting academic and non-academic discussions, Isao Takahashi helped me to locate Latex symbols, and Youngseuk Keehm helped a lot with computer problems. Many thanks to Arjun and Arpita for their help with Eclipse flow simulations, for being such wonderful friends, and for the numerous dinner invitations! Mamta, I'll remember the lunchtime *gup-shup*, the (long) coffee-breaks, and the Friday night SIA movies.

My family members have played a vital role in the completion of my Ph.D. My uncle Pabitra Sen convinced me to come to Stanford, and was supportive throughout my stay here. I cannot thank my cousin Madhuparna Roychoudhury and her family enough for providing all the moral support and encouragement when I most needed it. Behind every successful woman is a faithful husband...whatever little success I've had here in Stanford,

I owe a lot of it to Soovo. He not only helped me with algebra and homework assignments, he also cooked dinner for me and washed dishes for months, and never complained. Thanks also to my young-at-heart grandmother Uma Sen for her enthusiastic support of my Ph.D. endeavors. Finally, I want to mention my parents, who are the most important people in my life. Words cannot express my feelings for them. I owe everything to them, and there is no way I could have made it without their support. I dedicate this thesis to my mother and father, Bulbul and Provakar Sengupta. Thanks, Mom and Dad!

Contents

List of Tables

List of Figures

Chapter 1

INTRODUCTION

GOAL

The purpose of this thesis is to identify, quantify, and provide schemes to reduce uncertainties in fluid substitution for seismic hydrocarbon detection and reservoir monitoring.

Fluid substitution, the problem of predicting how seismic velocity and impedance depend on pore fluids, is a key step in seismic modeling and interpretation. The effect of pore fluids on the seismic response has been known for more than 40 years. However, quantifying pore fluid effects and their uncertainties has become most critical over the last decade, with the need to interpret seismic amplitudes for hydrocarbon detection and reservoir monitoring.

Rock properties (such as porosity, mineral modulus, and frame stiffness), fluid properties (such as fluid bulk modulus, density, and gas-oil-ratio), reservoir properties (such as temperature and pressure), and the scales of fluid distribution (fine-scale mix or coarse-scale mix) are all essential ingredients of the fluid substitution recipe. Errors in measurement or estimation of these properties often lead to uncertainties in the predicted seismic response. Uncertainties in the predicted velocity and impedance can also occur as a result of imperfections or approximations in the models. This thesis deals with the quantification of these uncertainties and recommends strategies for dealing with them.

BACKGROUND

Both laboratory and field measurements have illustrated the dependence of seismic velocities and impedance on pore fluids. Fluids affect the acoustic properties of rocks in mainly two ways. Pore fluids change the overall elastic moduli and seismic velocities of rocks, and also introduces velocity dispersion, i.e., dependence of velocity on the wave frequency. Several authors have proposed theoretical models to explain the fluid-related changes in the seismic behavior of rocks. This section presents a brief overview of the most widely used theoretical models, along with some key examples from laboratory and field studies.

When a less compressible fluid (such as brine) replaces a more compressible fluid (such as gas), the stiffer pore fluid resists wave-induced deformations and effectively makes the rock elastically stiffer. King (1966) and Nur and Simmons (1969) were among the earliest

authors to show laboratory measurements that demonstrated the effect of pore fluids on seismic velocities. More recently, Wang and Nur (1988) among many others reported laboratory experiments with reservoir fluids of different kinds that also show the dependence of seismic velocities on pore fluids.

The most well-known and frequently used model for predict fluid related changes in the seismic velocities of rocks is Gassmann's (1951) fluid substitution model. Gassmann proposed a low-frequency model for predicting the bulk and shear modulus of a saturated rock given the bulk and shear modulus of the dry rock. Gassmann's equations assume a homogeneous mineral modulus and statistical isotropy of the pore space, but are free of assumptions about the pore geometry.

Gassmann's equations are very often extended to include rocks with mixed mineralogies by using an effective average modulus such as the empirical Voigt-Reuss-Hill average modulus (Hill, 1952) in place of the mineral bulk modulus. Gassmann's equations require both V_P and V_S, while field applications often call for fluid substitution in the absence of shear wave velocity. Mavko, Chan and Mukerji (1995) suggested a method that uses an approximate version of Gassmann's relation to predict the compressional velocity of a saturated rock from the dry rock compressional velocity when the shear velocity is unknown. Empirical V_P/V_S relations can also be used (Greenberg and Castagna, 1992) to estimate the shear velocity for input to fluid substitution.

Several authors have extended Gassmann's equations to include cases when the rock is not isotropic or homogeneous. Brown and Korringa (1975) derived theoretical formulas relating the effective moduli of an anisotropic dry rock to the effective moduli of the same rock containing fluid. Berryman and Milton (1991) formulated a generalized Gassmann's equation, which describes the static or low-frequency effective bulk modulus of a fluid-filled porous medium composed of two phases, each of which could be described by the conventional Gassmann's equations. Like Gassmann's equations, the generalized Gassmann's formulation is independent of pore geometry and is applicable only at low frequencies (less than ≈ 100 Hz).

The quasi-static theories of Gassmann, Brown and Korringa etc. make the assumption that wave-induced pore pressures are equilibrated throughout the pore space. At high

frequencies, this assumption is not valid. Unequilibriated pore pressures give rise to velocity dispersion and attenuation. Numerous models have been proposed to describe the fluid-related dispersion.

Biot (1956) derived the now well-known theoretical formulas for predicting frequency dependent saturated rock velocities in terms of the dry rock properties. Geertsma and Smit (1961) made low- and middle-frequency approximations of Biot's theoretical results for predicting the frequency-dependent velocities of saturated rocks from the dry rock properties. The Biot model assumes that the rock is homogeneous and isotropic and that the fluid-bearing rock is fully saturated.

While Biot's theory takes into account global-scale pore-pressure variations and relative flow between solid and fluid, it does not account for local grain-scale unequilibriated pressures. Mavko and Nur (1975) and O´Connell and Budiansky (1977) introduced inclusion models to describe the high frequency limit of the "Squirt" or "local flow" phenomenon. At this high frequency limit, the inclusions are perfectly isolated with respect to fluid flow. These initial models were limited to assumptions of idealized geometry and small concentrations of inclusions.

Later, Mavko and Jizba (1991) derived a geometry independent squirt model for predicting the very high frequency moduli of saturated rocks in terms of the pressure dependence of dry rocks. This model is valid for all porosities. For most crustal rocks, the amount of squirt dispersion is comparable to or greater than Biot's dispersion, and, thus, using Biot's theory alone will lead to poor predictions of high-frequency saturated velocities, as shown experimentally by Winkler (1983). Mukerji and Mavko (1994) extended the squirt model to apply it to calculate high-frequency saturated rock velocities in anisotropic rocks.

The squirt models address only the very high frequency limit of squirt dispersion. The BISQ model (Dvorkin and Nur, 1993, Dvorkin et al., 1994) combined the Biot and squirt theories to model the full frequency dependence of velocity and attenuation in saturated rocks. The BISQ formulas can be used to calculate saturated rock velocity dispersion and attenuation. BISQ also assumes a homogeneous and isotropic rock.

The squirt or local flow dispersion is important at high frequencies (e.g., in case of laboratory measurements) but dispersion can also arise due to coarse-scale fluid distribution,

and this dispersion, often referred to as dispersion arising from "patchy saturation" can be important at seismic frequencies. This fluid effect was first theoretically modeled by White (White, 1975) and Dutta and Odé (Dutta and Odé, 1979). This thesis further analyses patchy behavior and shows strategies for reducing uncertainty arising from coarse-scale partial saturations.

The first-order low-frequency effects for single fluid phases are described quite well with Gassmann's (1951) relations. However, in most hydrocarbon detection problems, velocities of partially saturated rocks with mixed fluid phases in the pore-space need to be predicted. A very common approach to modeling partial saturation or mixed fluid saturations is to replace the collection of phases in the pore with a single "effective fluid" into Gassmann's equations. This approach has been discussed by Domenico (1976), Murphy (1984), Mavko and Nolen-Hoeksema (1994), Cadoret (1993), and many others. Experimental observations by Murphy (1984) show that the effective fluid model is applicable in some situations.

Since the Gassmann theory assumes a state of equilibrated pore pressure throughout the rock, the effective fluid model is valid only when all of the fluid phases are mixed at a very fine scale, smaller than a critical relaxation scale (Mavko et al., 1998). In 1993, Cadoret made low frequency measurements of partially saturated rocks during drainage (drying) and imbibition (wetting). During imbibition, the fluids were mixed at a fine scale in the rock, while during drainage, the fluids were mixed at a coarse scale. Velocity data collected during imbibition were found to be in excellent agreement with the fine-scale effective fluid model. During drainage, higher velocities were observed, indicating that the effective fluid model did not work when the fluid phases are mixed at scales larger than the characteristic diffusion length (also known as the critical relaxation scale).

When the saturation scales are larger than the characteristic diffusion length, the seismic velocity can be modeled by the patchy saturation model (Cadoret, 1993, Knight et al., 1995, Mavko and Mukerji, 1998). This thesis explores the applicability of the effective fluid model (also known as the fine-scale uniform saturation model) and the patchy saturation model (applicable at coarse saturation scales) at seismic frequencies. We try to distinguish production scenarios in which the scales of fluid saturation are small enough to be effectively modeled by the uniform saturation model, versus scenarios in which the saturation

scales are large enough to require patchy saturation modeling. We use fine-scale reservoir flow simulations to determine the sub-seismic resolution scales of fluid distribution. We try to determine which reservoir parameters have the largest impact on sub-resolution saturation scales.

In production scenarios, repeat seismic monitoring is an increasingly powerful technique that can effectively map subsurface fluid flow, and separate fluid effects from lithologic or other effects. Barr (1973) introduced the idea of seismically monitoring subsurface changes in fluid properties due to injection of waste materials in disposal wells. He based the proposal on changes in the reflection coefficient that would arise as a result of fluid substitution. Nur (1982) proposed the use of repeat seismic surveys to monitor the process of enhanced oil recovery, specifically during steam injection, to recover heavy oil. Since then, several case studies have been reported in which time-lapse seismic surveys were conducted to successfully monitor subsurface fluid changes (Greaves and Fulp, 1987, Pullin et al., 1987, Eastwood et al., 1994, Johnston et al., 1998).

So far, many of the interpretation of time-lapse data have been qualitative before-after comparisons. For quantitative interpretation of time-lapse seismic, a key requirement is understanding of multi-phase fluid flow and spatial saturation distributions. Therefore, this thesis integrates reservoir flow simulation with rock physics models to compute and interpret time-lapse seismic signatures. The next section gives an overview of the chapters in this thesis.

OVERVIEW OF CHAPTERS

In Chapter 2, we quantify the sensitivity of fluid substitution to uncertainties in rock properties (porosity, mineral modulus, and frame stiffness) and fluid properties (bulk modulus, density, and gas-oil-ratio). We quantify the uncertainties in seismic velocities and AVO response to uncertainties in these rock and fluid parameters. Material from this chapter was presented at SEG meetings (Sengupta et al., 1998, Sengupta and Mavko, 1999). In Chapter 3, we address the problem of uncertainty in spatial distribution of fluids. We integrate fine-scale flow simulations with the fluid substitution recipe to determine which fluid flow parameters control the sub-resolution saturation scales. Results from this chapter

were presented at the AGU meetings of 1996 and 1997 and in the SEG meeting in 1998 (Sengupta et al., 1996, Sengupta and Mavko, 1997, Sengupta and Mavko, 1998). In Chapter 4, we present a reservoir monitoring case study in which time-lapse near and far offset data were collected to monitor subsurface fluid flow. In this chapter, we combine flow simulator predictions of saturation with estimation of saturation scales from well logs to interpret the time-lapse seismic data. This chapter will be presented at the SEG meeting in 2000 (Sengupta et al., 2000).

Chapter 2 addresses the sensitivity of seismic velocities to uncertainties in fluid properties. Fluid substitution is a key step in seismic hydrocarbon detection. More often than not, at least some of the fluid substitution inputs are uncertain, owing to measurement errors, unavailability of data, and natural lithologic variation. We quantify uncertainties in seismic signatures predicted by fluid substitution resulting from uncertainties in rock and fluid properties. Chapter 2.1 deals with Gassmann's fluid substitution recipe, which is the most popular and commonly used tool for predicting seismic velocities in fluid saturated rocks. We quantify the sensitivity of the predicted velocity to uncertainties in the input rock and fluid properties, i.e., the V_P, V_S, and density (ρ) of the rock saturated with the original fluid, the mineral bulk modulus (K_0), the porosity (ϕ), the bulk modulus (K_{f1}) and density (ρ_{f1}) of the original fluid, and the bulk modulus (K_{f2}) and density (ρ_{f2}) of the new fluid.

In this study, we define a sensitivity factor, E_i, as the ratio of the fractional error in the predicted V_P to the fractional error in each input parameter. Our study shows that fluid-substitution predictions of V_P are most sensitive to the original V_P, with E_i between 1 and 5. The sensitivity of the predicted V_P to the original V_S, porosity, and mineral bulk modulus are much lower, with E_i between 0.1 and 0.5. The sensitivity of the predicted V_P to the bulk modulus and density of water and oil is also low, with E_i between 0.1 and 0.5. The sensitivity to the bulk modulus and density of gas is extremely low, with E_i always below 10^{-3}. However, the inputs that can potentially have the largest uncertainties are the bulk moduli and density of the pore fluids, because their values change a lot with reservoir conditions, such as pressure, temperature, and partial saturation. Chapter 2.2 quantifies the uncertainties in the fluid properties due to various changes in the reservoir and studies the resultant effect on seismic velocities.

The most striking fluid effects occur when gas appears in the subsurface. Gas injection

can increase the pore pressures, and as a result, some of the injected gas may dissolve in the oil, thus increasing the gas-oil-ratio (GOR), and making the oil more compressible. Reservoir pressures often drop due to oil production, causing gas to come out of solution. Such changes in free gas saturation and GOR may not be modeled correctly by flow simulators, but they do affect seismic velocities, as shown in Chapter 2.2.

Our study presented in Chapter 2.2 shows that for a given mass of gas, a rock containing free gas always has a lower velocity than the same rock containing only dissolved gas if the oil and gas are mixed at a very fine scale. For a fine-scale mix of oil and gas, the seismic velocity is dominated by the free gas saturation, and the oil gravity and GOR have a negligible effect on the velocity. When gas comes out of solution, we expect it to form bubbles in the oil, i.e., a fine-scale mix (Chapter 3.2). We therefore conclude that gas dissolution always leads to significant reduction in the seismic velocity.

However, in the case of a coarse-scale or patchy mix of oil and gas, the rock containing free gas may have slightly higher or lower seismic velocities than the rock containing dissolved gas, depending on the dry rock stiffness, the porosity, and the oil gravity. We expect a patchy mix when gas in injected into oil (Chapter 2). Therefore, we conclude that if some of the injected gas dissolved into oil, we should not expect significant changes in the seismic velocity.

Chapter 2.2 also shows that that soft rocks are seismically more sensitive than stiff rocks for distinguishing free gas (gas-oil mix) from dissolved gas (gas-oil solution). In the absence of free gas, rocks saturated with heavier oils show higher seismic velocities than rocks saturated with lighter oils. The seismic difference between a dead oil and a live oil at a given GOR (e.g. GOR = 50) is larger for a heavy oil than for a live oil, because, heavy oils, being much heavier and stiffer than gas, show a higher sensitivity to dissolved gas for a given value of GOR. However, the seismic difference between a dead oil and a fully saturated oil (with GOR = GOR_{max}) is larger for a light oil than for a heavy oil, because light oils can dissolve more gas than heavier oils.

The impact of pore fluids on seismic velocities makes it interesting for reservoir exploration and development. However, applying these theories to field or production scenarios involves several challenges. Seismic velocities are not only affected by fluids, but also by variations in lithology, porosity, clay, sorting etc, which can mask fluid effects

and introduce non-uniqueness in interpretation of seismic signatures. One of the popular and powerful techniques of separating fluid effects from other effects is the combined use of P and S wave velocities, such as in Amplitude Variation with Offset (AVO) techniques (Rutherford and Williams, 1989, Castagna et al., 1993, Castagna and Swan, 1997, Hilterman, 1998). Chapter 2.3 discusses uncertainties in AVO attributes, i.e., normal incidence reflectivity and the AVO gradient as a result of uncertainties in rock and fluid properties.

Using a Monte Carlo approach, we quantify the uncertainty in the Amplitude Variation with Offset (AVO) response which results from uncertainties in rock and fluid properties. We can apply this methodology in assessing the merits of AVO analysis or even acquiring offset data to address problems constrained by knowledge of the rock physics of the local environment. Our studies show that the uncertainty in the AVO response increases with decreasing rock stiffness. Although AVO anomalies are typically associated with lithology or fluid changes, we find that anisotropy can create or destroy AVO anomalies.

In **Chapter 3** we address the problem of uncertainties in seismic velocities due to variation in heterogeneous scales of saturation. Partially saturated rocks show higher velocities if the fluids are mixed at coarse scales than if the fluids are mixed together at very fine scales.

We investigate the effect of saturation scales on reflection properties using the Kennett algorithm to compute synthetic seismograms for 1-D layered media. We identify three saturation scales, (a) larger than the seismic wavelength (i.e. resolvable), (b) smaller than the seismic wavelength but larger than the characteristic diffusion length, and (c) smaller than the characteristic diffusion length. When the saturation scale is in the range (a), the seismic velocity and reflectivity can be modeled by the ray-theory equations. In case (b), we can model the velocity and amplitude using effective medium theory. Case (b) is known as the patchy saturation model. For case (c), the seismic velocity and reflectivity can be computed using the effective fluid model, and this is known as the uniform saturation model.

In Chapter 3.2, we explore applicability of the uniform and patchy saturation models at seismic frequencies. We try to distinguish production scenarios in which the scales of fluid saturation are small enough to be effectively modeled by the uniform saturation model,

versus scenarios in which the saturation scales are large enough to require patchy saturation modeling. We use fine-scale reservoir flow simulations to determine the sub-seismic resolution scales of fluid distribution. We try to determine which reservoir parameters have the largest impact on sub-resolution saturation scales.

Flow simulations have helped us to understand which reservoir parameters control the scales of saturation. Patchy saturation has been mostly verified in laboratory measurements, and in well logs. Our study shows that we can also expect patchy behavior at the seismic scale. This chapter's most important conclusion is that when gas is injected into oil-reservoirs, gravitational forces dominate, leading to the formation of sub-resolution gas-caps and hence causing patchy saturation at field scales. In this chapter, we also conclude that the uniform saturation model is appropriate for most waterfloods and for primary production scenarios when gas comes out of solution.

Another important conclusion is that knowing the relative permeabilities of the fluid components in the reservoir narrows the uncertainty in saturation scales by a large amount. The values of the residual saturation from the relative permeability curves can be used to modify the upper patchy bound so that it lies closer to the lower bound. The residual saturation thus constrains the seismic velocity. We call the new upper bound the modified patchy bound. This bound gives a much better approximation of the velocity-saturation response in cases of gas injection, and is also a valid upper bound for waterfloods and other production scenarios, for the respective values of residual saturation. Other factors that also affect the saturation scale, but to a smaller degree, are wettability of the rock, the mobility ratios of the fluids, and the permeability distribution in the reservoir.

In **Chapter 4**, we present a reservoir monitoring case study from the North Sea, in which we interpret time-lapse seismic data in terms of changes in the pore fluids. Our goals in this study, as in most time-lapse studies, were to link flow simulation and seismic, and to map production-related saturation changes.

Using real field data, Chapter 4 shows that the sub-resolution spatial distribution of fluids can impact the seismic response. Although there is a good qualitative match between the fluid changes predicted by the flow simulator and the fluid changes interpreted from the seismic, the simulator predicts very smooth saturation profiles, which do not quantitatively match the time-lapse seismic changes. We find that downscaling the simulator outputs

yields a much better quantitative match to the seismic. We downscaled the smooth saturations from the simulator by incorporating high spatial frequencies from the well logs, while constraining it to the total mass balance predicted by the flow simulator and varying only the vertical spatial distribution. This downscaling gave an estimate of the patchy saturation profile. The computed seismic response of the downscaled (patchy) saturation distributions matched the real time-lapse seismic much better than the (smooth) saturation distributions taken directly from the simulator.

Fluid substitution, i.e., predicting seismic signatures of saturation changes, definitely is sensitive to the saturation scales. In this exercise we found that downscaling of smooth saturation outputs obtained from the flow simulator was required to provide a good quantitative match to the near and far offset time-lapse data, even though the the fine details in the saturation distribution were below seismic resolution, and below the resolution of the simulator blocks. Of course, there are many issues in seismic acquisition and processing that impact amplitudes in and their interpretations. Nevertheless, the seismic response is significantly affected by the subresolution saturation heterogeneities which can be estimated from well logs but are not present in the unrealistically smooth flow simulator outputs.

Chapter 2

SENSITIVITY ANALYSIS

2.1 Sensitivity Analysis of Gassmann's Fluid Substitution Equations

ABSTRACT

In this chapter we quantify the sensitivity of velocity predictions made using Gass-mann's fluid-substitution equations to uncertainties in the input rock and fluid properties. We define a sensitivity factor, E_i, as the ratio of the fractional error in the predicted V_P to the fractional error in each input parameter. Fluid-substitution predictions of V_P are most sensitive to the original V_P, with E_i between 1 and 5. The sensitivity of the predicted V_P to the original V_S, porosity, and mineral bulk modulus are much lower, with E_i between 0.1 and 0.5. The sensitivity of the predicted V_P to the bulk modulus and density of water and oil is also low, with E_i between 0.1 and 0.5. The sensitivity to the bulk modulus and density of gas is extremely low, with E_i always below 10^{-3}. However, since the properties of gas are very highly sensitive to changes in pressure and temperature, the uncertainties in these values can be very large.

INTRODUCTION

Gassmann's (1951) equations of fluid substitution are frequently used to predict velocities of rocks saturated with different pore fluids. Given the V_P (compressional wave velocity), V_S (shear wave velocity), and ρ (density) of a dry rock (or a rock saturated with one fluid), these equations predict the V_P and V_S of the saturated rock (or the rock saturated with a new fluid). The Gassmann velocity prediction also requires a few other inputs: the mineral bulk modulus (K_0), the porosity (ϕ), the fluid bulk moduli (K_{fl}) and fluid densities (ρ_{fl}).

More often than not, at least some of the Gassmann inputs are uncertain, owing to measurement errors, unavailability of data, and natural lithologic variation. In this chapter, the question we address is: How sensitive are predictions using Gassmann's equations to uncertainties in the required rock and fluid properties?

We quantify the sensitivity of Gassmann's fluid-substitution equations to uncertainties

in all the required inputs, using an analytical approach. We present the results for all sandstones, by including all combinations of ϕ and V_P falling between the Hashin-Shtrikman bounds (Hashin and Shtrikman, 1963). We also present results for different fluids: water, oil and gas. Finally, we address velocity prediction in partially saturated rocks, where there are uncertainties in the fluid saturations.

We carry the sensitivity analysis a step further in Chapter 2.3, where we apply Monte-Carlo techniques to quantify the uncertainty in the AVO response of rocks as a result of fluid substitution (refer to table 2.8 and Figures 2.26 and 2.28 in Chapter 2.3).

THEORY AND APPROACH

Given the bulk modulus (K) and shear modulus (μ) of a rock saturated with one fluid (fl_1), the low frequency Gassmann (1951) theory predicts the bulk modulus and shear modulus of a rock saturated with a different fluid (fl_2), through the following equations:

$$\frac{K_2}{K_2 - K_0} - \frac{K_{fl_2}}{\phi(K_{fl_2} - K_0)} = \frac{K_1}{K_1 - K_0} - \frac{K_{fl_1}}{\phi(K_{fl_1} - K_0)} \tag{2.1}$$

$$\mu_2 = \mu_1 \tag{2.2}$$

The subscript 0 refers to the mineral, 1 refers to the properties of the rock saturated with the original fluid (fl_1), and 2 refers to the properties of the rock saturated with the new fluid (fl_2). The bulk density change is given by:

$$\rho_2 - \rho_1 = \phi(\rho_{fl_2} - \rho_{fl_1}) \tag{2.3}$$

We then can calculate the V_P and V_S of the rock saturated with the new fluid using the equations:

$$V_P = \sqrt{\frac{K + \frac{4}{3}\mu}{\rho}} \tag{2.4}$$

$$V_S = \sqrt{\frac{\mu}{\rho}} \tag{2.5}$$

The system of equations (2.1) through (2.5) form the fluid substitution recipe that is commonly used in predicting the change in V_P and V_S of rocks due to a change in the pore fluid. We can write the fluid substitution recipe as a function of nine inputs as follows:

$$V_{P_2} = f_G(V_{P_1}, V_{S_1}, \rho_1, K_0, \phi, K_{fl_1}, \rho_{fl_1}, K_{fl_2}, \rho_{fl_2}) \tag{2.6}$$

$$V_{P_2} = f_G(p_i)_{i=1:9} \tag{2.7}$$

We computed the partial derivatives of the predicted velocity (V_{P_2}) with respect to each of the nine inputs. The error in the predicted velocity $(\delta_i V_{P_2})$ due to an error in any one input (p_i) is approximated by the partial derivative of V_{P_2} with respect to that input multiplied by the input error (δp_i).

$$\delta_i V_{P_2} = \frac{\partial V_{P_2}}{\partial p_i} \delta p_i \tag{2.8}$$

The total error in V_{P_2} is the sum of all the partial derivatives, weighted by the error in the corresponding input:

$$\delta V_{P_2} = \sum_{i=1}^{9} \delta_i V_{P_2} = \sum_{i=1}^{9} \frac{\partial V_{P_2}}{\partial p_i} \delta p_i \tag{2.9}$$

We calculated the partial derivatives for each of the nine input parameters, as shown in Equation (2.8), for all physically realizable combinations of V_P and ϕ, i.e., those combinations that fall within the Hashin-Strikman bounds (1963). We estimated the corresponding V_S using Han's $V_P - V_S$ relations (Han, 1986) shown:

$$V_S = 0.7936 V_P - 0.7868 \tag{2.10}$$

where the units of V_P and V_S are km/s. We then computed the error multiplier E_i for each input, as follows:

$$\frac{\delta V_{P_2}}{V_{P_2}} = \frac{\partial V_{P_2}}{\partial p_i} \frac{p_i}{V_{P_2}} \frac{\delta p_i}{p_i} = E_i \frac{\delta p_i}{p_i} \tag{2.11}$$

The E_i is the ratio of output fractional (or percent) error to the input fractional (or percent) error. We can compute the fractional error in the predicted velocity, by multiplication of the fractional error in the input with the corresponding E_i.

We also computed the differential error, which is defined as the error in the predicted *fractional change* in V_P. The error in the fractional change in V_P due to uncertainties in the inputs of the fluid substitution recipe is

$$\delta\left[\frac{V_{P_2}-V_{P_1}}{V_{P_1}}\right]=\delta\left[\frac{V_{P_2}}{V_{P_1}}-1\right]=\sum_i\frac{\partial}{\partial p_i}\left(\frac{f_G}{V_{P_1}}\right)\Delta p_i \tag{2.12}$$

For each individual term within the summation, we can write:

$$\begin{aligned}\frac{\partial}{\partial p_i}\left(\frac{f_G}{V_{P_1}}\right)\Delta p_i &= \frac{V_{P_1}\frac{\partial f_G}{\partial p_i}-f_G\frac{\partial V_{P_1}}{\partial p_i}}{V_{P_1}^2}\Delta p_i \\ &= \left(\frac{1}{V_{P_1}}E_i\frac{V_{P_2}}{p_i}-\frac{V_{P_2}}{V_{P_1}^2}\delta_{1i}\right)\Delta p_i \\ &= (E_i-\delta_{1i})\frac{V_{P_2}}{V_{P_1}}\frac{\Delta p_i}{p_i}\end{aligned} \tag{2.13}$$

where δ_{ij} is the Kronecker delta function. The differential error multiplier (D_i) can thus be defined in terms of the error multiplier (E_i) as

$$D_i=(E_i-\delta_{1i})\frac{V_{P_2}}{V_{P_1}} \tag{2.14}$$

We computed the values of D_i for all physically possible combinations of V_P and porosity, and for four different fluid changes. Given an uncertainty of x in any input parameter, the corresponding uncertainty in the predicted fractional change V_P is given by $D_i x$.

Finally, we looked at partially saturated rocks where there are uncertainties in fluid saturations. The effective fluid model (Domenico, 1976) suggests that the mixture of gas-oil-water phases in the rock can be replaced by an average fluid whose bulk modulus is computed using the Reuss average (Reuss, 1929), and the density is a simple volumetric average.

$$\frac{1}{K_{fl}}=\sum_i\frac{S_i}{K_{fl_i}} \tag{2.15}$$

$$\rho_{fl}=\sum_i S_i\rho_{fl_i} \tag{2.16}$$

We used the effective fluid model coupled with Gassmann's equations to compute uncertainties due to fluid substitution in partially saturated rocks.

WATER, OIL, AND GAS

We quantify the sensitivity of the Gassmann recipe for the following fluid substitutions: (a) water saturated to oil saturated, (b) oil saturated to water saturated, (c) water saturated to gas saturated, and (d) gas saturated to water saturated rocks. The mineral and fluid properties used are shown in Table 2.1.

Table 2.1: Mineral and Fluid Properties.

Mineral/Fluid	Bulk Modulus (GPa)	Density (kg/m^3)
Quartz	36.6	2650
Water	2.25	1000
Oil	1.00	800
Gas	10^{-4}	1

Water to Oil

Figure 2.1 shows the original water-saturated rock velocity (V_{P_1}), the predicted oil-saturated velocity (V_{P_2}), the predicted change in V_P due to fluid substitution ($\Delta V_P = V_{P_2} - V_{P_1}$), and the percent change in V_P due to fluid substitution ($\Delta V_P / V_{P_1}$). The solid black lines are the Hashin-Shtrikman upper and lower bounds for water-saturated sandstones. The critical porosity line (Nur et al., 1995) is shown by the dashed white line. Most sandstone velocity values typically lie between the Hashin-Shtrikman lower bound and the critical porosity line. Figure 2.1 shows that the soft rocks, which lie near the Hashin-Shtrikman lower bound, are more sensitive to a fluid change, while the stiffer rocks are less sensitive to a fluid change.

Figure 2.2 shows the E_i values for water to oil fluid substitution plotted versus porosity (x-axis) and water-saturated rock V_P (y-axis) for all nine input parameters. Each figure is

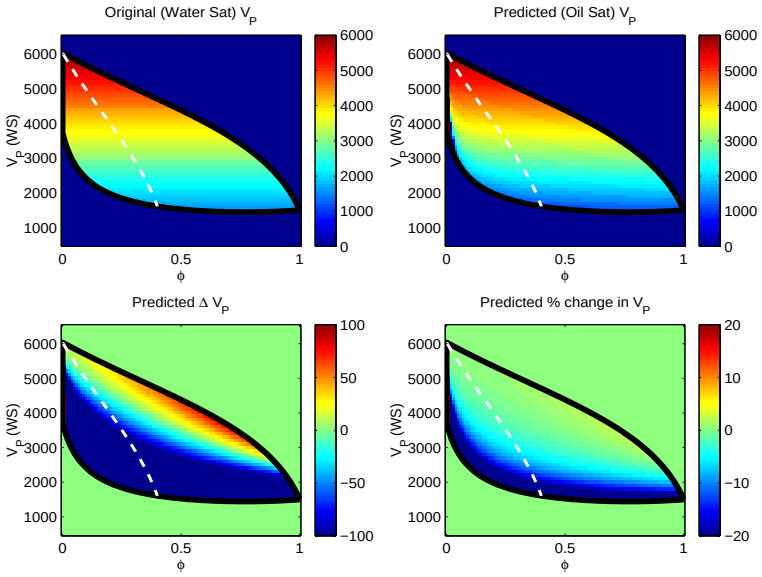

Figure 2.1: Water to oil: The quantities of interest are plotted in color as a function of porosity (x-axis) and reference water saturated V_P (y-axis). The black lines are the Hashin-Shtrikman upper and lower bounds. The dashed white line is the critical porosity line. Top left: Original rock velocity of water-saturated rock (V_{P_1}), Top right: Gassmann predicted velocity of oil-saturated rock (V_{P_2}), Bottom left: Predicted change in rock velocity ($\Delta V_P = V_{P_2} - V_{P_1}$), Bottom right: Predicted percent change in Rock velocity ($\Delta V_P / V_{P_1}$).

labeled with the relevant input parameter. The top left figure shows the E_i values for an uncertainty in the value of V_{P_1}, the velocity of the original (water-saturated) rock. This figure shows that the fractional error in the predicted V_{P_2} could be double the fractional error in V_{P_1} for soft rocks ($E_i = 2$). For stiffer rocks, the fractional error in the predicted V_{P_2} is roughly equal to the fractional error in the original V_{P_1} ($E_i = 1$). It is therefore very important to have accurate measurements of the original V_{P_1}.

The sensitivity (E_i) to the other inputs is much lower. A fractional error of 0.01 in any of the other 8 inputs would cause a fractional error of 0.001-0.002 in the predicted V_{P_2}. Notice that the color scale for the E_i values is 0-2 for V_{P_1} and 0-0.2 for all the other 8 inputs. The sensitivity to V_{S_1}, ρ_1, ϕ, and K_{fl} is larger in soft rocks ($E_i >= 0.1$) than in stiff rocks ($E_i < 0.1$). The sensitivity to K_0 is very low ($0 < E_i < 0.1$), except for some very soft sandstones lying close to the Hashin-Shtrikman lower bound ($0.1 <= E_i <= 0.2$). The sensitivity to the fluid densities is very low ($E_i < 0.1$) everywhere between the critical

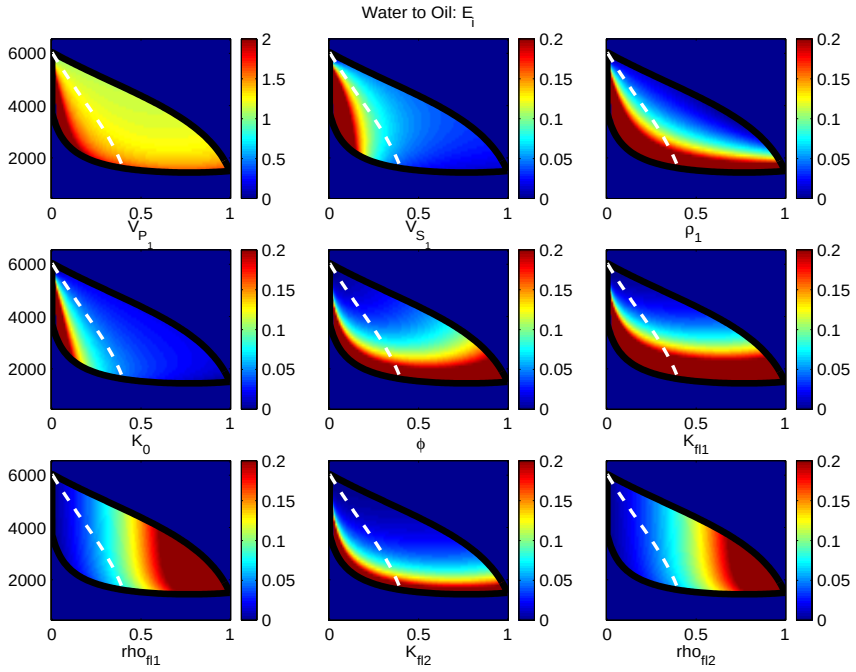

Figure 2.2: Water to oil: E_i values plotted as color scale values (refer Equation 2.11) versus porosity (x-axis) and water-saturated velocity (y-axis) for all nine input parameters. Each figure is labeled with the input parameter that is uncertain.

porosity line and the Hashin-Shtrikman lower bound.

Figure 2.3 shows the value of $\delta V_{P_2}/\Delta V_{P_2}$ for an error of 0.01 in each of the inputs. This quantity becomes very large in the places where the predicted change in V_P is zero or small. Therefore, this is not a very useful estimate of the error and we do not use this quantity in the next few examples.

Figure 2.4 shows the value of $\frac{\partial V_{P_2}}{\partial p_i} p_i$. Multiplying the plotted value with the fractional error in the input parameter would yield δV_{P_2}, which is the error in the output (V_{P_2}) in m/s. We do not plot this quantity in the other examples to avoid redundancy, since Figure 2.1 and Figure 2.2 already contain information about the value of $E_i V_{P_2}$.

Figure 2.5 shows the Differential Error Multiplier (D_i) for the nine input parameters of the fluid substitution recipe, where the original fluid is water, and the new fluid is oil. In the top left diagram, we see that for very soft rocks lying nearly on the lower Hashin-Shrikman bound, the value of D_i is approximately 1. This means that, if the uncertainty

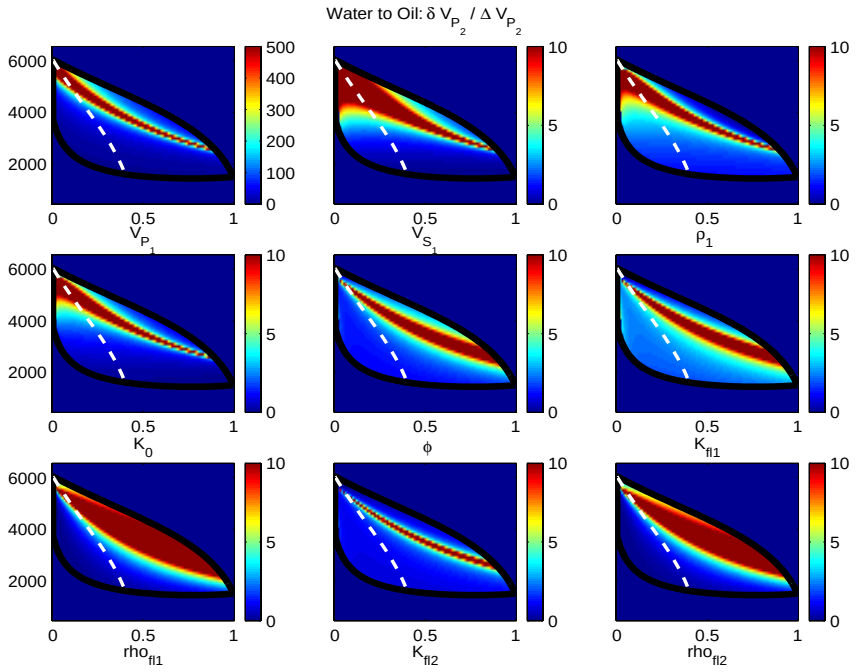

Figure 2.3: Water to oil: $E_i \Delta V_{P_2}$ (see Equation 2.11) plotted versus porosity (x-axis) and water-saturated V_P (y-axis) for all nine input parameters. In each figure, the labels indicate the uncertain parameters.

in the original V_P is 5 %, then the uncertainty in the predicted fractional change could be 5 %. Therefore, if the Gassmann-predicted change is 15 %, (as shown in Figure 2.1) the observed velocity change could be anywhere between 10 and 20 %, due to the uncertainty in V_P. From the other diagrams in Figure 2.5, we observe that the D_i values are typically higher for soft rocks, demonstrating that soft rocks are more sensitive to uncertainties in inputs. For most of the input parameters, the D_i magnitude lies between 0 an 0.5. The sensitivity to fluid density appears to be extremely low (below 0.1) for all rocks between the lower Hashin-Shtrikman bound and the critical porosity line.

Oil to Water

We repeated the procedure, but this time we predicted water-saturated velocities from an originally oil-saturated rock. Figure 2.6 shows the original velocities of the oil-saturated

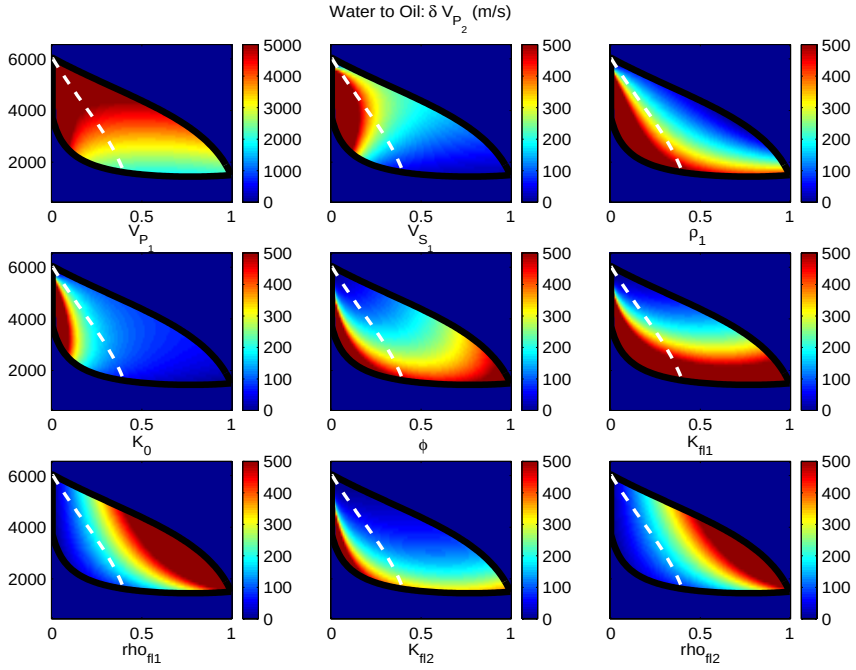

Figure 2.4: Water to oil: $E_i V_{P_2}$ plotted as a function of porosity (x-axis) and water-saturated V_P (y-axis) for all nine input paramters. The label of each subplot indicates the uncertain parameter.

rocks (V_{P_1}), the predicted water-saturated velocities (V_{P_2}), the predicted change in velocities (ΔV_P), and the predicted percent changes in velocities. As in the water to oil fluid substitution case, the soft rocks are more sensitive to the fluid change than the stiffer rocks.

Figure 2.7 shows the sensitivity of the oil to water fluid substitution. The results of the oil to water prediction are very similar to the water to oil prediction. The sensitivity to V_{P_1} uncertainties is very large ($1 <= E_i <= 2$). The sensitivity to uncertainties in all other inputs is much smaller ($0 <= E_i <= 0.2$). The soft rocks again show a greater sensitivity to errors in inputs than stiff rocks.

The D_i values for oil to water fluid substitution are similar to the water to oil case, except, of course, in this case, we generally observe velocity drops as opposed to velocity increases. Figure 2.8 shows that the D_i for the V_P lies between 0.5 and 1, while the D_i for the input V_S, rock density, porosity, mineral modulus and fluid moduli are below 0.5. The D_i for the fluid densities are less than 0.1.

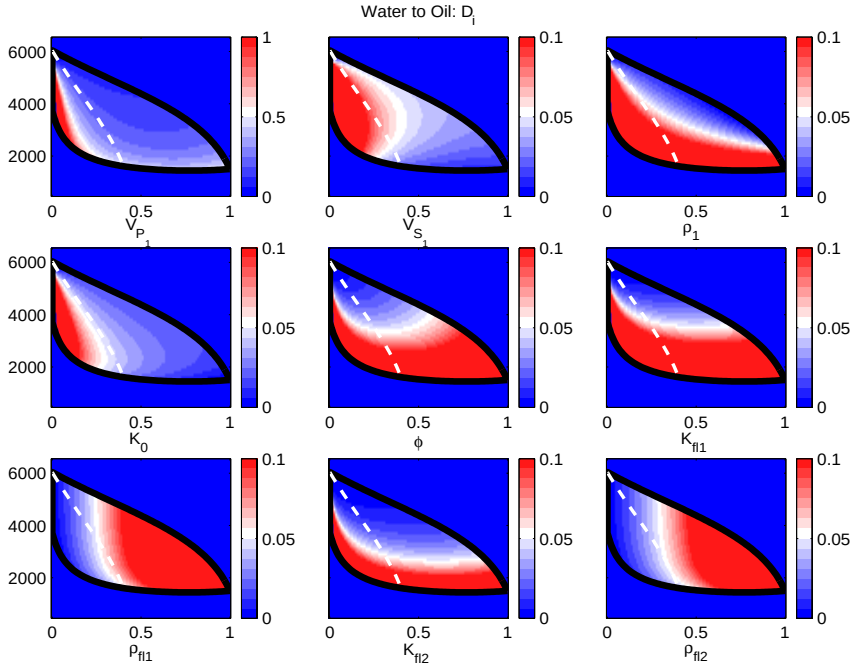

Figure 2.5: Water to Oil: D_i for all sandstones within the Hashin-Shtrikman bounds, shown as color scale values as a function of porosity and water-saturated P-wave velocity. The uncertain input parameter is labeled below the corresponding figure.

Water to Gas

In this example, the original fluid was water, and the new fluid substituted into the rocks was gas. Figure 2.9 shows the original and new velocities, and the absolute and percent changes in velocities. Figure 2.10 shows the E_i values. The predicted V_{P_2} is very sensitive to errors in the original V_{P_1}. The sensitivity to V_{P_1} is larger than in the water to oil and oil to water fluid substitution cases ($1 < E_i < 5$), especially when the rocks are soft. The sensitivity to V_{S_1}, ρ_1, ϕ, and K_{water} is much smaller ($0 < E_i < 0.5$). The sensitivity to K_0 is still smaller: E_i ranges from 0.1-0.2. The sensitivity of the fluid substitution to the bulk modulus of gas and density of the gas is negligibly small. The E_i for an error in K_{gas} is less than 10^{-5}, while the E_i for an error in ρ_{gas} is less than 10^{-3}.

Figure 2.11 shows that the fractional change in velocity is very sensitive to uncertainties in the input V_P. For many of the softer rocks, the D_i is very high, generally between 1 and

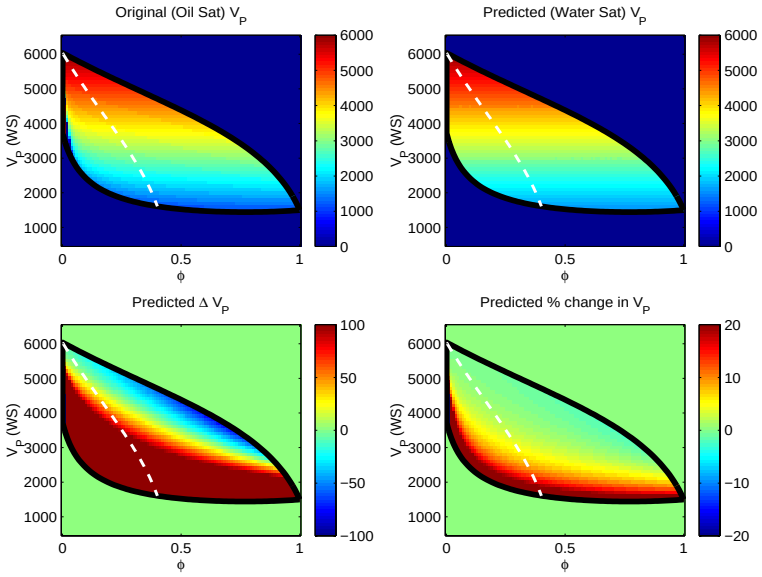

Figure 2.6: Oil to water: Top left: Original rock velocity of oil-saturated rock (V_{P_1}), Top right: Gassmann predicted velocity of water-saturated rock (V_{P_2}), Bottom left: Predicted change in rock velocity ($\Delta V_P = V_{P_2} - V_{P_1}$), Bottom right: Predicted percent change in Rock velocity ($\Delta V_P / V_{P_1}$).

4. The other input parameters (V_S, ρ, ϕ, K_0, K_{water} and ρ_{water}) show a much lower D_i between 0 and 0.5. The gas bulk modulus and density show an extremely low D_i of less than 10^{-3}. This result is consistent with the E_i results.

Gas to Water

In this section, we compute the sensitivity of fluid substitution when the original fluid is gas, and the new fluid is water. Figure 2.12 shows the original and predicted velocities, and the predicted change in the velocities. The change is again larger in the soft rocks than in the stiff rocks. Figure 2.13 shows the E_i values. The results are very similar to the prediction of gas-saturated velocities from water-saturated velocities. The predicted V_{P_2} has the highest sensitivity to V_{P_1} ($1 < E_i < 5$). V_{P_2} has a much lower sensitivity to the V_S, ρ, ϕ, K_0, K_{water} and ρ_{water} ($0.1 < E_i < 0.5$) . The sensitivity to the gas bulk modulus and density is almost negligible ($E_i < 10^{-3}$). The D_i values are similar to the water to gas

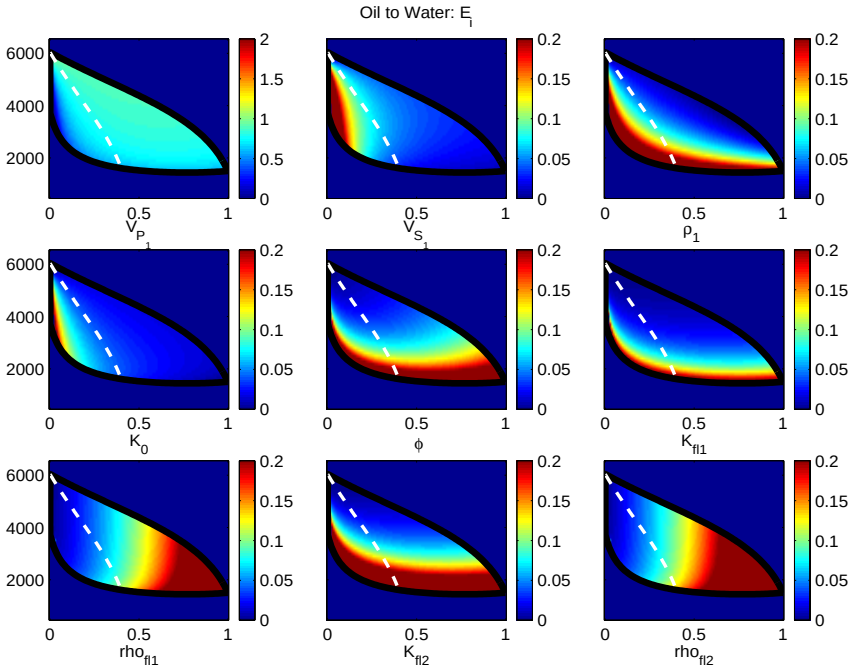

Figure 2.7: Oil to water: E_i values (refer Equation 2.11) plotted in color versus porosity (x-axis) and water-saturated velocity (y-axis) for all nine input parameters.

case. Softer rocks have a higher D_i than stiff rocks, original V_P has the highest D_i, and the gas bulk modulus and the density have an almost negligible D_i.

SATURATION UNCERTAINTIES

In the case of partially saturated rocks, where fluid phases are mixed together in the pore spaces, the effective fluid bulk modulus can be estimated by the Reuss average (Reuss, 1929), shown in Equation 2.15. Uncertainties in the fluid saturations can lead to uncertainties in the effective fluid properties (bulk modulus and density), which are then used in Gassmann's equations to predict the partially saturated rock velocities. In this section we quantify the uncertainty in the effective fluid properties caused by uncertainties in the saturations.

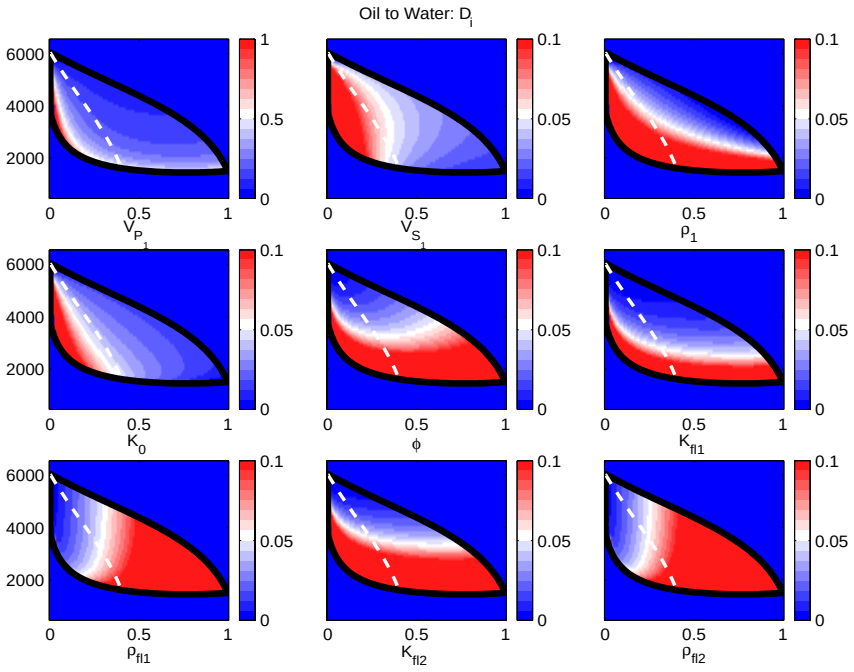

Figure 2.8: Oil to Water: D_i for all sanstones within the Hashin-Shtrikman bounds, shown as color scale values as a function of porosity and water-saturated P-wave velocity. The uncertain input parameter is labeled below the corresponding figure.

Two Fluids

When there are only two fluids (eg. water and oil, no gas), we must consider the uncertainty in the saturation of only one of the fluids, because the saturations are constrained by the equation:

$$\sum_i S_i = 1 \tag{2.17}$$

Differentiating Equation 2.15 with respect to S_1, we obtain,

$$\frac{\partial K_{fl}}{\partial S_1} = K_{fl}^2 \left(\frac{1}{K_{fl_2}} - \frac{1}{K_{fl_1}} \right) \tag{2.18}$$

$$\frac{\delta K_{fl}}{K_{fl}} = \frac{\partial K_{fl}}{\partial S_1} \frac{\delta S_1}{K_{fl}} = \left[K_{fl} \left(\frac{1}{K_{fl_2}} - \frac{1}{K_{fl_1}} \right) S_1 \right] \frac{\delta S_1}{S_1} = F_K \frac{\delta S_1}{S_1} \tag{2.19}$$

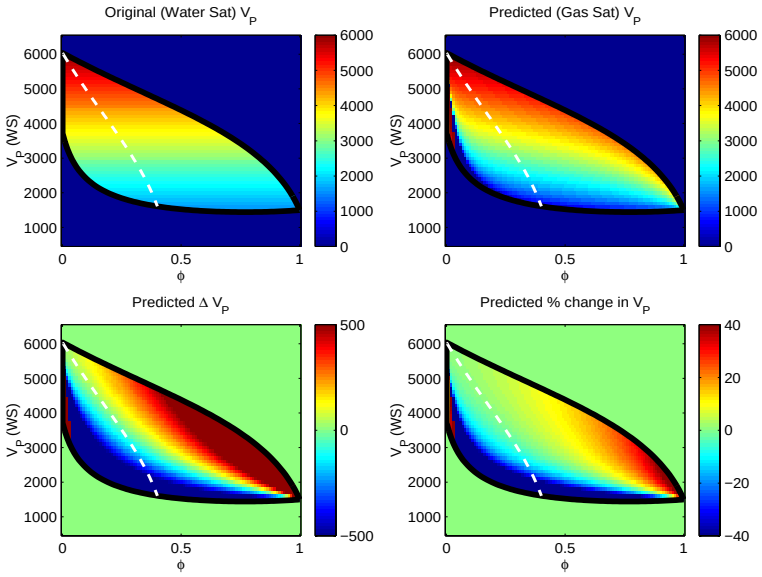

Figure 2.9: Water to Gas: Top left: Original rock velocity of water-saturated rock (V_{P_1}), Top right: Gassmann predicted velocity of gas-saturated rock (V_{P_2}), Bottom left: Predicted change in rock velocity ($\Delta V_P = V_{P_2} - V_{P_1}$), Bottom right: Predicted percent change in Rock velocity ($\Delta V_P / V_{P_1}$).

Equation 2.19 defines the factor F_K, which is the sensitivity of the effective fluid bulk modulus to the saturation. Figure 2.15 shows a plot of the quantity F_K versus S_w for oil-water and gas-water mixes. From Figure 2.15(c), we observe that, for oil-water mixes, with an uncertainty of 0.1 in $\frac{\delta S_W}{S_W}$, the uncertainty in the effective fluid bulk modulus is between 0 (at $S_W = 0$) and 1 (at $S_W = 1$). Figure 2.15(c) shows that, for gas-water systems, the uncertainty is small when $0 \leq S_W \leq 0.9$, but grows very large (on the order of 10^4) near $S_W = 1$. The reason for this drastic change in uncertainty can be seen in Figure 2.15(a), where there is a large jump in $K_{eff-fluid}$ at $S_W = 1$ of 2.5x10^9. The corresponding derivative is therefore large.

Differentiating Equation 2.16, we obtain,

$$\frac{\partial \rho_{fl}}{\partial S_1} = \rho_{fl_1} - \rho_{fl_2} \tag{2.20}$$

$$\frac{\delta \rho_{fl}}{\rho_{fl}} = \left[\frac{S_1}{\rho_{fl}} (\rho_{fl_1} - \rho_{fl_2}) \right] \frac{\delta S_1}{S_1} = F_\rho \frac{\delta S_1}{S_1} \tag{2.21}$$

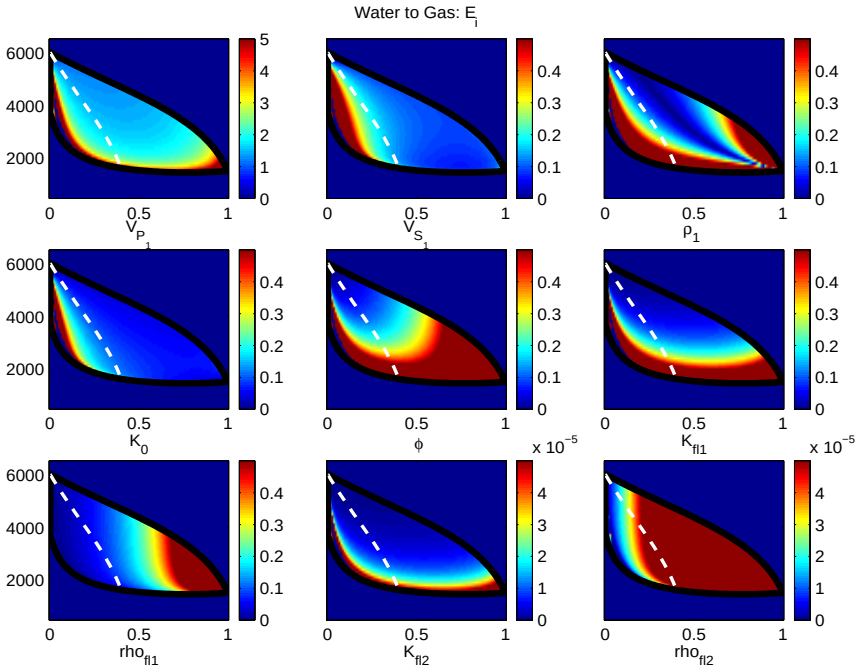

Figure 2.10: Water to Gas: E_i values plotted (refer Equation 2.11) in color versus porosity (x-axis) and water-saturated velocity (y-axis) for all nine input parameters.

Equation 2.21 defines the factor F_ρ, which is the sensitivity of the effective fluid bulk modulus to the saturation. Figure 2.15(d) shows that, for oil-water mixes, F_ρ lies between 0 and 0.1. For gas-water mixes, F_ρ is about 1.

Three Fluids

When the rock is saturated with more than two fluids, we can write the following equations by differentiating Equation 2.15.

$$\delta K_{fl} = \sum_{i=1}^{n} \frac{\partial K_{fl}}{\partial S_i} \delta S_i \tag{2.22}$$

$$\frac{\partial K_{fl}}{\partial S_i} = K_{fl}^2 \left(\frac{1}{K_{fl_n}} - \frac{1}{K_{fl_i}} \right) \tag{2.23}$$

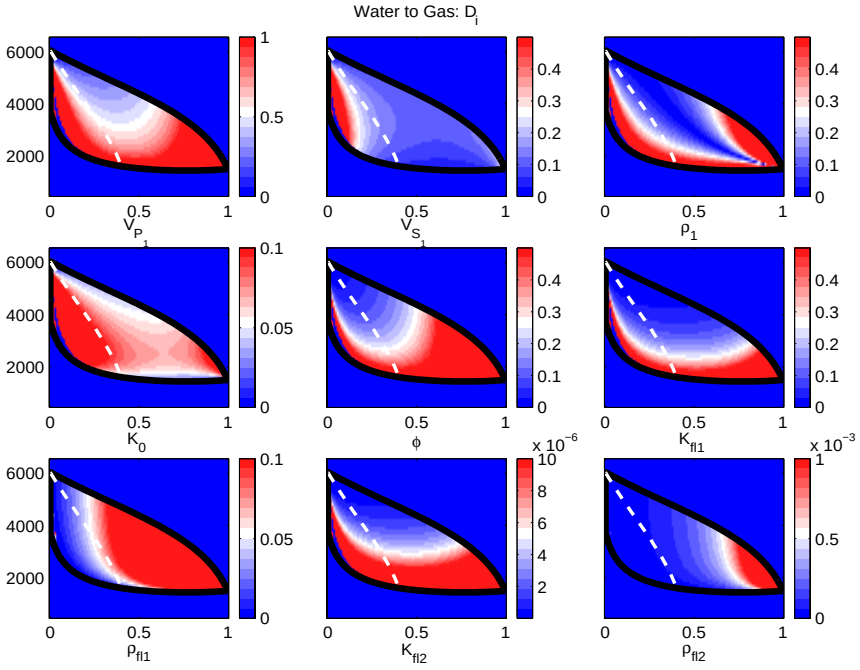

Figure 2.11: Water to gas: D_i for all sanstones within the Hashin-Shtrikman bounds, shown as color scale values as a function of porosity and water-saturated P-wave velocity. The uncertain input parameter is labeled below the corresponding figure.

$$\frac{\delta K_{fl}}{K_{fl}} = \sum_{i=1}^{n} \left[K_{fl} \left(\frac{1}{K_{fl_n}} - \frac{1}{K_{fl_i}} \right) S_i \right] \frac{\delta S_i}{S_i} \tag{2.24}$$

Differentiating Equation 2.16 we can write

$$\frac{\partial \rho_{fl}}{\partial S_i} = \rho_{fl_i} - \rho_{fl_n} \tag{2.25}$$

$$\frac{\delta \rho_{fl}}{\rho_{fl}} = \sum_{i=1}^{n} \left[\left(\rho_{fl_i} - \rho_{fl_n} \right) S_i \right] \frac{\delta S_i}{S_i} \tag{2.26}$$

The sensitivity of the effective fluid properties to uncertainties in saturations can be computed from the above equations.

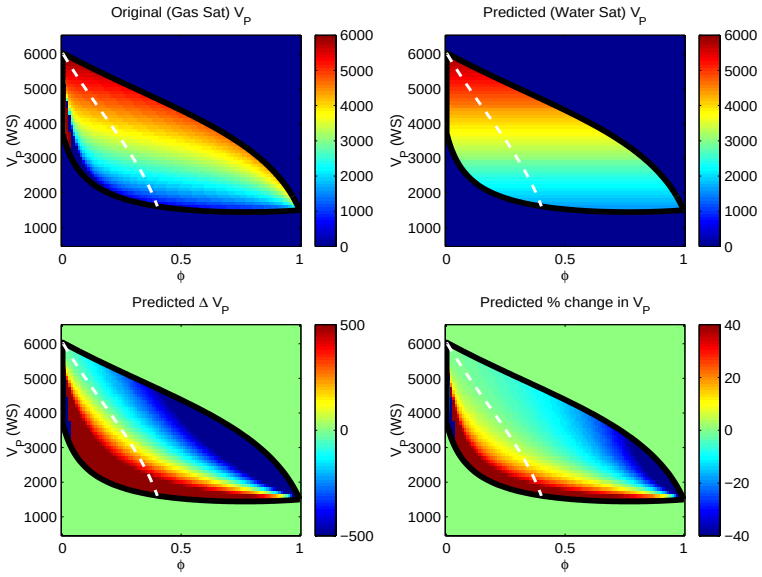

Figure 2.12: Gas to water: Top left: Original rock velocity of gas-saturated rock (V_{P_1}), Top right: Gassmann predicted velocity of water-saturated rock (V_{P_2}), Bottom left: Predicted change in rock velocity ($\Delta V_P = V_{P_2} - V_{P_1}$), Bottom right: Predicted percent change in rock velocity ($\Delta V_P / V_{P_1}$).

CONCLUSIONS

We defined a sensitivity factor, E_i, as the ratio of the fractional error in the predicted V_P to the fractional error in each input parameter (summarized in Table 2.2). The fluid-substitution predictions of V_P are the most sensitive to the original V_P, with E_i between 1 and 5. This indicates that an uncertainty of 1% in the original V_P would result in an uncertainty of 1 to 5% in the predicted V_P. The sensitivity to the original V_S, ϕ, and K_0 are much lower, with E_i between 0.1 and 0.5. This means that an error of 10% in the mineral bulk modulus, for example, would lead to an error of only 1% in the predicted P-wave velocity. The sensitivity to the bulk modulus and density of water and oil is also low, with E_i between 0.1 and 0.5. The sensitivity to the bulk modulus and density of gas is extremely low, with the E_i corresponding to these two inputs is always below 10^{-3}. However, the fluid densities and bulk moduli are the parameters that can potentially be the most uncertain, since their values change a lot with pressure, temperature, and partial saturation.

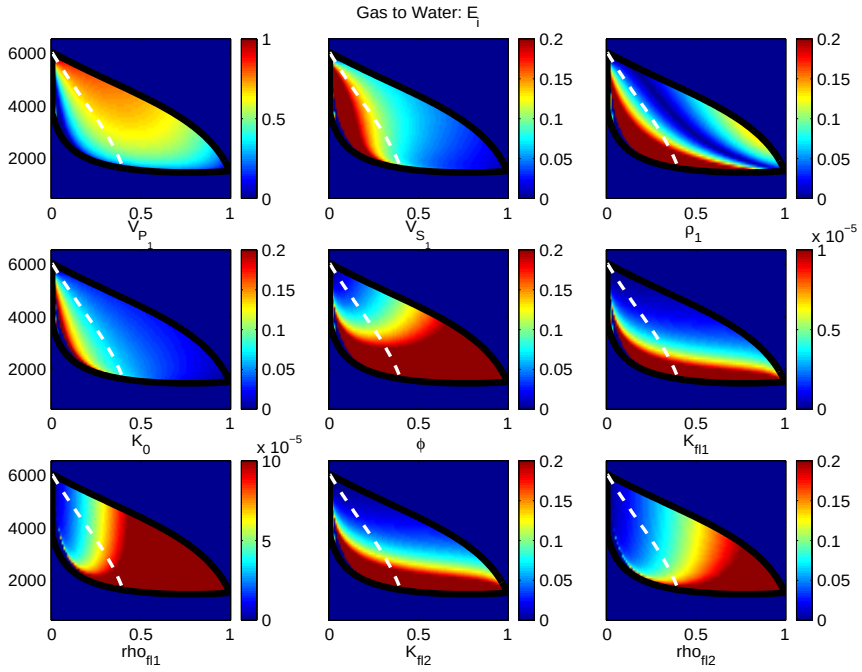

Figure 2.13: Gas to water: E_i values (refer Equation 2.11) versus porosity (x-axis) and water-saturated velocity (y-axis) for all nine input parameters.

Table 2.2: Sensitivity of Fluid-Substitution Recipe, where x is the fractional error in each input.

Fluid substitution Sensitivity Summary	
Input Parameter	Fractional Error in predicted V_P
V_{P_1}	$(1.0 - 5.0)x$
V_{S_1}	$(0.1 - 0.5)x$
ρ_1	$(0.1 - 0.3)x$
K_0	$(0.1 - 0.4)x$
ϕ	$(0.1 - 0.5)x$
K_{water}	$(0.1 - 0.5)x$
ρ_{water}	$(0.0 - 0.4)x$
K_{oil}	$(0.1 - 0.5)x$
ρ_{oil}	$(0.0 - 0.4)x$
K_{gas}	$(0.0 - 10^{-5})x$
ρ_{gas}	$(0.0 - 10^{-3})x$

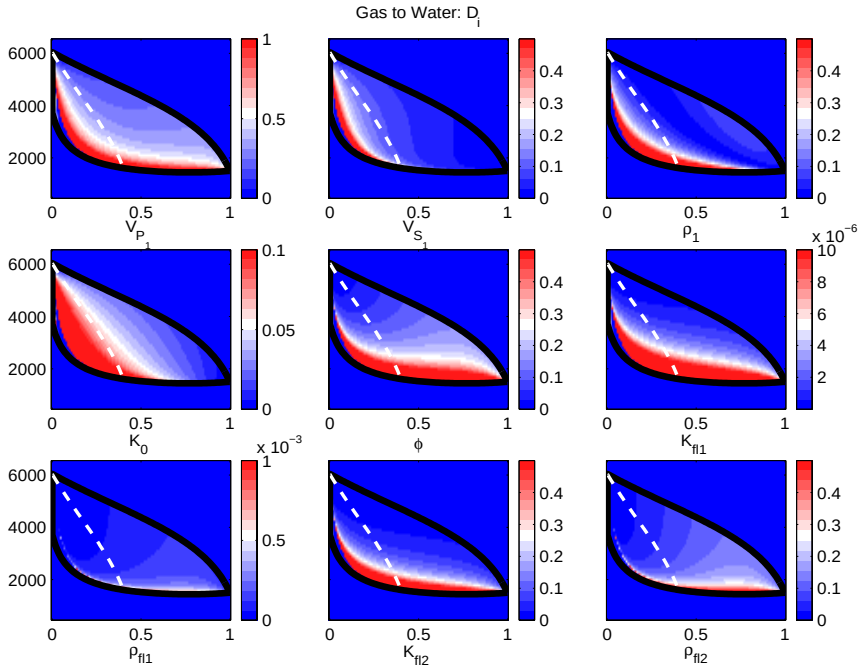

Figure 2.14: Gas to Water: D_i for all sanstones within the Hashin-Shtrikman bounds, shown as color scale values as a function of porosity and water-saturated V_P. The uncertain input parameter is labeled below the corresponding figure.

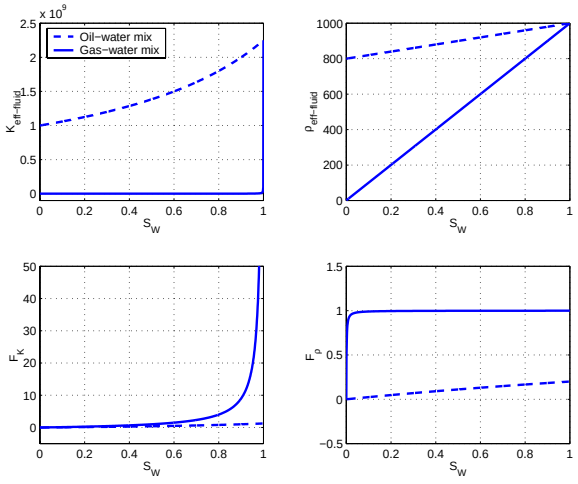

Figure 2.15: Uncertainties in effective fluid properties due to uncertainties in fluid saturations. Top left: Effective fluid bulk modulus versus S_w. Top right: Effective fluid density versus S_w. Bottom left: F_K (Equation 2.19) vs S_w. Bottom right: F_ρ (Equation 2.21) vs S_w.

2.2 Seismic Detectability of Free Gas versus Dissolved Gas

ABSTRACT

We quantify the seismic velocities of rock saturated with free and dissolved gas, using Batzle-Wang's equations coupled with fluid substitution recipes. We conclude that, given the same mass of gas, the rock containing free gas always has a lower velocity than the rock containing only dissolved gas if the oil and gas are mixed at a very fine scale. For a fine-scale mix of oil and gas, the seismic velocity is dominated by the free gas saturation, and the oil gravity and GOR have a negligible effect on the velocity. However, in the case of a coarse-scale or patchy mix of oil and gas, the rock containing free gas may have slightly higher or lower seismic velocities than the rock containing dissolved gas, depending on the dry rock stiffness, the porosity, and the oil gravity.

INTRODUCTION

Batzle (1995) pointed out that direct hydrocarbon indicators such as bright spots and AVO anomalies can be modified substantially by natural variations in hydrocarbon properties and changes in these properties brought on by production. A simple "gas" model is often inadequate since live oils can give a similar response. Reservoir properties may change substantially due to production because of changes in Pressure, temperature, dissolution of gas etc.

Presence of gas in the subsurface can lead to striking effects in the seismic response, such as large amplitude anomalies and increased traveltimes. Oil production often leads to a pressure drop in the reservoir. If the oil contains dissolved gas, the production related pressure drop can cause the dissolved gas to come out of solution, greatly increasing seismic amplitudes and traveltimes. In this chapter we quantify the seismic detectability of free gas versus dissolved gas.

The problem of free gas versus dissolved gas can also be an issue in interpreting saturations from flow simulation outputs. For example, flow simulators can be made to run faster by forcing them to assume either that the gas-oil-ratio (GOR) is zero or that the GOR does not change during the run. However, this assumption may not be true in the actual reservoir.

Flow simulators may predict the correct *mass* of gas in a simulator cell, which the reservoir engineer cares about, but it may not correctly predict whether the gas is free or dissolved, which is critical for seismic analysis. The questions that arise are: How accurately must we know the free gas saturations to model a reasonably correct value of the seismic velocity? How accurately can we interpret seismic velocities in terms of saturation if the GOR is uncertain?

In this study, we used the results from Batzle and Wang (1992) to calculate the acoustic velocities of gas, oil, and oil containing dissolved gas. We then used Gassmann's (1951) fluid substitution equations to predict the corresponding velocities of oil-saturated and gas-saturated rocks. We performed the study on different rock types, for various oil properties, and for different scenarios such as gas injection and gas coming out of solution.

Increasing the GOR reduces the bulk modulus and density of oil. Heavy oils can dissolve only small amounts of gas. We therefore find that the properties of dead oil (oil with no dissolved gas) are quite similar to the properties of saturated oil (oil containing the maximum allowable amount of dissolved gas) if the oil is heavy. And because a heavy oil is always much less compressible than the gas that dissolves in it, rocks saturated with heavy oils show a large velocity difference between free gas (gas-oil mix) and dissolved gas (gas-oil solution).

In contrast, light oils can dissolve large amounts of gas. In this case, live oil properties can therefore be quite different than dead oil properties. Light oils containing large amounts of dissolved gas are very compressible. Therefore, less seismic difference exists between free gas and dissolved gas for rocks saturated with light oils.

FLUID PROPERTIES

A widely used classification of crude oil is the American Petroleum Institute oil gravity (API gravity):

$$API = \frac{141.5}{\rho_0} - 131.5 \tag{2.27}$$

where ρ_0 is the density of oil in g/cm^3 at 15.6^{o}C and atmospheric pressure.

The Batzle-Wang (1992) equations (Equations (2.28) - (2.32)) give empirical relations for seismic velocities of oil and gas, in terms of temperature, pressure, and compaction. The acoustic velocity (in m/s) of dead oil depends on pressure P (in MPa) and temperature T (in degrees Celsius) as

$$V_p = 2096\left(\frac{\rho_0}{2.6-\rho_0}\right)^{\frac{1}{2}} - 3.7T + 4.64P + 0.0115\left[4.12\left(1.08\rho_0^{-1}\right)^{\frac{1}{2}} - 1\right]TP \tag{2.28}$$

A live oil in situ is usually characterized by the gas-oil-ratio (GOR or R_G). GOR is defined as the volume ratio of liberated gas to remaining oil at atmospheric pressure and 15.6^{o}C. The maximum amount of gas that can be dissolved in oil is a function of pressure, temperature, and the composition of both the gas and the oil.

$$R_G^{max} = 0.02123G\left[Pexp\left(\frac{4.072}{\rho_0} - 0.00377T\right)\right]^{1.205} \tag{2.29}$$

where R_G is in liters/liter (1 L/L = 5.615 ft^3/bbl) and G is the gas gravity. From Equation (2.29) we see that increasing P, decreasing T, and decreasing ρ_0 all tend to increase the amount of gas that can be dissolved. Similarly, decreasing P or increasing T can cause gas to come out of solution.

P-wave velocities in oils with dissolved gas can be calculated versus pressure and temperature by Equation (2.28), using a pseudodensity (ρ') instead of the oil density (ρ_0):

$$\rho' = \frac{\rho_0}{B_0}\left(1 + 0.001R_G\right)^{-1} \tag{2.30}$$

$$B_0 = 0.972 + 0.00038 \left[2.4 R_G \left(\frac{G}{\rho_0} \right)^{\frac{1}{2}} + T + 17.8 \right]^{1.175} \tag{2.31}$$

The true density of oil with gas (in g/cc) can be calculated by

$$\rho_G = \left(\rho_0 + 0.0012 G R_G \right) / B_0 \tag{2.32}$$

Table 2.3 summarizes some of the reservoir conditions, rock properties, and fluid properties used in this chapter.

Table 2.3: Reservoir conditions, rock properties, and fluid properties used in modeling seismic velocities.

Rock/Fluid/Reservoir Parameter	Properties	
"Stiff" Rock	ϕ=0.15	Mineralogy=Quartz
	V_P(WSat)=4500 m/s	V_S(WSat)=2950 m/s
"Soft" Rock	ϕ=0.35	Mineralogy=Quartz
	V_P(WSat)=3000 m/s	V_S(WSat)=2500 m/s
Quartz	ρ=2650 kg/m^3	K=36.6 GPa, μ=45 GPa
Water	ρ=1000 kg/m^3	K=2.25 GPa
"Heavy" Oil	API=15	ρ=965 kg/m^3
	K=1.7856 GPa	GOR$_{max}$=56
"Medium" Oil	API=30	ρ=876 kg/m^3
	K=1.3380 GPa	GOR$_{max}$=88
"Light" Oil	API=45	ρ=800 kg/m^3
	K=1.1106 GPa	GOR$_{max}$=150
Gas	Gas gravity=0.6	ρ=126 kg/m^3
	K=0.0404 GPa	
Pressure	20 MPa	
Temperature	86^{o}C	

SEISMIC VELOCITIES

In this section, we present modeling results that demonstrate the seismic velocity difference between free and dissolved gas for various API oils and in different rocks. Figure 2.16 shows a mass balance of free gas and dissolved gas for 3 different oils. In each case, GOR

(in liters/liter) is the amount of dissolved gas, while S_g is the free gas saturation. The value of GOR at $S_g = 0$ corresponds to the GOR$_{max}$ for the particular API oil at a pressure of 20 MPa and a temperature of 86^{o}C. The heaviest oil (15 API) has a GOR$_{max}$ of 56, the 30 API oil has a GOR$_{max}$ of 88, and the lightest oil (40 API) has a GOR$_{max}$ of 150. Each point along the dotted line, for example, corresponds to the same total mass of gas, but with different ratios of free to dissolved gas. At GOR = 0, all the gas is free.

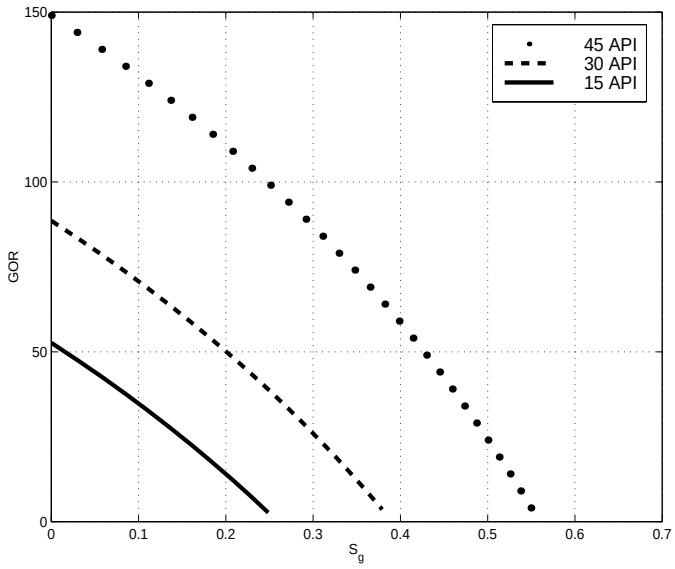

Figure 2.16: GOR vs S_g for 3 different oils: A mass balance of gas. Each curve corresponds to a constant mass of gas, but varying fractions of free and dissolved gas. The intercepts of each curve at $S_g = 0$ correspond to the maximum amount of gas that can be saturated in each oil. Lighter (higher API) oils can dissolve more gas than heavier (lower API) oils.

We modeled the seismic velocities of the oil and gas saturated rocks using both the "uniform saturation" model, which corresponds to very fine-scale mixing of the oil and free gas (Domenico, 1976), and the "patchy saturation" model, which corresponds to a coarse-scale mixing of the fluids (Mavko and Mukerji, 1998). In Figures 2.17 and 2.18 (which are explained in detail in the following sections), the lower curves correspond to fine-scale saturation, while the upper, more linear curves, correspond to patchy saturation.

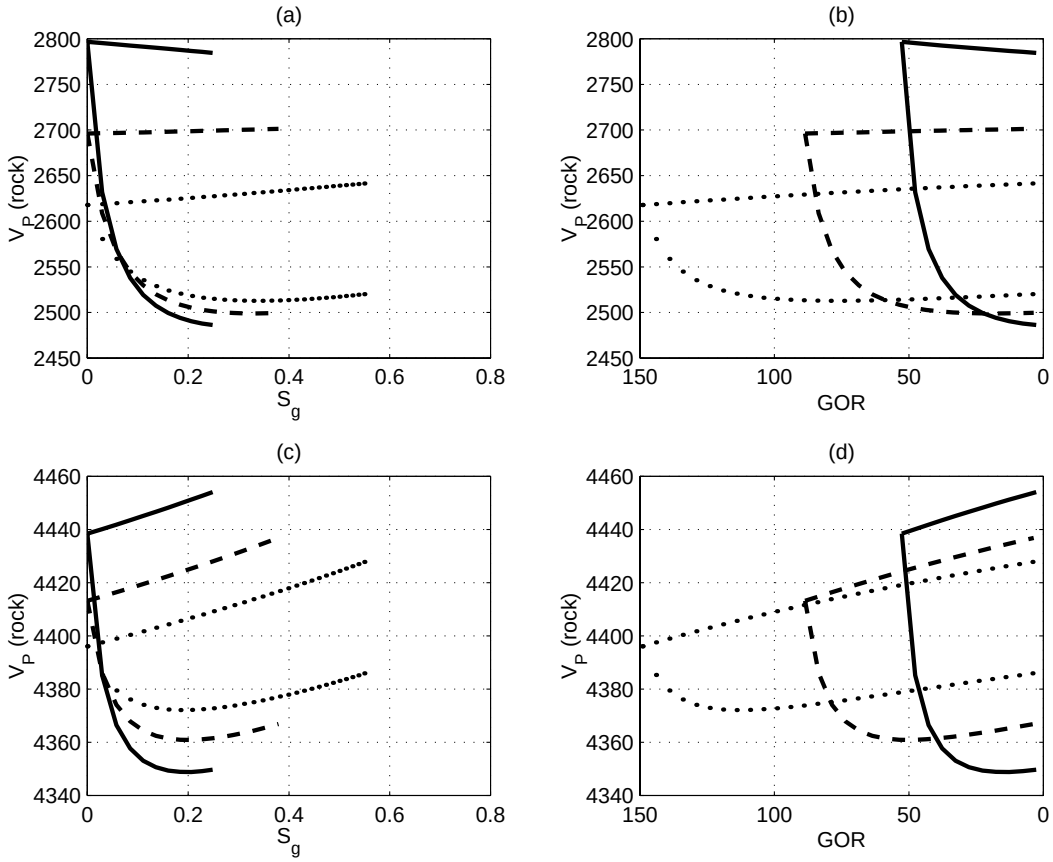

Figure 2.17: Seismic velocity of free gas versus dissolved gas when the mass of gas corresponds to the maximum GOR for each of the same 3 oils shown in Figure 2.16. (a) and (b): A soft rock, (c) and (d): A stiff rock. The lower non-linear curves indicate fine-scale mixing of the fluids while the upper linear curves indicate coarse-scale or patchy mixing of the fluids.

Gas Coming Out of Solution

In Figure 2.17 (a) and (b), the S_g and GOR are related by the conservation of total mass of gas (shown in Figure 2.16). Free gas saturation (S_g) increases at the expense of reduced dissolved gas (GOR). Figure 2.17(a) shows the variation in velocity in a soft sandstone with increasing amounts of free gas. When gas comes out of solution, it will most likely form gas bubbles in the oil, causing the fluids to mix together at a very fine scale (see Chapter 3.2 for details). Considering the fine-scale model (lower curves), the velocity drop is larger when free gas appears for a heavy oil (15 API) than for a lighter oil (45 API). Figure 2.17

(b) shows the same result plotted as a function of GOR.

Figures 2.17(c) and (d) are similar to Figures 2.17(a) and (b), except that the rock is stiffer in Figure 2.17(c) and (d), with a porosity of 0.15. As expected, the velocity drop with the appearance of free gas is smaller for the stiff rock (approximately 40 m/s for the 15 API oil) than for the soft rock (approximately 130 m/s for the 15 API oil). As in Figure 2.17(a) and (b), a larger drop occurs in V_P for a heavy oil (15 API) than for a light oil (45 API), due to dissolution of gas.

In both the soft and stiff rocks, for the fine-scale saturation model, the amount of free gas dominates the seismic velocities, and the oil API or the amount of dissolved gas has very little effect on the V_P. The oil API affects the seismic velocities only when the free gas saturation is zero or extremely low (below 0.01).

Gas Injection into Oil

When gas is injected into an oil reservoir, it could remain free, it could dissolve into the oil, or part of it could remain free while the other part dissolves in the oil. If all or some of the gas remains free, it could mix with the oil at a very fine scale (e.g., forming bubbles), or it could mix with the oil at a coarse scale (e.g., forming gas-caps). The seismic velocity will drop according to the distribution of gas in the reservoir.

Figure 2.18 (a) shows the various trajectories along which the seismic velocity can drop when gas in injected into a reservoir initially saturated with a dead oil of 15 API. If all the injected gas dissolves in the oil, the seismic velocity will drop $125m/s$ from the initial point A to point C in Figure 2.18 (a). In this case, the free-gas saturation remains zero, while the GOR increases from 0 to 52. At this point, the oil is fully saturated with gas, because the maximum GOR for a 15 API oil at a pressure of $20MPa$ and temperature of 80^oC is 52 (Equation (2.29)). Any more injected gas would therefore remain free.

If all the injected gas remains free, it can either mix with the oil at a fine scale by forming bubbles, or it can mix at a coarse scale, by forming gas-caps. If the free gas mixes with the oil at a fine scale, then the velocity will follow the uniform saturation curve and drop by a very large amount ($430m/s$), from A to D in Figure 2.18 (a). However, if the gas mixes with the oil in large patches, it will follow the patchy saturation curve and drop by a

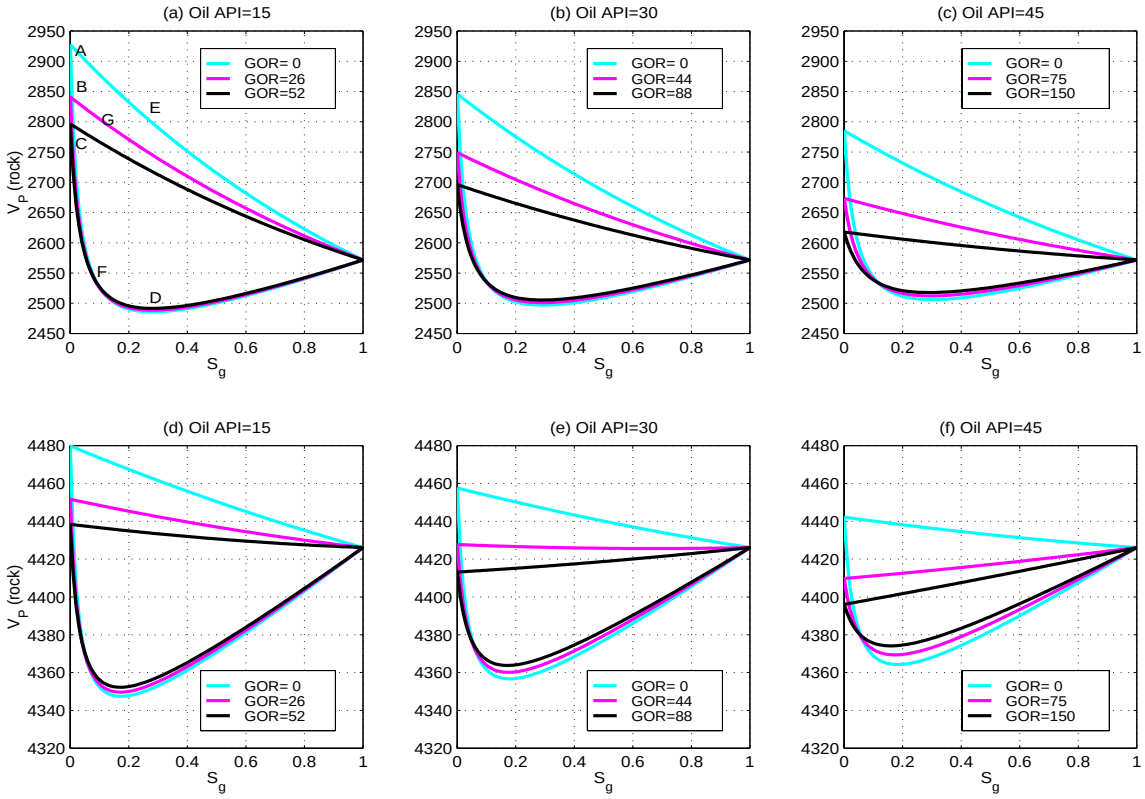

Figure 2.18: Seismic velocity of free versus dissolved gas for variable amounts of gas, and the same 3 oils in Figure 2.16. (a), (b), and (c): A soft rock, (d), (e), and (f): A stiff rock.

much smaller amount ($125m/s$), from A to E in Figure 2.18 (a).

If some of the gas initially dissolves in the oil, and some of it remains free, then the velocity might drop from A to B, and then either to G (for a patchy mix) or to F (for a fine-scale mix).

From Figure 2.18, we observe that if the injected gas is mixed with the oil at a fine scale in the reservoir, (i.e., uniform saturation), the rock velocities are dominated by the amount

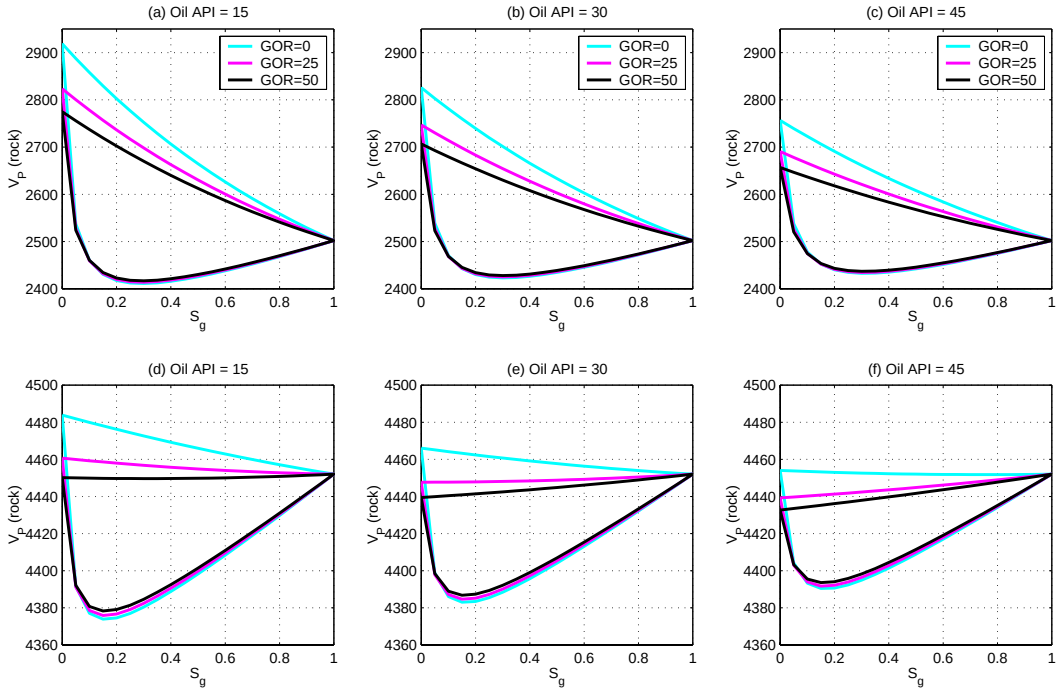

Figure 2.19: Seismic velocities of free versus dissolved gas, for fixed GOR's of 0, 25, and 50, and the same 3 oils in Figure 2.16. (a), (b), and (c): A soft rock, (d), (e), and (f): A stiff rock.

of free gas in the reservoir, and the effect of GOR is practically negligible.

However, when gas is injected into oil, we expect the gas to form gas-caps above the oil, often leading to patchy saturation (Chapter 3.2 contains details). For a patchy mix of the fluids, the GOR does cause some difference in the rock V_p. Lighter oils can dissolve more gas (have higher GOR_{max}). Therefore, there is a larger seismic difference between a rock containing fully saturated oil and a rock containing a mix of oil and free gas in case

of light oils.

For a fixed amount of gas, heavier oils show a larger seismic difference between free and dissolved gas. Referring back to Figure 2.16 we can observe that for all the 3 oils, if the GOR drops by 50, (e.g., from 150 to 100 for the 45 API oil), the S_g increases by 0.25. Figure 2.19 shows that, for a fixed about of gas, heavier oils show a larger seismic difference between free gas and dissolved gas. In Figure 2.19, the black curves correspond to GOR=50, the pink curves correspond to GOR=25, and the blue curves correspond to GOR=0. Figure 2.19 (a), (b), and (c) correspond to the same stiff rock shown in Figure 2.18 (a), (b), and (c). Figure 2.19 (d), (e), and (f) correspond to the same soft rock shown in Figure 2.19 (d), (e), and (f). In Figure 2.19 (a), the intersection of the black curves with the $S_g = 0$ axis corresponds to dissolved gas, and the intersection of the blue curve with the $S_g = 0.25$ axis corresponds to the same amount of free gas. The velocity difference between these two points is 360 m/s for a fine-scale mix of the fluids, and 100 m/s for a coarse-scale mix. In the same rock, and for the same amount of gas, the velocity difference between free and dissolved gas is 280 m/s for a fine-scale mix and 50 m/s for a patchy mix when the oil APi is 30 (Figure 2.19 (b)). When the oil API is 45 (Figure 2.19 (c)), the velocity difference is 230 m/s for a fine-scale mix and 40 m/s for a coarse-scale mix.

Figures 2.18 (d), (e), and (f) are similar to (a), (b), and (c), but the rock is stiffer. As expected, the drop in velocity is smaller in the stiff rock than in the soft rock. Figure 2.18 also shows that for a fixed GOR, heavy oils the seismic difference between dead oil and live oil does not change very much with the oil API.

All Rocks

We present in Figure 2.20 the results for all sandstones, i.e., for all combinations of V_P and porosity that lie between the Hashin-Shtrikman bounds (Hashin and Shtrikman, 1963). The dark black lines are the Hashin-Shtrikman bounds, while the dotted white line is the critical porosity line (Nur et al., 1995). Sandstones typically lie between the Hashin-Shtrikman lower bound and the critical porosity line.

We computed the V_P of rocks saturated with (i) dead oil, (ii) live oil at maximum GOR, and (iii) fluid mixture of dead oil and free gas (corresponding to the maximum GOR).

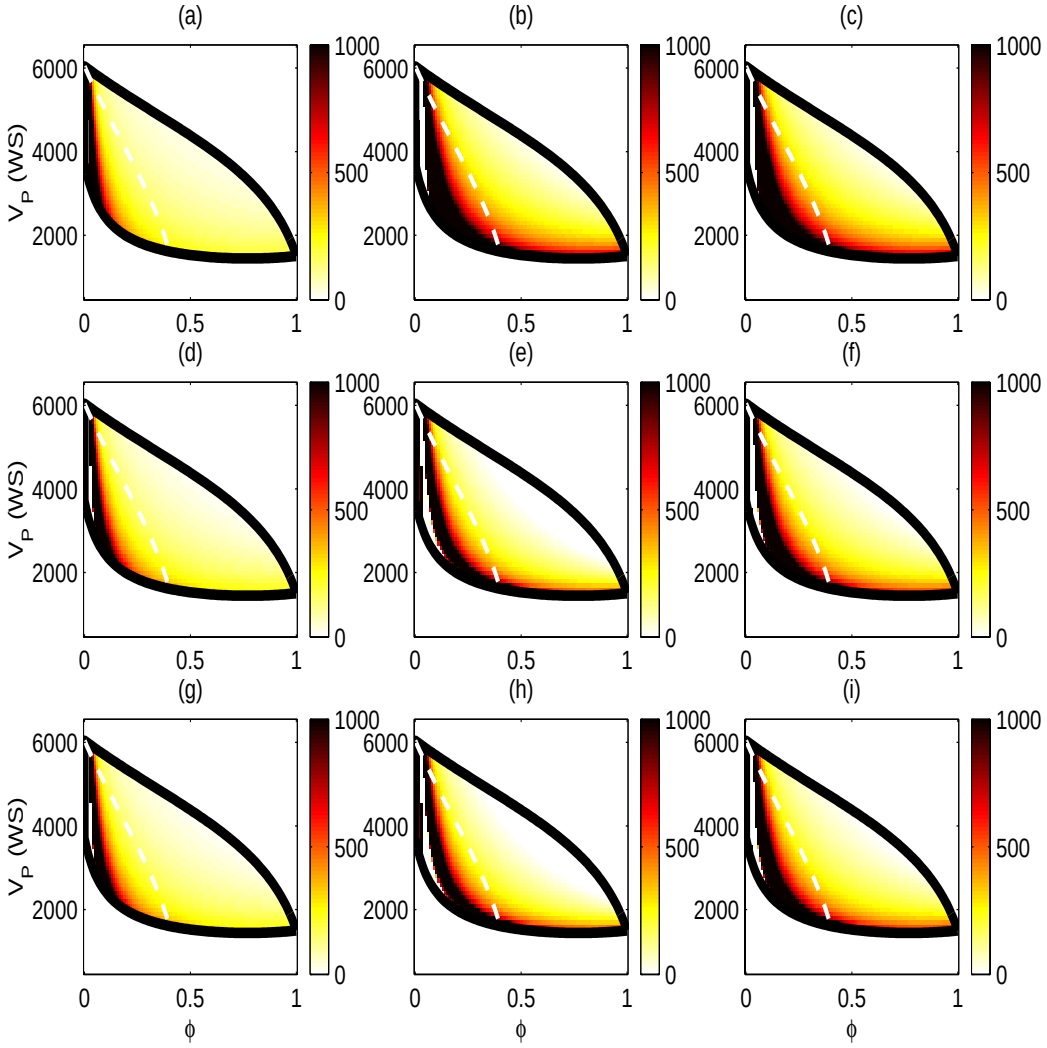

Figure 2.20: All rocks with quartz mineralogy: (a), (b), and (c) correspond to a 15 API oil. (d), (e), and (f) correspond to a 30 API oil. (g), (h), and (i) correspond to a 45 API oil. (a), (d), and (g) show the seismic difference between rocks containing only dead oil and fully saturated oil (GOR=GOR$_{max}$) but no free gas. (b), (e), and (h) show the seismic difference between the fully saturated oil and the dead oil mixed with free gas, where the free gas saturation corresponds to the maximum GOR of each oil. (c), (f), and (i) show the seismic difference between free gas and dissolved gas when all the oils mix with or dissolve the same fixed amount of gas.

We then plotted (ii)-(i) and (iii)-(ii) in Figure 2.20. Figures 2.20 (a), (d), and (g) show the resulting seismic difference between live oil and dead oil ((ii)-(i)), while Figures 2.20 (b), (e), and (h) show the resulting seismic difference between free gas and dissolved gas

((iii)-(ii)). We also computed the V_P of rocks saturated with GOR=50, and the V_P of rocks saturated with dead oil plus free gas corresponding to a GOR of 50. Figures 2.20 (c), (f), and (i) correspond to the seismic difference between free and dissolved gas for a fixed mass of gas. Figure 2.20 (a), (b), and (c) correspond to a 15 API oil, Figure 2.20 (d), (e), and (f) correspond to a 30 API oil, and Figure 2.20 (g), (h), and (i) correspond to a 45 API oil.

As Figure 2.20 shows, the softer rocks (which are close to the Hashin-Shtrikman lower bound) show a higher sensitivity to both the amount of gas dissolved in the oil and the free gas saturation than the stiff rocks. We also observe that heavy oils show a small difference between live oil and dead oil, while light oils show a large difference between live oil and dead oil. In contrast, heavy oils show a large difference between free gas and dissolved gas, while light oils show a small difference between free gas and dissolved gas.

CONCLUSIONS

We conclude from our studies that soft rocks are seismically more sensitive than stiff rocks for distinguishing free gas (gas-oil mix) from dissolved gas (gas-oil solution). When free gas is present, and the the oil is mixed with the gas at a fine scale (uniform saturation), the free gas saturation dominates the seismic velocities, and the oil properties (API, GOR) have negligible effect. When the fluids are mixed at coarse scales (patchy saturation), the oil properties and the dry rock properties play a larger role in determining the seismic velocities.

In the absence of free gas, rocks saturated with heavier oils show higher seismic velocities than rocks saturated with lighter oils when the oils are

- dead, i.e., contain no dissolved gas,
- live, containing a fixed amount of dissolved gas (e.g. GOR = 50), or
- saturated, i.e., containing the maximum possible amount of dissolved gas (GOR = GOR_{max}).

The seismic difference between a dead oil and a live oil at a given GOR (e.g. GOR = 50) is larger for a heavy oil than for a live oil, because, heavy oils, being much heavier

and stiffer than gas, show a higher sensitivity to dissolved gas for a given value of GOR. However, the seismic difference between a dead oil and a fully saturated oil (with GOR = GOR_{max}) is larger for a light oil than for a heavy oil, because light oils can dissolve more gas than heavier oils.

When gas comes out of solution, the free gas is most likely to form bubbles, i.e., mix at a fine scale with the oil (see Chapter 3.2). In such scenarios, the seismic velocity always drops, but the drop is larger in case of heavy oils than in case of light oils, for a given intial GOR. This also holds if the oil is initially at the maximum GOR.

A patchy mix of oil and gas can be expected when gas is injected into oil (see Chapter 3.2). When gas mixes at a coarse scale with an oil it shows a higher velocity than a fine-scale mix, but a patchy mix typically has almost the same seismic velocity as the gas-oil solution. The patchy mix of oil and free gas can have a slightly higher or slightly lower velocity than the corresponding gas-oil mix, but this difference is very small.

2.3 Sensitivity Studies in Forward AVO Modeling

ABSTRACT

Using a Monte Carlo approach, we quantify the uncertainty in the Amplitude Variation with Offset (AVO) response which results from uncertainties in rock and fluid properties. We can apply this methodology to assess the effectiveness of AVO analysis or even acquiring offset data to address problems using rock physics constraints. Our studies show that the uncertainty in the AVO response increases with decreasing rock stiffness. Although AVO anomalies are typically associated with lithology or fluid changes, we find that anisotropy can create or destroy AVO anomalies.

INTRODUCTION

AVO modeling is routinely used to high grade hydrocarbon prospects, assess the ability to differentiate hydrocarbon type, and examine the potential advantages of AVO. AVO is a function of compressional velocitiy (V_P), shear velocity (V_S), and density (ρ) contrasts, which in turn are functions of rock and fluid properties such as porosity (ϕ), clay content, bulk modulus of the dry rock (K_{dry}), fluid bulk moduli (K_{fl}), and fluid densities (ρ_{fl}). The AVO response is sensitive to uncertainties in these rock and fluid properties.

We numerically compute the uncertainty in the AVO signature given the uncertainties in the rock properties, which enables us to make a feasibility analysis of whether or not AVO will be successful for detecting and differentiating hydrocarbons in a particular area. We use this tool to quantify which parameters are critical in reducing uncertainties in AVO modeling.

In this study, we modeled each input parameter as an independent normal (Gaussian) random variable, with a given mean μ and standard deviation σ (or a percentage error which is set equal to 2σ). If any input parameter is known with absolute certainty, then its corresponding standard deviation is set to zero.

We first studied the impact of V_P, V_S, and ρ on AVO in isotropic, elastic media. We then studied the effect of uncertainties in the rock and fluid properties on the AVO response, by computing the uncertainties in the V_P, V_S, and ρ as a result of fluid substitution, and using the values obtained as inputs to AVO modeling. In the fluid substitution step, the results we obtained using the Monte Carlo approach agree well with the results we obtained using analytical techniques in Chapter 2.1. The Monte Carlo method is not only easy to use but is also powerful in practice, because it can take into account the statistical variation in the rock and fluid properties. Next, we applied the statistical forward modeling technique to well log data to perform a feasibility study for hydrocarbon detection using AVO. Finally, we studied the effect of ignoring uncertainty in the anisotropy on the AVO response. In our modeling, we assumed that the uncertainty in the individual rock parameters are independent of uncertainties in the other parameters.

Table 2.4: Case 1: Initial model parameters (mean (μ) and % error ($2\sigma/\mu$)) values used in statistical AVO modeling.

Layer	V_P (ft/s)	% Error	V_S (ft/s)	% Error	ρ (g/cc)	% Error
Cap rock	7800	2	3500	5	2.23	3
Reservoir	8300	3	4900	10	2.00	3

AVO MODELING IN ISOTROPIC MEDIA

The AVO response is sensitive to the V_P, V_S, and density of the cap rock and the reservoir rock. Our approach starts with a popular linearization of the Knotts-Zoepptritz equations (Aki and Richards, 1980)

$$R(\theta) = b_0 + b_1 tan^2(\theta) + b_2 tan^2(\theta) sin^2(\theta) \tag{2.33}$$

$$b_0 = \frac{\Delta Z_P}{2Z_P}, b_1 = \frac{\Delta V_P}{V_P} - 2\frac{V_S^2 \Delta\mu}{V_P^2 \mu}, b_2 = 2\frac{V_S^2 \Delta\mu}{V_P^2 \mu} \tag{2.34}$$

where Z_P is the acoustic impedance defined as $Z_P = \rho V_P$. The linearized equations give accurate results when the contrasts in V_P, V_S, and ρ are small, and for angles up to 30^o.

We examined the sensitivity of AVO for a class II type of reservoir, by modeling the input rock properties as gaussian random variables. Table 2.4 lists the parameters for the initial model, in which the uncertainties in V_P, V_S, and ρ are uncorrelated. The curves in Figure 2.21 are the various realizations of the AVO response when the inputs contain uncertainties. The uncertainties in the input parameters are indicated as a % of the mean value, and correspond to two standard deviations around the mean. The results indicate that uncertainty in V_P affects the reflectivity at all offsets, while uncertainty in V_S affects the reflectivity only at far offsets. Uncertainty in density affects the reflectivity at both near and far offsets, but it affects the near offsets more than the far offsets.

Figure 2.22, which displays the same AVO response as Figure 2.21 (d), shows the probability (in percentage) of the reflectivity at each offset. The color scale indicates probability values, which can be interpreted as the confidence in the AVO response. This figure shows that we have a greater confidence at the near offsets and increasing uncertainty at far offsets.

Figure 2.23 shows the uncertainty in the AVO response, with the same mean values of the V_P, V_S, and ρ of the cap rock and the reservoir as shown in Table 2.5. The mean values of the parameters are the same in cases 1 and 2, but the uncertainties are different. Figure 2.24 shows how the uncertainties in the inputs affect the b_0 (zero-offset reflectivity) and the b_1 (AVO gradient) terms. Each input "smears" the $b_0 - b_1$ cross plots in a particular way. We can see that uncertainty in V_P and density affect both terms, while uncertainty in V_S affects b_1 only. When there are uncertainties in all parameters, the $b_0 - b_1$ cross plots are scattered elliptically around the mean.

Table 2.5: Case 2: Model parameters (μ and $2\sigma/\mu$) used in statistical AVO modeling.

Layer	V_P (ft/s)	% Error	V_S (ft/s)	% Error	ρ (g/cc)	% Error
Cap rock	7800	5	3500	5	2.23	5
Reservoir	8300	5	4900	5	2.00	5

ROCK AND FLUID PROPERTIES

In this section we present results of linking uncertainties in rock and fluid properties to uncertainties in the AVO response. We first modeled the AVO response, along with the

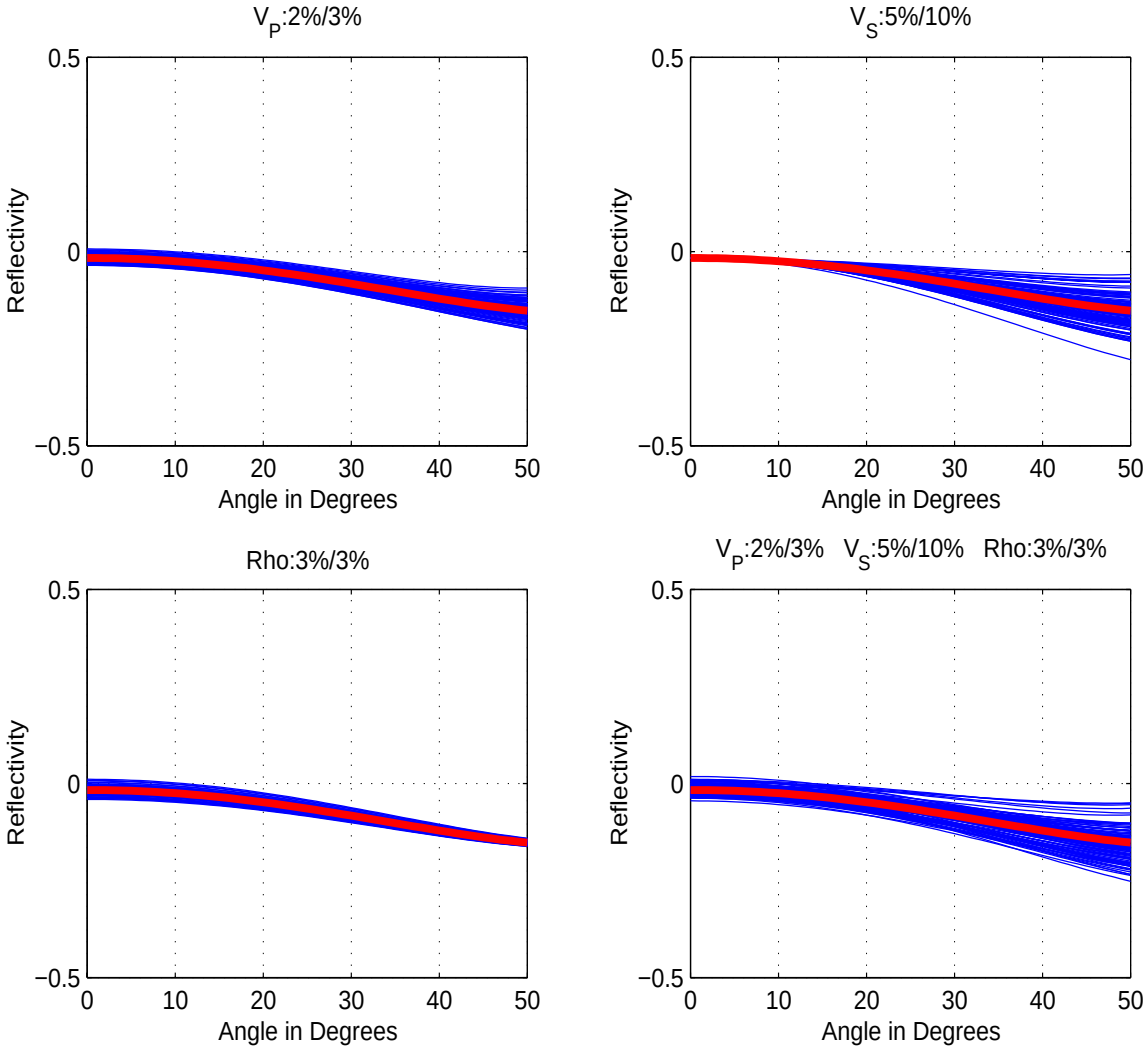

Figure 2.21: Sensitivity of AVO in isotropic media: case 1. The notation x %/y % refers to the uncertainty (equal to two standard deviations) in the cap and reservoir rock. The cap and reservoir properties and the uncertainties in them are also shown in Table 2.4. Top left: uncertainties in V_P only, Top right: unceratainties in V_S only, Bottom left: uncertainties in ρ only, Bottom right: uncertainties in V_P, V_S, and ρ.

corresponding uncertainties, of brine saturated sands. We then used Gassmann's fluid substitution equations (1951) along with the uncertainties in each input parameter to compute the V_P, V_S, and ρ of hydrocarbon saturated sands and the corresponding uncertainties in the velocities density. We used the values of the hydrocarbon saturated V_P, V_S, and ρ along

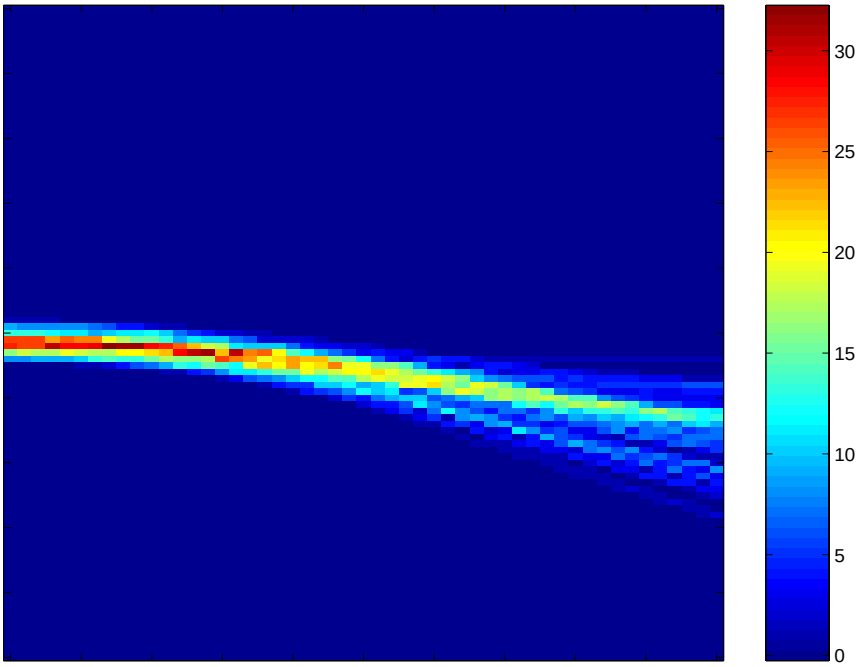

Figure 2.22: Quantifying Uncertainties in AVO: The rock properties and the uncertainties are given in Table 2.4. The reflectivity histograms are computed and displayed at each offset angle. Warmer colors correspond to higher frequency of occurrence, and therefore a higher probability.

with the corresponding uncertainties to compute various realizations of the AVO response of the hydrocarbon saturated rock.

We performed the modeling for two different rocks: a "stiff" rock and a "soft" rock. We started with the water saturated velocities, (along with the uncertainties in the rock and fluid properties) and computed the velocities of the hydrocarbon saturated rock using fluid substitution. The inputs for the fluid substitution recipe (listed in Tables 2.6 and 2.7) are: the compressional velocity (V_P) and shear velocity (V_S) of the rock saturated with the original fluid, the mineral bulk modulus (K_0), the porosity of the rock (ϕ), the original fluid bulk modulus (K_{fl_1}) and density (ρ_{fl_1}), and the new fluid bulk modulus (K_{fl_2}) and density (ρ_{fl_2}). We used Gassmann's equations of fluid substitution to calculate the bulk and shear moduli of the hydrocarbon saturated rock from the bulk and shear moduli of the

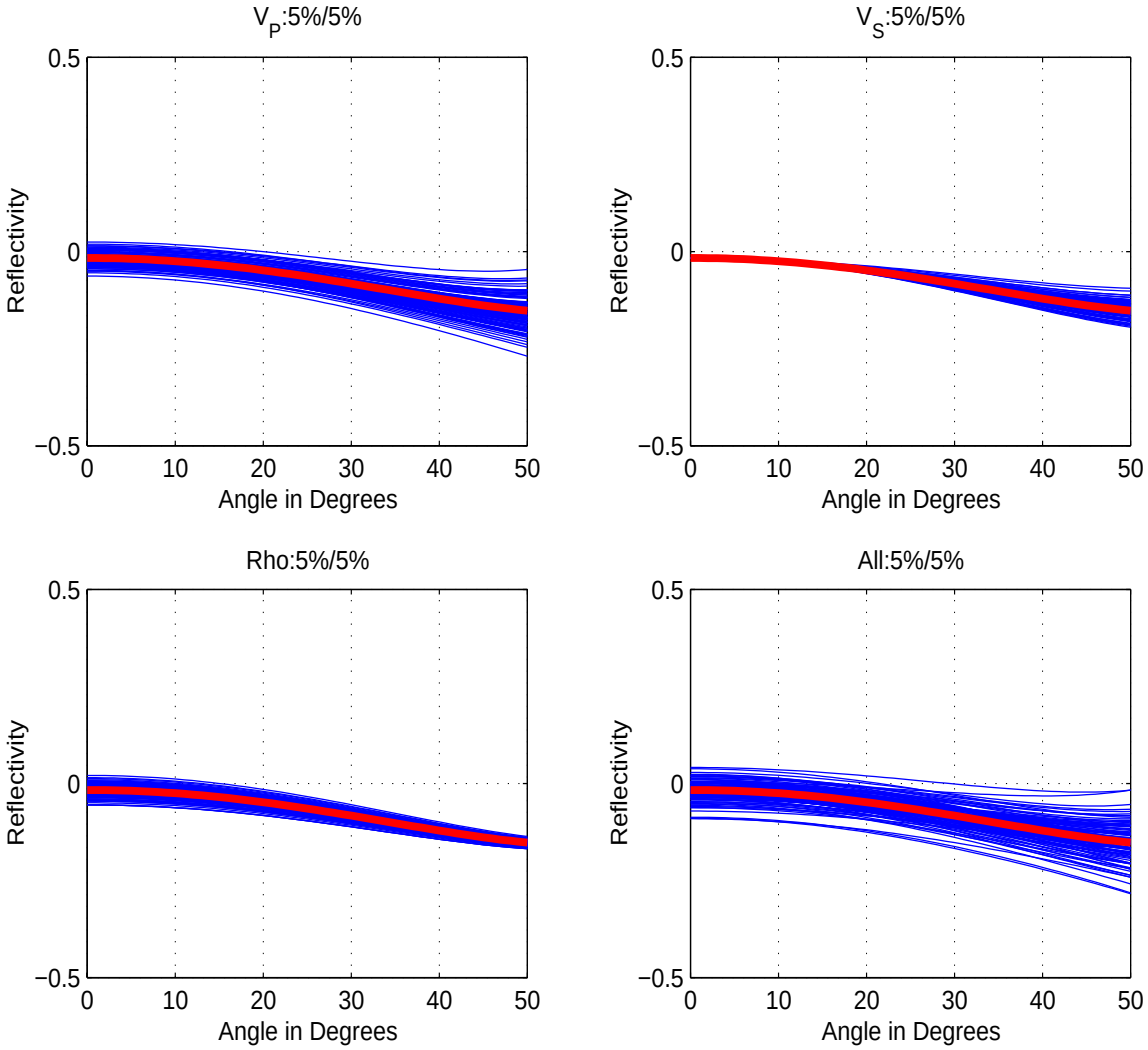

Figure 2.23: Sensitivity of AVO in isotropic media: case 2. The notation x %/ y % refers to uncertainties in the cap and reservoir rock. The parameters are given in Table 2.5. Top left: 5% uncertainty in V_P only: Top right: 5 % uncertainty in V_S only, Bottom left: 5 % uncertainty in ρ only, Bottom right: 5 % uncertainty in V_P, V_S, and ρ.

water saturated rock.

$$\frac{K_2}{K_2 - K_0} - \frac{K_{fl_2}}{\phi(K_{fl_2} - K_0)} = \frac{K_1}{K_1 - K_0} - \frac{K_{fl_1}}{\phi(K_{fl_1} - K_0)} \tag{2.35}$$

$$\mu_2 = \mu_1 \tag{2.36}$$

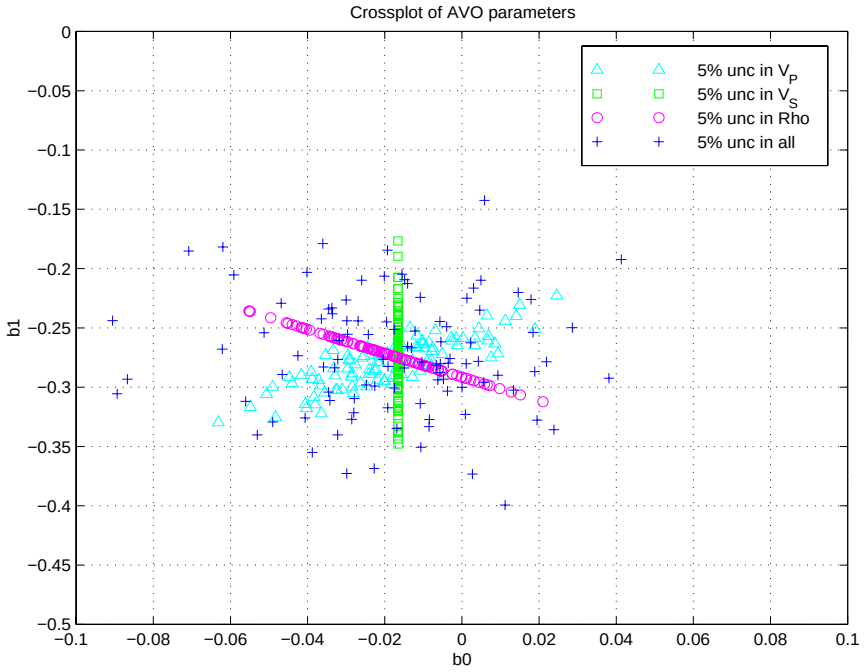

Figure 2.24: Case 2: Crossplot of AVO intercept versus the AVO gradient. The mean values and the uncertainties in the rock properties are the same as in Table 2.5 and Figure 2.23. The triangles correspond to 5 % uncertainty in V_P only, the squares correspond to 5 % uncertainty in V_S only, the circles correspond to 5 % uncertainty in ρ only, and the plus signs correspond to 5 % uncertainty in V_P, V_S, and ρ.

The subscript 1 refers to the properties of the rock saturated with water (fl_1), and 2 refers to the properties of the rock saturated with hydrocarbon (fl_2). The bulk density change is given by:

$$\rho_2 - \rho_1 = \phi(\rho_{fl_2} - \rho_{fl_1}) \tag{2.37}$$

We then calculated the V_P and V_S of the hydrocarbon saturated rock using the equations:

$$V_P = \sqrt{\frac{K + \frac{4}{3}\mu}{\rho}} \tag{2.38}$$

$$V_S = \sqrt{\frac{\mu}{\rho}} \tag{2.39}$$

The system of equations (2.35) through (2.39) form the fluid substitution recipe.

Table 2.6: "Stiff" rock: Input mean values and errors to Gassmann and corresponding outputs. WS indicates water saturated, and HS indicates hydrocarbon saturated values.

Input Parameter	Mean	% Error
V_P (WS)	2742 m/s	5
V_S (WS)	1433 m/s	10
ρ (WS)	2230 kg/m^3	5
ρ_W	992.2 kg/m^3	10
k_W	2.28x10^9	10
ρ_{HC}	721.8 kg/m^3	20
k_{HC}	0.476x10^9	20
k_{min}	32.68x10^9	15
ϕ	0.245	5
Output Parameter	**Mean**	**% Error**
V_P (HS)	2396 m/s	11
V_S (HS)	1454 m/s	10
ρ (HS)	2163 kg/m^3	6

Table 2.7: "Soft" rock: Input mean values and errors to Gassmann and corresponding outputs

Input Parameter	Mean	% Error
V_P (WS)	1462 m/s	5
V_S (WS)	366 m/s	10
ρ (WS)	2057 kg/m^3	5
ρ_W	991.3 kg/m^3	10
k_W	1.42x10^9	10
ρ_{HC}	909.8 kg/m^3	20
k_{HC}	0.572x10^9	20
k_{min}	32.68x10^9	15
ϕ	0.35	5
Output Parameter	**Mean**	**% Error**
V_P (HS)	1057 m/s	16
V_S (HS)	369 m/s	10
ρ (HS)	2057 kg/m^3	6

We computed the uncertainty in the V_P, V_S, and ρ in the hydrocarbon saturated rocks when there are uncertainties in each of the 9 inputs, as shown in Tables 2.6 and 2.7. These tables also show that the V_P, V_S, and ρ of the hydrocarbon saturated rocks have additional uncertainties as a result of fluid substitution. We modeled the AVO response, along with the uncertainties, of the brine saturated as well as the hydrocarbon saturated rocks. The parameters used in the AVO modeling are summarized in Table 2.8. We used the modeling results to test the the feasibility of using AVO for hydrocarbon detection in the two rocks, for the given uncertainties in the rock and fluid properties.

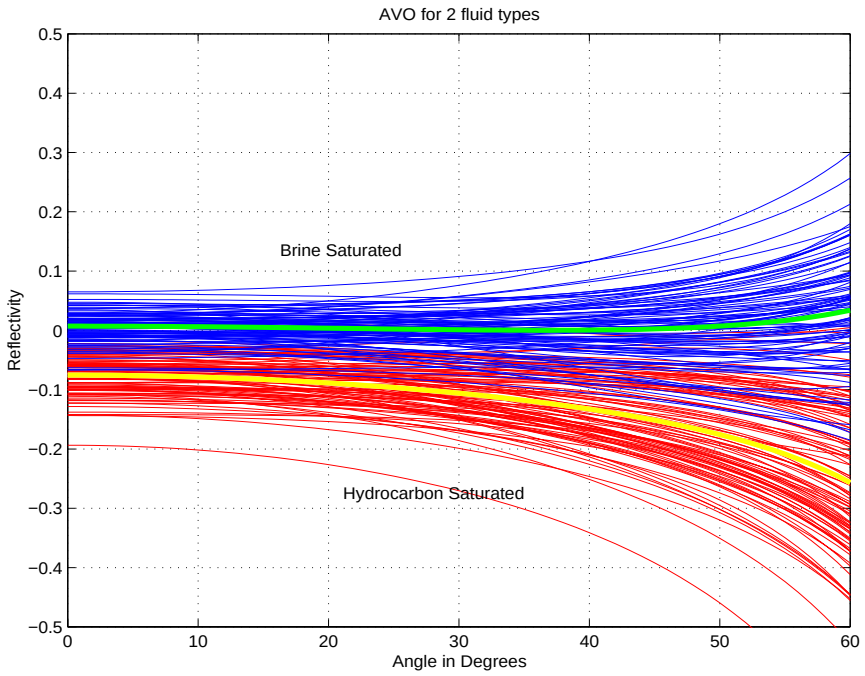

Figure 2.25: Stiff rock: Statistical realizations of AVO curves for brine and hydrocarbon saturated cases. The rock properties are given in Table 2.8.

Figure 2.25 shows the computed AVO response, along with the uncertainties, and Figure 2.26 shows the $b_0 - b_1$ crossplots. Figure 2.27 shows the AVO curves for the soft rock. Figure 2.28 shows the AVO crossplot for the soft rock. In Figures 2.26 and 2.28, the blue clouds correspond to the uncertianties in the brine saturated rock, and the red clouds correspond to uncertainties in the hydrocarbon saturated rock. The larger scatter in the red

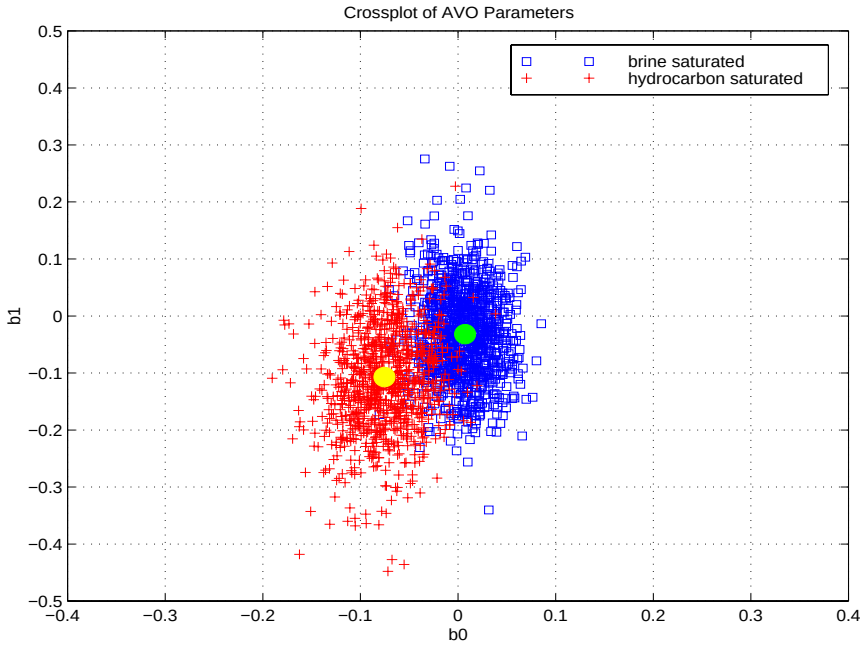

Figure 2.26: Stiff rock: Crossplot of AVO parameters. The rock properties, given in Table 2.8, are the same as in Figure 2.25

.

(hydrocarbon) points in Figure 2.28 shows that fluid substitution introduces more uncertainty in the soft rock than in the stiff rock. However, the stiff rock has a much larger overlap between the red and the blue clusters. We can qualitatively conclude from Figures 2.26 and 2.28 that the AVO parameters better separate the fluids in the soft rock than in the stiff rock. In a later section in this chapter (Bayesian Analysis of AVO classification) we quantitatively show that the AVO parameters are better separated in the soft rock than in the stiff rock.

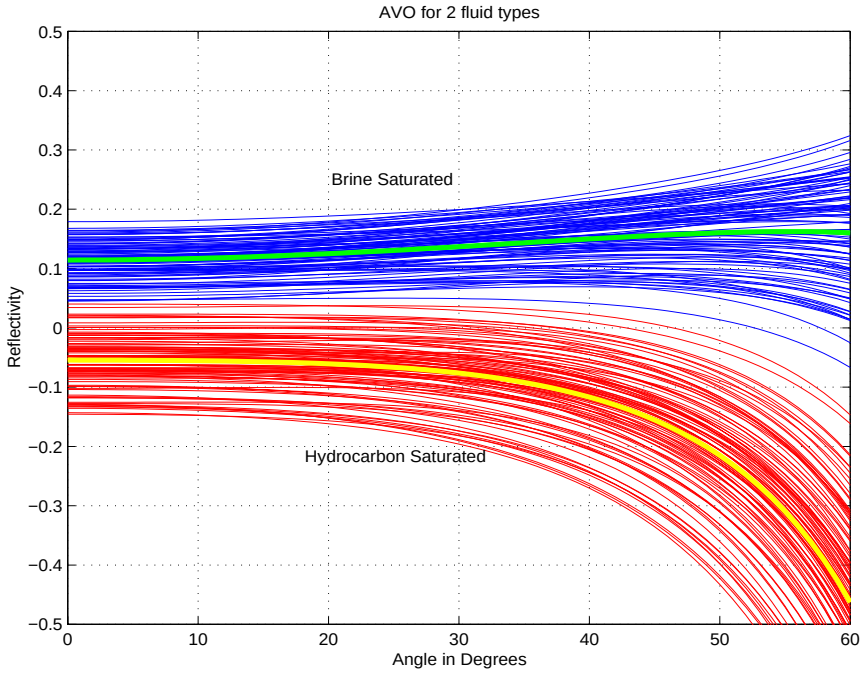

Figure 2.27: Soft rock: AVO curves for brine and hydrocarbon saturated cases. The rock properties are given in Table 2.8.

Table 2.8: Rock and fluid properties of the "stiff" rock and the "soft" rock used in AVO modeling. Each parameter is modeled as a gaussian random variable with a mean (μ) and a % error (given by $2\sigma/\mu$).

Rock	Parameter	V_P (m/s)	V_S (m/s)	ρ (kg/m^3)
Cap rock	Mean	2621	1341	2300
	Error	5%	10%	5%
Stiff rock (WS)	Mean	2742	1433	2230
	Error	5%	10%	5%
Stiff rock (HS)	Mean	2396	1454	2163
	Error	5%	10%	5%
Cap rock	Mean	1494	548	1600
	Error	5%	10%	5%
Soft rock (WS)	Mean	1462	366	2057
	Error	5%	10%	5%
Soft rock (HS)	Mean	1057	369	2028
	Error	5%	10%	5%

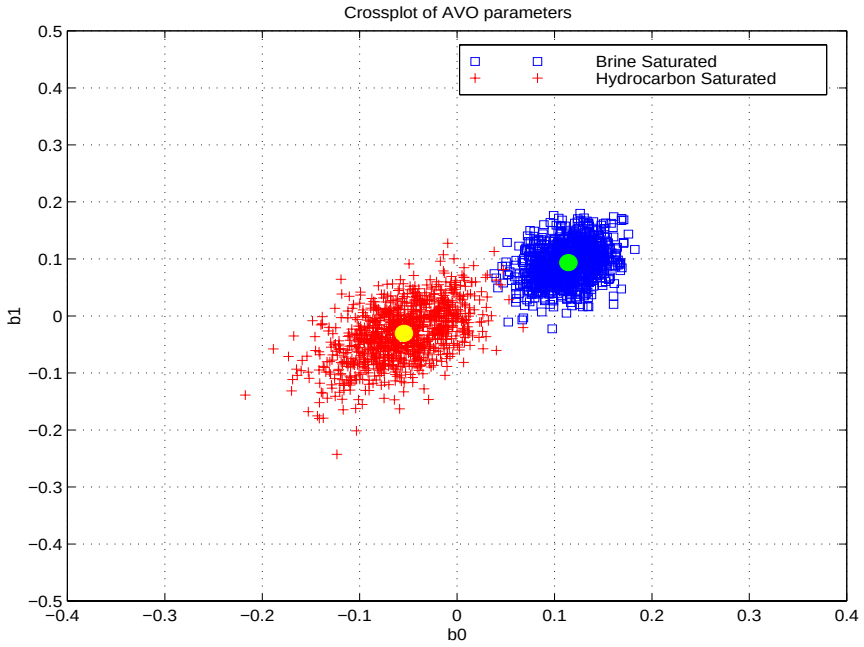

Figure 2.28: Soft rock: Crossplot of AVO parameters. The rock properties and uncertainties are the same as in Figure 2.27, and listed in Table 2.8.

AVO MODELING IN NORMALLY PRESSURED AND OVERPRESSURED REGIONS

In this case study, we obtained the mean values of the rock properties from trends observed in well-log data, and estimated the uncertainties by analyzing the scatter around these trends observed in the data. Thus, we can say that the uncertainties in the lithologic parameters in this case are mostly due to local heterogeneities. The mean values and errors of the model parameters used in the AVO modeling are shown in Table 2.8.

This approach ignores upscaling due to seismic wave propagation. (We account for seismic upscaling in Chapter 3.1 and 4.) We can expect that seismic wave propagation will have two competing effects. On one hand, it will have the effect of averaging over a large volume of rock, and therefore smooth out some of the extremes in the impedance, thus reducing the uncertainty. On the other hand, the process of extracting AVO parameters

from seismic data can introduce some uncertainty.

Table 2.9: Normal and overpressured rock properties: Mean values (μ) and % errors ($2\sigma/\mu$)

Layer	Pressure	V_P (m/s)	$\pm$ %	V_S (m/s)	$\pm$ %	ρ (g/cc)	$\pm$ %
Shale	normal	3795	10	1839	8	2.5	3
Brine Sand	normal	4100	8	2239	11	2.524	3
Gas Sand	normal	3368	8	2259	11	2.481	3
Shale	overpressure	3365	10	1550	7	2.395	2
Brine Sand	overpressure	3925	6	2150	9	2.357	3
Gas Sand	overpressure	3567	6	2199	9	2.268	3

Figure 2.29 shows the AVO signatures and the $b_0 - b_1$ cross plots in a normally pressured region and in an overpressured region. In this example, gas case is quite well separated from the brine case in the normally pressured region, but there is some overlap between brine and gas in the overpressured region.

Table 2.9 shows that the water saturated sandstone in the normal pressure region has higher V_P than the overlying shale, while the gas bearing sandstone has a lower V_P than the shale. However, in the overpressured region, the shale has a slower V_P than both the water saturated and the gas saturated sands. Since the bulk modulus of a gas is approximately equal to the applied gas pressure, a possible explanation is that the gas becomes less compressible in the overpressured region, and therefore appears more liquid-like. Also, the shale is very slow in the overpressured region, causing many of the gas sands to have positive reflection coefficients. In both the normal and overpressured regions, the shale has the lowest V_S, the gas saturated sand has the highest V_S, and the water saturated sand has an intermediate V_S. The shear wave contrast between the gas-saturated and brine-saturated rocks is always fairly small (which is understandable because fluids do not affect the shear moduli of rocks).

The crossplots in Figure 2.29 (c) and (d) show that the intercept term dominates the AVO response. The AVO gradient in both the normal and overpressured regions is somewhat sensitive to the fluids, but does not differ drastically from the gas to the water saturated rocks. The water-bearing sands have a positive intercept in both the normal and overpressured regions. The gas-sands have negative intercepts in the normal pressure region, thus

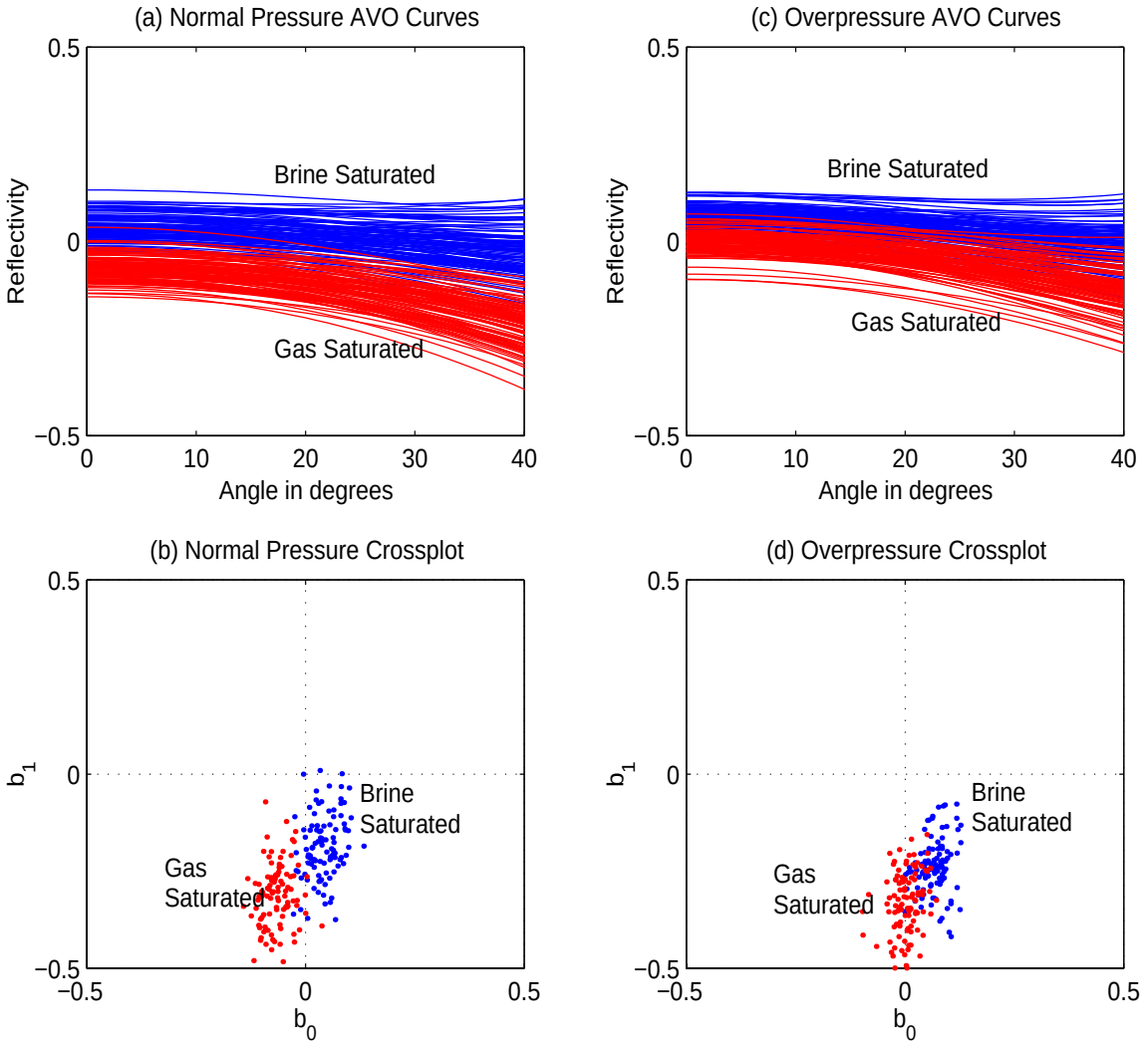

Figure 2.29: AVO as a fluid discriminator in normal and overpressured rocks

making them easy to discriminate from the water-sand. However, in the overpressured region, some of the gas-sands have positive intercepts, making them difficult to discriminate from the water-sands. Analysis of the AVO response in this area indicates that AVO will be very successful in discriminating gas zones in the normally pressured region, but less successful in the overpressured regions. We quantify the AVO success rate in the normal and overpressured regions in the next section.

BAYESIAN ANALYSIS OF AVO CLASSIFICATION

We classified the fluid-types from the AVO intercept and gradient terms using a Bayesian classification approach based on non-parametric bi-variate probability density functions (pdf's) (Mukerji et al., 2000). Figure 2.30 shows the bivariate joint distributions of the AVO intercept and gradient for the four different rocks discussed in the previous sections. The green pdf's correspond to the brine-saturated rocks, while the pink pdf's correspond to the hydrocarbon-saturated rocks. The joint pdf allows us to estimate Bayes risk and classification success rates (1 - Bayes risk) (Duda and Hart, 1973). Table 2.10 presents the Bayesian classification success rate for three different scenarios: using a single attribute, either the AVO intercept or the AVO gradient, and using both parameters together. We observe that the success rate of using AVO as a discriminatory tool is higher in the case of the soft rock (99.7 %) than in the case of the stiff rock (90.1 %). We also observe that the success rate is higher in the case of the normal pressure region (94.3 %) than in the overpressured region (88.1 %).

Table 2.10: Bayesian Analysis of AVO Classification

Rock Type	Classification parameters	Success Rate (%)
Stiff	b_0	88.6
	b_1	68.1
	$b_0 \& b_1$	90.1
Soft	b_0	98.5
	b_1	95.1
	$b_0 \& b_1$	99.7
Normal Pressure	b_0	93.5
	b_1	75.4
	$b_0 \& b_1$	94.3
Overpressure	b_0	86.9
	b_1	73.1
	$b_0 \& b_1$	88.1

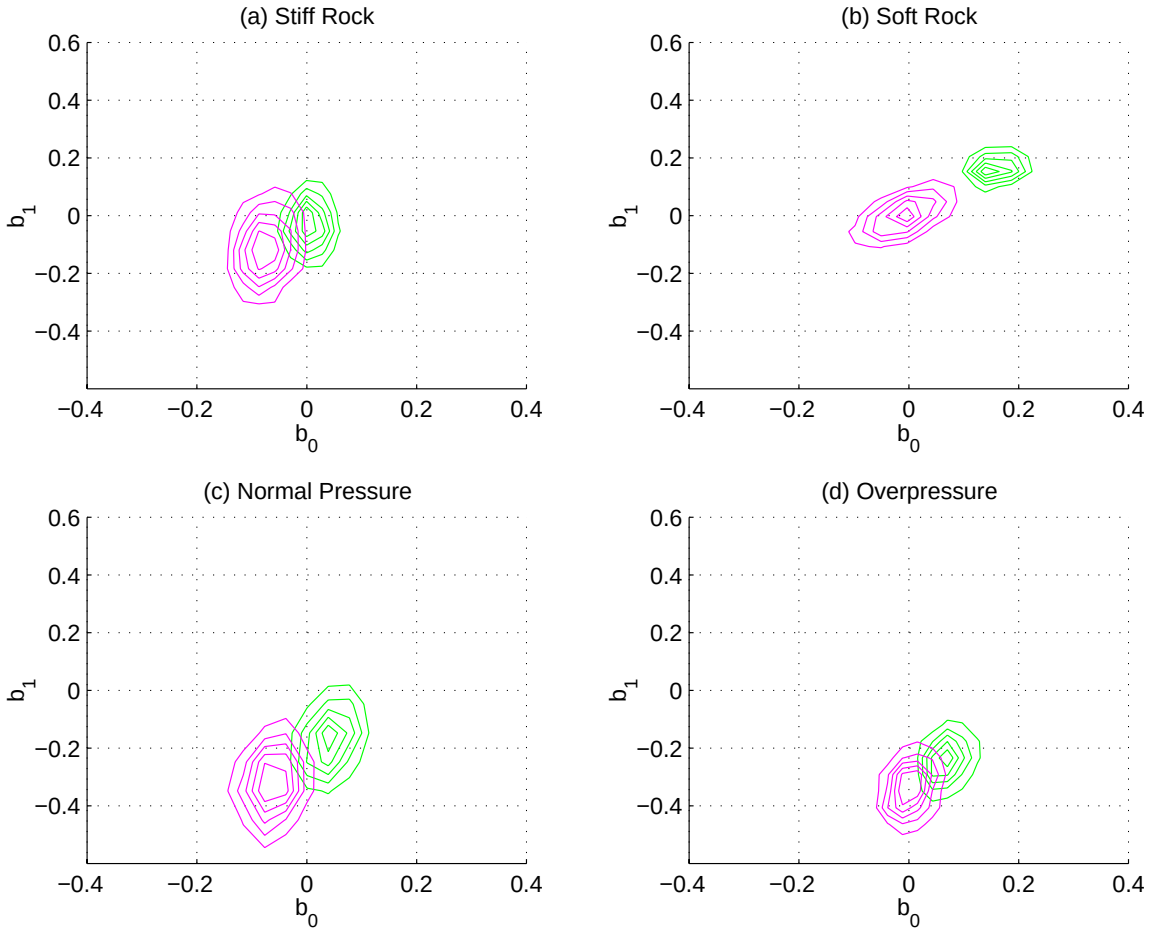

Figure 2.30: Quantifying the success rate of AVO as a tool for dicriminating fluids using probability density functions (pdf's) and Bayesian classification. (a) Pdf's of the brine-saturated (green) and hydrocarbon-saturated (pink) stiff rock corresponding to Figure 2.26, (b) Pdf's corresponding to the soft rock in Figure 2.28, (c) Pdf's of the normal pressure region, and (d) Pdf's of the overpressured region (Figure 2.29).

AVO MODELING IN ANISOTROPIC MEDIA

Extending our interests beyond the isotropic AVO considerations, we can ask what are the uncertainties of ignoring anisotropic effects on AVO. We know, from the parameterization, that anisotropy affects the offset terms and in particular the gradient term. The AVO signature in transversely anisotropic rocks depend on V_P, V_S, density and the Thomsen's anisotropy parameters δ and ϵ (1993, 1995). The equations used to calculate the AVO

response in anisotropic media are given below (Thomsen, 1993):

$$R(\theta) = b_0 + b_1 tan^2(\theta) + b_2 tan^2(\theta) sin^2(\theta) \tag{2.40}$$

$$b_0 = \frac{\Delta Z_P}{2Z_P}, b_1 = \frac{\Delta V_P}{V_P} - 2\frac{V_S^2 \Delta\mu}{V_P^2 \mu} + \frac{1}{2}(\delta_2 - \delta_1), b_2 = 2\frac{V_S^2 \Delta\mu}{V_P^2 \mu} + \frac{1}{2}(\epsilon_2 - \epsilon_1) \tag{2.41}$$

Figure 2.31 shows that when reasonable values of anisotropic parameters are included in AVO considerations, they can have profound effects. Since these parameters are so ill constrained, we allowed both δ and ϵ to vary $\pm 20\%$. The blue curves correspond to the isotropic case, and the pink curves correspond to the anisotropic case. This figure also shows the corresponding scatter on the $b_0 - b_1$, $b_1 - b_2$, and $b_0 - b_2$ cross plots. Since to first order, the contribution of anisotropy to reflectivity is directly proportional to the contrast in anisotropy across an interface, a 10 to 20 % anisotropy can completely mask or reinforce AVO anomalies arising, for example, from pore-fluids. Without quantification of the exact magnitude of anisotropy, it remains a very convenient excuse when AVO observations are different from expectations.

Table 2.11: Parameters (μ and $2\sigma/\mu$) used in statistical AVO modeling of anisotropic media.

Layer	V_P (ft/s)	% Error	V_S (ft/s)	% Error	ρ (g/cc)	% Error
Cap rock	7800	2	3500	5	2.23	2
Reservoir	8300	2	4900	5	2.00	2

CONCLUSIONS

AVO modeling coupled with realistic rock physics constraints and uncertainties permits the rapid assessment of applicability and feasibility. Clearly, other real world problems such as tuning, attenuation, noise, velocity gradients, and unknown anisotropy only make the problem worse. We can apply this method in quantifying the feasibility of using AVO as a discriminatory tool, and thus determine the additional value of acquiring far offset data.

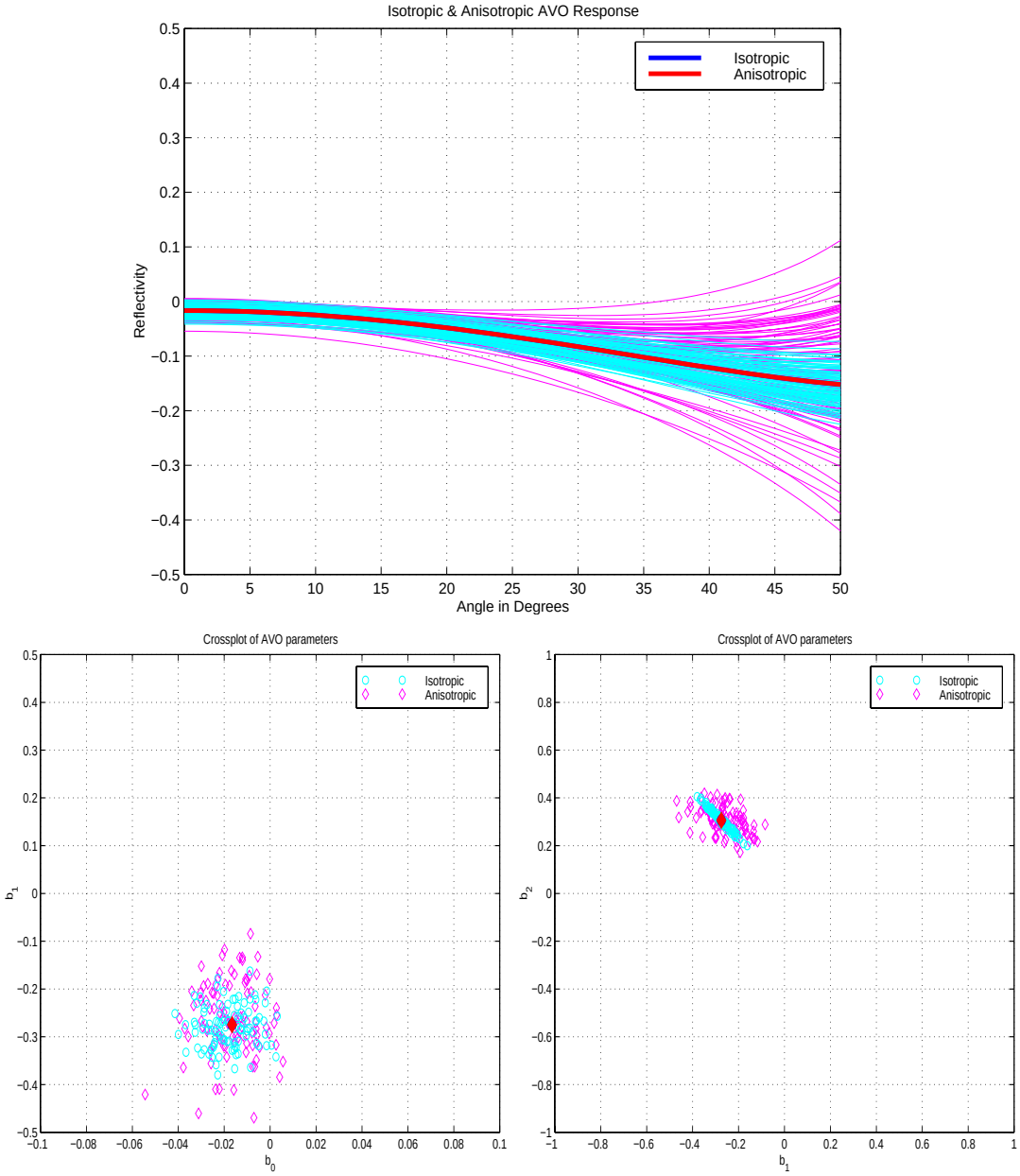

Figure 2.31: AVO modeling in anisotropic media. The mean (μ) and % errors ($2\sigma/\mu$) of the V_P, V_S, and ρ of the cap and the reservoir rocks are given in Table 2.11. The blue colors correspond to the isotropic case, while the pink colors correspond to the anisotropic case, with δ of $0.1 \pm 20\%$ and ϵ of $0.1 \pm 20\%$ in both the cap and the reservoir rocks. The crossplots of $b_0 - b_1$ and $b_1 - b_2$ show that the anisotropic case has a much larger scatter than the isotropic case.

Chapter 3

SATURATION SCALES

3.1 Seismic Forward Modeling of Saturation Scales

ABSTRACT

We investigate the effect of saturation scales on reflection properties using the Kennet algorithm to compute synthetic seismograms for 1-D layered media. We identify three saturation scales, (a) larger than the seismic wavelength (i.e. resolvable), (b) smaller than the seismic wavelength but larger than the characteristic diffusion length, and (c) smaller than the characteristic diffusion length. When the saturation scale is in the range (a), the seismic reflectivity can be modeled by the ray-theory equations. In case (b), the reflectivity can be modeled using effective medium theory. We call case (b) a patchy saturation model. For case (c), the reflectivity can be computed using the effective fluid model, and we call this a uniform saturation model.

INTRODUCTION

The sensitivity of seismic velocities to pore fluids has been recognized for years (Gassmann, 1951, Nur and Simmons, 1969). Less widely known is that seismic velocities depend not only on the types and saturations of the pore fluids (water, oil, gas), but also on the spatial scales of heterogeneous fluid distributions (White, 1975). Spatially varying saturations give rise to wave-induced pore pressure gradients, which in turn cause wave attenuation and velocity dispersion (Akbar et al., 1994).

The effects of saturation scales on transmission properties of rocks (i.e., velocities), have been studied both theoretically (White, 1975, Dutta and Odé, 1979, Mavko and Nolen-Hoeksema, 1994, Akbar et al., 1994, Packwood and Mavko, 1995, Gurevich and Zyrianov, 1995) and experimentally (Knight et al., 1995, Cadoret, 1993). Our objective in this chapter is to quantify the impact of saturation scales on reflection properties. For example, is the reflected signal sensitive to the scales of saturation heterogeneity? Can we replace a medium with heterogeneous saturations by an effective

homogeneous medium that has the same seismic reflectivity? Our approach is to model synthetic seismograms numerically in one-dimensional layered media corresponding to different saturation scenarios.

RELEVANT SCALES

When the distribution of water-oil-gas phases is spatially heterogeneous, we can identify three limiting ranges of scale, each with its own distinct velocity and reflectivity signature. The critical factor determining these ranges is the characteristic size, d, of the saturation heterogeneity, or saturation "patch".

The first criterion is resolution. If the patch size is comparable to or larger than the seismic wavelength, λ, then the patches can be directly resolved ($\lambda < d$). In principle, we can see regions of different fluid saturation directly on the seismic image, depending, of course, on the sensitivity of velocity and impedance to pore fluids.

When the patch size is smaller than a quarter of the seismic wavelength ($d < \lambda/4$), the individual patches cannot be resolved, but still influence velocity and impedance. Sub-resolution patches are divided into two additional ranges, known as the unrelaxed and the relaxed states, dictated by the hydraulic diffusivity and characteristic diffusion length of the medium. The diffusion length can be estimated approximately as

$$L_c = \sqrt{D/f} \tag{3.1}$$

where D is the hydraulic diffusivity and f is the seismic frequency. When the characteristic scale of the subresolution saturation heterogeneities, or "patch size", is small compared to the diffusion length (L_c), then any wave-induced differences in pore pressure between the different fluid phases have sufficient time during a seismic period to flow and equilibriate. The equilibration of pore pressures allows us to replace the mixture of phases with an effective fluid having bulk modulus K_f and density ρ given by

$$\frac{1}{K_f} = \sum_i \frac{S_i}{K_i}$$

$$\rho_f = \sum_i S_i \rho_i \tag{3.2}$$

where S_i, K_i, ρ_i, are the saturation, bulk modulus, and density of each phase (Domenico, 1976). The effective velocity of a rock with this mixture of phases can be estimated by substituting this effective fluid into Gassmann's (1951) relations. We call this the "effective medium relaxed" state.

There is a less well recognized intermediate scale between the ray theory (resolvable) and the effective medium relaxed limits. When the patch size is still much smaller than the seismic wavelength but larger than the diffusion length, L_c, then there is not enough time during a seismic period for wave-induced pressure gradients to equilibrate between the pore fluid phases. In this case, the effective fluid description given by Equation (3.2) is no longer appropriate. Instead, when each of the phases is well separated over scales $> L_c$, the effective moduli of the rock can be estimated with the equation from Hill's equation (Hill, 1963):

$$\frac{1}{K + \frac{4}{3}\mu} = \left\langle \frac{1}{K_{sat} + \frac{4}{3}\mu} \right\rangle \tag{3.3}$$

where K and μ are the effective bulk and shear moduli of the rock, K_{sat} is the saturated rock bulk modulus within each of the saturation patches (water, oil, and gas) computed with Gassmann's relations, and $\langle\rangle$ designates a volumetric average. The shear modulus is independent of saturation in this low frequency limit. We call this the "effective medium unrelaxed" state. P-wave velocity in the unrelaxed state is always larger than the velocity in the relaxed state, given the same saturations. Equation (3.3) assumes a homogeneous dry rock and is valid for any arbitrary saturation patch shape. To summarize, the three different saturation scales we explore in this chapter are

- $d > \lambda$, resolvable patches,
- $\lambda > d > L_c$, effective medium unrelaxed,
- $d < L_c$, effective medium relaxed.

SYNTHETIC SEISMOGRAMS FOR HETEROGENEOUS SATURATIONS

Figure 3.1 illustrates the velocity signature over the transition from to $d > \lambda$ to $d < L_c$ for a layered medium. The velocities were obtained from the experimental observations of normal incidence waves in periodic layered media (Marion et al., 1994). The observed velocities approach the ray theory value in the limit of small λ/d and the slower effective medium theory value in the limit of large λ/d. In the limits, the velocity is easily quantified as averaging layer slownesses versus averaging compliance (Mukerji et al., 1995). If the periodic spacing d is a multiple of one-half wavelength, multiple reflections are in phase and add constructively. When this Bragg scattering condition is satisfied, the result is a large total reflection. Even for non-periodic media, constructive interference can give rise to the well-known "tuning" effects that lead to large observed amplitudes. In this chapter, we study the case where the laminations are due to layered saturations.

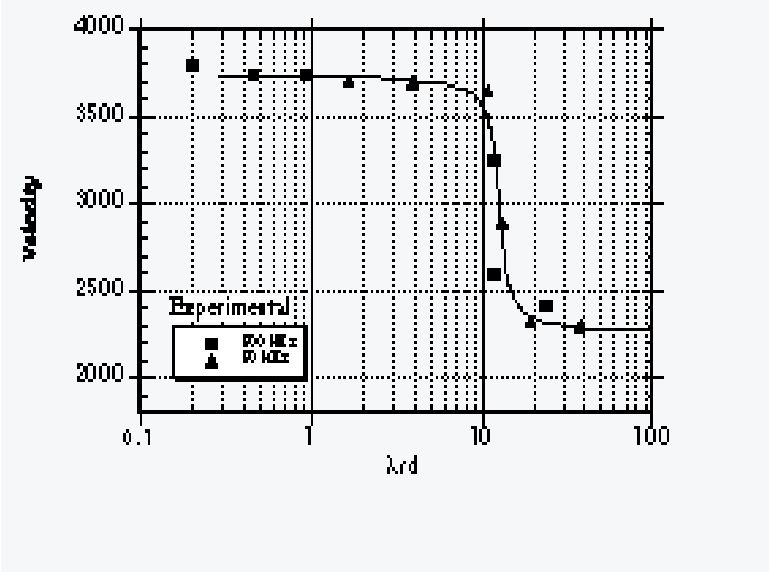

Figure 3.1: Experimental velocity versus λ/d.

Using the Kennett (1983) algorithm, we computed synthetic reflection seismograms for plane waves normally incident on a layered medium, We considered a homogeneous rock

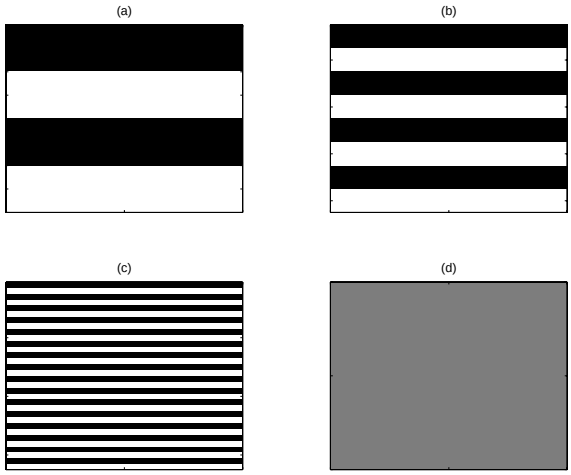

Figure 3.2: Patchy saturation at various scales and uniform saturation models. (a) $d > \lambda$, patchy unrelaxed, short wavelength (ray theory) limit. (b) $d \approx \lambda$, patchy unrelaxed, transition between short wavelength and long wavelength limits. (c) $L_c < d << \lambda$, patchy unrelaxed, effective medium limit. (d) $d << \lambda$, $d < L_c$, effective medium relaxed, or uniform saturation.

with heterogeneous spatial distribution of pore fluids. The heterogeneous saturations were modeled as alternating periodic layers of dry and water-saturated rock with 35% porosity. The mineralogy was assumed to be quartz, and the dry rock properties were taken to be representative of reservoir sandstones, with a porosity of 35%, a P-wave velocity of 1740 m/s, and an S-wave velocity of 1180 m/s. The water-saturated velocities within the saturated layers were computed using Gassmann's (1951) equation. The relaxed, uniform saturation was modeled using the same mineralogy and porosity, but with an effective pore fluid obtained from the Reuss average (1929) of water and air (Equation (3.2)). The saturation scale relative to the seismic wavelength (λ) was varied by changing the thickness of the layers while keeping the overall saturation and the total path length constant. This is shown schematically in Figure 3.2. Reflection seismograms were computed for a range of values of λ/d from 0.25 to 125. The overall saturation was fixed at 80%.

Synthetic reflection seismograms for selected values of λ/d are shown in Figure 3.3. In each case the first event (event A) at about 0.07 s is the reflection from the interface between the overburden and the saturated layered medium. Figure 3.3 (a) shows that for wavelengths much smaller than the patch size, the individual patches (layers) can be seismically resolved

(events B). Event C represents the reflection from the half-space below the saturated layered medium. This is the short wavelength limit. When $\lambda = d$ (Figure 3.3 (b)) we see, as expected, strong scattering effects due to the large number of alternating saturated and dry layers. The individual layers are still just barely resolvable.

At the effective medium limit, where the wavelength exceeds the patch size (Figures 3.3 (c) and 3.3 (d)), the individual layers are no longer resolvable. However, the effective velocities and traveltimes depend on whether the fluids are unrelaxed (Figure 3.3 (c)) or relaxed (Figure 3.3 (d)). Figure 3.3 (d) corresponds to the case where the layers are thin enough or the permeability is high enough for fluid patches (if present) to relax during a seismic period so that we have a uniform saturation throughout the rock. Notice the difference in the arrival time of event C in Figures 3.3 (c) and 3.3 (d). Again, this event represents the reflection from the half-space below the saturated layered medium. In the unrelaxed situation, event C arrives earlier (≈ 0.26 s) than for the relaxed uniform saturation (≈ 0.31 s). Figure 3.4 shows normal incidence reflection seismograms computed for the heterogeneous subresolution saturations with the seismogram for a single homogeneous effective medium obtained from Equation (3.3). The two seismograms are very similar, both in first arrival times and amplitude of the first arrival. Therefore, at long wavelengths we can replace the patchy unrelaxed medium consisting of fine-scale heterogeneous saturations by an effective homogeneous medium.

SCALE DEPENDENT VELOCITIES AND REFLECTIVITIES

Arrival times and amplitudes picked from the synthetic seismograms were used to obtain the transmission velocities and reflectivities for the various scales of saturation. The velocity and reflectivity change as the patch size changes from large (ray theory limit) to small (effective medium unrelaxed). They also change as the saturation scale decreases from the coarse-scale or unrelaxed patchy saturation to the fine-scale or relaxed uniform saturation. Figure 3.5 shows the dependence of seismic velocity on λ/d.

The first transition, which occurs at about $\lambda \approx d$, is due to the transition from the ray

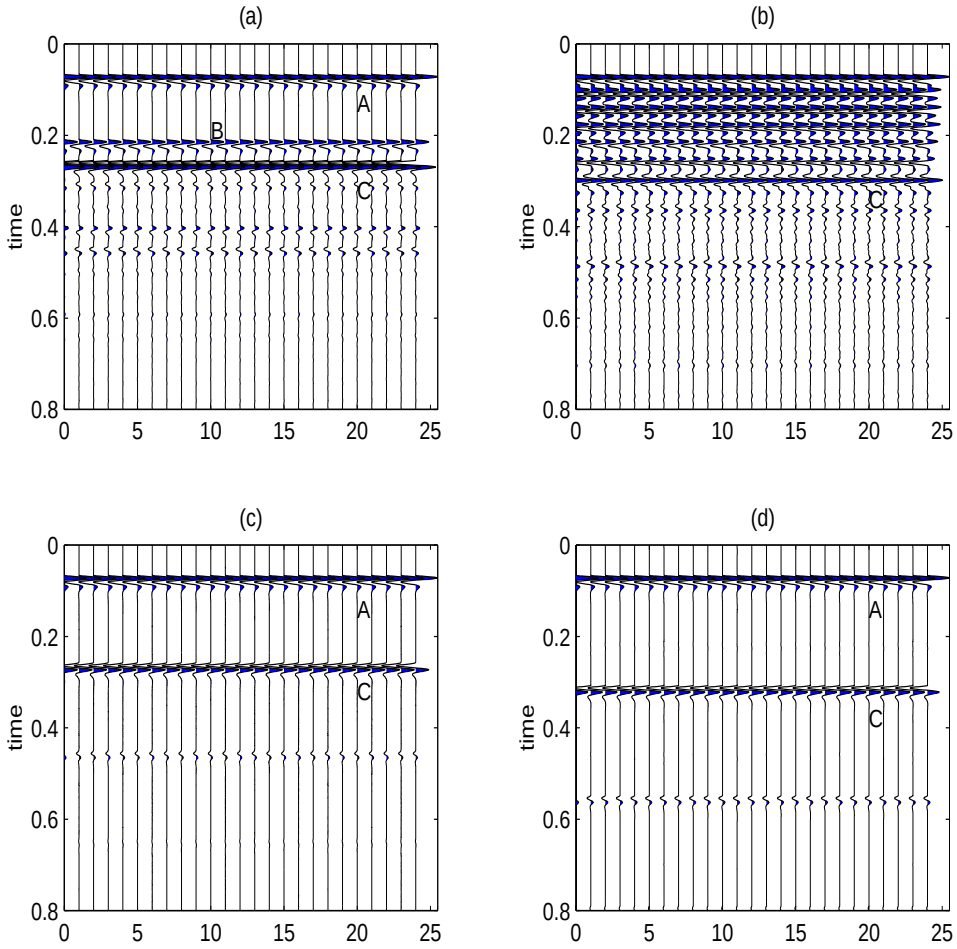

Figure 3.3: Seismograms computed using the Kennet algorithm: (a) $\lambda/d = 0.2$, (b) $\lambda/d = 1$, (c) $\lambda/d = 20$, (d) relaxed, uniform saturation.

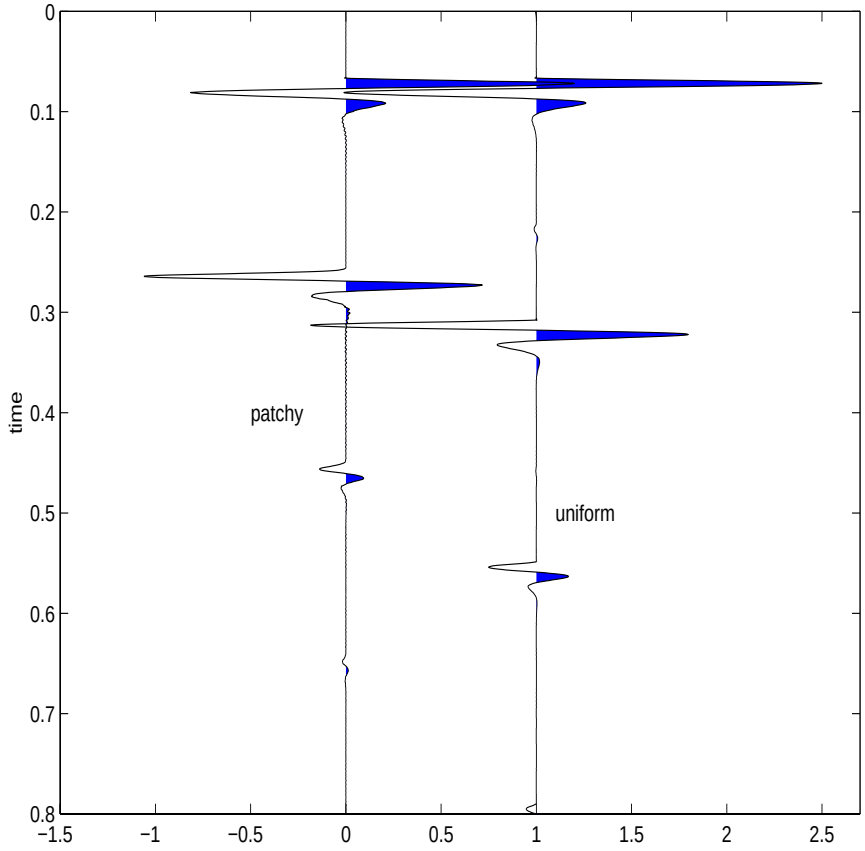

Figure 3.4: Comparison of normal incidence reflection seismograms computed for the heterogeneous subresolution patchy saturations (dashed line) with the seismogram for a single homogeneous effective medium obtained from equation (3.3) (solid line). The seismograms have been shifted horizontally by a constant value for purposes of depiction.

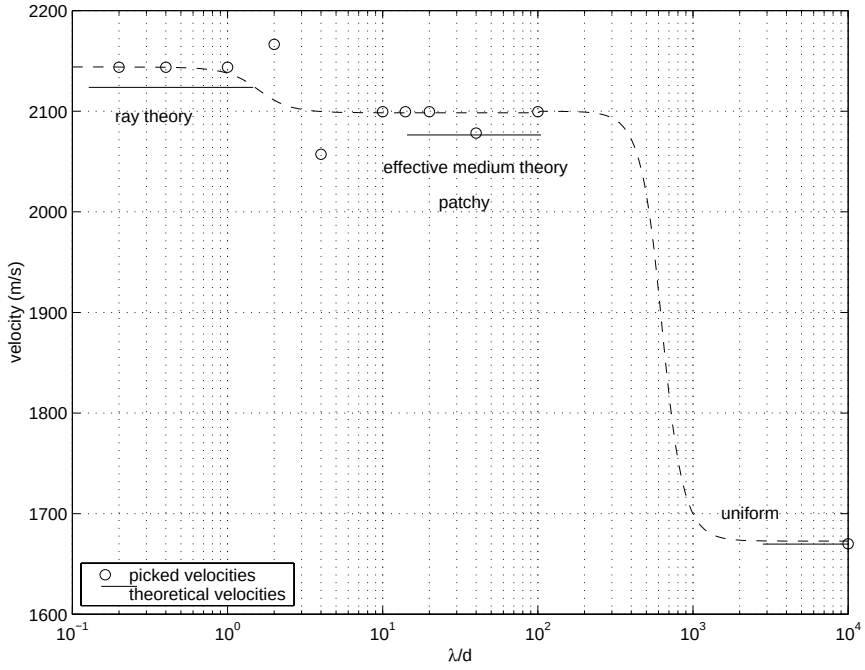

Figure 3.5: The "double S curve" – velocity versus λ/d. Horizontal lines show theoretical values.

theory limit to the effective medium unrelaxed limit. The seismic velocity is close to the ray theory velocity given by

$$\frac{1}{V_{RT}} = \frac{f_i}{V_i} \tag{3.4}$$

Here, f_i are the fractional patch sizes and V_i are the velocities within each patch. When the patch size d is such that $\lambda/d > 1$, and $d = L_c$, (effective medium unrelaxed), the velocities obtained from the numerical wave propagation results are slower than V_{RT}, the ray theory velocity. The slower velocities correspond to the effective medium theory velocity given by

$$\frac{1}{V_{EMT}^2} = \rho_{EMT} \sum_i \frac{f_i}{V_i^2} \tag{3.5}$$

where $\rho_{EMT} = \sum_i f_i \rho_i$, and ρ_i are the densities of each patch. This equation is equivalent to Hill's equation (Equation (3.3)) for a layered geometry. The second and larger transition is due to the transition from patchy unrelaxed to relaxed uniform saturation. This transition occurs when $d \approx L_c$, or when the patch size becomes so small that it is effectively uniform saturation. More precisely, this transition occurs when $\lambda > \frac{Vd^2}{D}$, where V is the velocity and D is the diffusivity.

Figure 3.6 shows the variation in seismic reflectivity, computed from the reflected amplitudes of the synthetic seismograms, with λ/d. These reflectivities are computed for a particular choice of the overburden properties. The overburden has a velocity of 3000 m/s and density of 3000 kg/m^3. Here we observe the well-known Bragg scattering effect, which occurs when the layer thickness is a multiple of one-half of the wavelength and shows a large increase in the reflected amplitude. The reflectivity at $\lambda/d < 1$ is given by the impedance contrast between the overburden and the first layer. As we move to finer scales of saturation (increasing λ/d), there is little change in reflectivity as long as $\lambda < d$. For the long wavelength unrelaxed limit, the reflectivity computed from the picked seismic reflection amplitude value matches the theoretical reflectivity computed from the effective medium velocity (Equation (3.5)). Therefore, at long wavelengths, the patchy unrelaxed medium can be replaced by an effective homogeneous medium. The second transition in the reflectivity is due to the transition from unrelaxed effective medium to the relaxed state. The reflectivity values of course depend on the choice of the overburden.

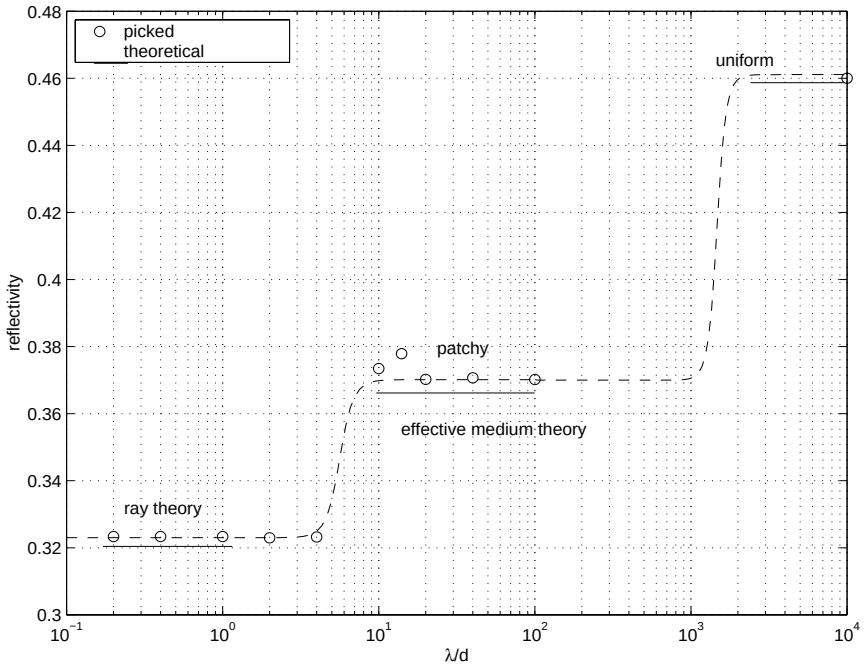

Figure 3.6: Seismic reflectivity versus λ/d. Horizontal lines show theoretical values.

AVO RESPONSE OF UNIFORM AND PATCHY SATURATION

When the wavelength is much larger than the patch size, the patchy saturation can be modeled as a homogeneous effective medium, with the velocities given by V_{EMT}. For a rock with a homogeneous mineralogy where the laminations are due only to fluids, the shear modulus is constant throughout the rock since fluids do not affect the shear modulus of a rock. As a result, the rock turns out to be isotropic, i.e., the P-wave and S-wave velocities in the rock are independent of the direction of propagation. We therefore say that for a rock with a homogeneous mineralogy, where fluid-induced heterogeneities are small compared to the seismic resolution, we can replace the heterogeneous rock with an "effective" homogeneous rock for reflection properties as well.

Figure 3.7 shows the AVO curves for the patchy unrelaxed and relaxed cases,

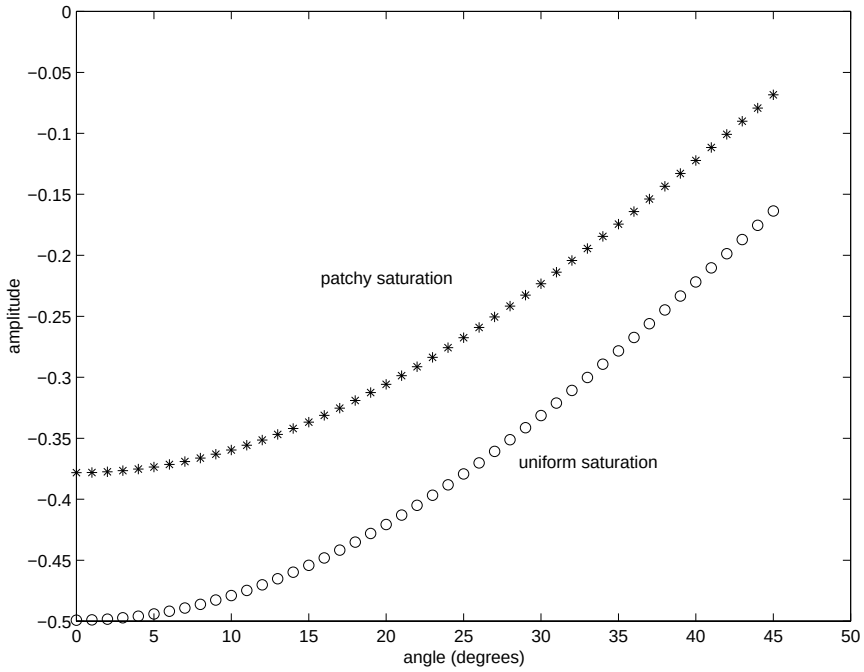

Figure 3.7: Amplitude variation with offset for (a) patchy unrelaxed model, and (b) patchy relaxed model, with 80% water-saturation.

at 80% water-saturation. We computed the AVO response for the patchy unrelaxed and relaxed models for different saturations, using Aki-Richards' approximations (Aki and Richards, 1980). Figure 3.8 (a) shows the AVO curves for the patchy unrelaxed case, for saturations ranging from 0 to 100%. Figure 3.8 (b) shows similar curves for the patchy relaxed case. As expected, we see that the AVO curves coincide in the completely dry and the completely saturated cases, but are well-separated and have distinct trends for partial saturations.

CONCLUSION

We investigated the seismic velocity and reflection properties of heterogeneous pore fluid saturations at different scales. Plane-wave, normal-incidence synthetic seismograms were

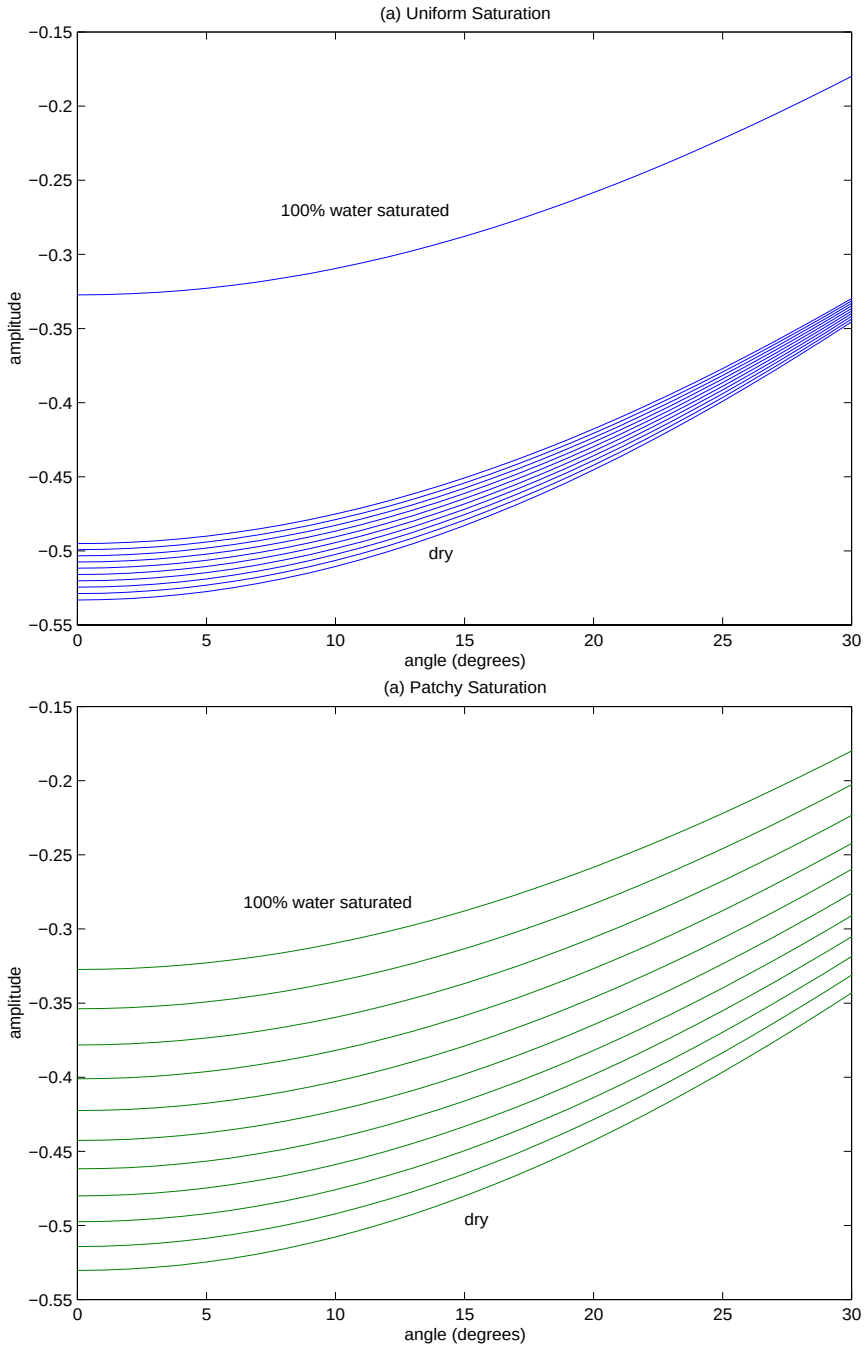

Figure 3.8: Amplitude variation with offset for (a) patchy unrelaxed model, and (b) patchy relaxed model, with saturations ranging from 0 to 100%.

computed using the Kennett algorithm for a range of saturation scenarios in a one-dimensional layered medium. Three principal scales of heterogeneities result from saturation distributions. In the first case, the fluid patches are much larger than the seismic wavelength, and they can be resolved seismically. In this short wavelength limit the velocity and reflectivity can be obtained from ray theory calculations. In the second case, the patches are smaller than the seismic wavelength, but they are not small enough to have sufficient time during a seismic period to diffuse and equilibrate the pore pressures. This is the effective medium unrelaxed limit. We show, using traveltimes and amplitudes from computed synthetic seismograms, that the patchy unrelaxed heterogeneous medium can be replaced by an "effective" homogeneous medium with P-wave modulus given by the Hill equation (Equation (3.3)). In the third situation of the effective medium relaxed limit, the patches are extremely small. The patches are well below seismic resolution and are also small enough to allow equilibriation of pore pressures within a seismic period. Here, we can replace the heterogeneous fluid distribution with a single "effective fluid", which is a Reuss average of the different phases (Equation (3.2)). This effective fluid is then used to saturate the dry rock using Gassmann's equation. Replacement by an "effective medium", means replacement in terms of both the transmission and the reflection properties. In Chapter 3.2, we discuss a strategy to constrain seismic velocities using knowledge of saturation scales from fine-scale flow simulations.

3.2 Impact of Flow-simulation Parameters on Saturation Scales

ABSTRACT

Sub-resolution scales of fluid saturation introduce uncertainties in the interpretation of seismic velocity. A “coarse-scale” or “patchy” distribution always has a higher seismic velocity than a “fine-scale” or “uniform” distribution. We present a multidisciplinary study which links rock physics and seismic with reservoir engineering to reduce uncertainties in saturation scales. In our study, we performed fine-scale flow-simulations which helped us to understand which reservoir parameters control the sub-seismic-resolution fluid distribution. Our studies show that when gas in injected into oil reservoirs, gravitational forces induce the formation of sub-resolution gas caps, which lead to patchy saturation at seismic scales. We also learned that that uniform saturation occurs for most waterfloods and for primary production scenarios where gas comes out of solution. Fluid density contrasts, mobility ratios, and residual oil saturations are some parameters that are crucial in constraining saturation scales.

INTRODUCTION

The sensitivity of seismic velocities to pore-fluids has been recognized for years (Gassmann, 1951, Biot, 1956, Nur and Simmons, 1969). More recently, several authors have pointed out that seismic velocities depend not only on the types and saturations of the pore fluids (water, oil, gas) but also on the spatial scales over which the fluid phases are mixed in the pore space (White, 1975, Dutta and Odé, 1979, Mavko and Mukerji, 1998). Spatially varying saturations give rise to wave-induced pore pressure gradients, which in turn cause wave attenuation and velocity dispersion (Akbar et al., 1994, Knight et al., 1995). Variation in saturation *scales* can introduce uncertainties into interpretation of seismic attributes for hydrocarbon detection.

Figure 3.9 shows an example of the non-unique dependence of seismic velocity on

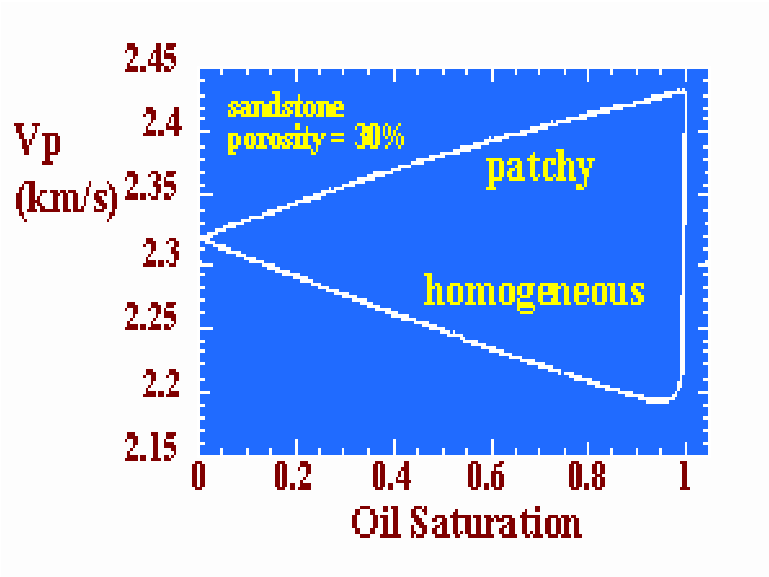

Figure 3.9: Velocity depends on fluid saturation, as well as on the saturation scales.

fluid saturation for a gas-oil mix. A more complete discussion of the basic scale effects can be found, for example, in Mavko and Mukerji (1998). The lower, non-linear curve is the "homogeneous" or "uniform saturation" model and corresponds to very fine-scale mixing of the pore-fluid phases. The upper, more linear curve is known as the "patchy saturation model" and corresponds to more coarse saturation scales. Uniform saturation refers to the case in which the saturation scales are small enough so that any wave-induced increments of pore pressure can diffuse among the fluid phases during a seismic period. Patchy saturation refers to the case where the saturation scale is large enough that the wave-induced pore pressure changes cannot equilibrate during a seismic period. If, for example, we observe a seismic velocity of $2.35km/s$, the oil saturation could be 0.99 with a fine-scale or uniform distribution or 0.20 with a coarse-scale, patchy distribution, or anywhere in between. Hence, without independent information about saturation scales, there may be a large uncertainty in interpreting the oil saturation from seismic.

In this chapter, we explore how various fluid flow parameters, such as wettability, permeability, fluid density, viscosity and relative permeability affect the saturation scale and the resulting seismic velocity. Our goal is to constrain the rock physics fluid-substitution

model with the aid of reservoir engineering knowledge and direct application of reservoir flow simulators.

Fine-Scale Saturation

When the scale of the saturation heterogeneity in the reservoir is significantly smaller than the seismic wavelength, the individual fluid patches cannot be seismically resolved, but they still influence seismic velocity and impedance. Sub-resolution patches may be divided into two ranges dictated by L_c, the critical diffusion (or relaxation) scale of the medium (Mavko and Mukerji, 1998). At a seismic frequency f, wave-induced pore pressure heterogeneities caused by spatially varying saturations will have time to relax and reach a local isostress state over scales smaller than the critical diffusion scale L_c.

$$L_c = \sqrt{\frac{D}{f}} \tag{3.6}$$

In Equation (3.6), $D = kK_{fl}/\eta$ is the hydraulic diffusivity, k is the permeability, K_{fl} is the fluid bulk modulus and η is the fluid viscosity. Mixtures of water, oil, and gas in regions of rock smaller that L_c can be replaced by an "effective fluid" (Domenico, 1976), having a bulk modulus given by the isostress Reuss average of the water-oil-gas moduli: $\frac{1}{K_{fl}} = \frac{S_w}{K_w} + \frac{S_o}{K_o} + \frac{S_g}{K_g}$, where S is the saturation, K is the bulk modulus, and μ is the shear modulus. The subscripts w, o, and g stand for water, oil, and gas. The saturated rock bulk modulus K_{sat} and shear modulus μ_{sat} can then be computed from the dry moduli K_{dry} and μ_{dry} using this average K_{fl} in Gassmann's relations:

$$\begin{aligned} \frac{K_{sat}}{K_{min} - K_{sat}} &= \frac{K_{dry}}{K_{min} - K_{dry}} + \frac{K_{fl}}{\phi(K_{min} - K_{fl})} \\ \mu_{sat} &= \mu_{dry} \end{aligned} \tag{3.7}$$

where K_{min} is the mineral bulk modulus. We refer to this fluid-substitution recipe using an effective fluid in Gassmann's equations as the "uniform saturation", or the "Gassmann-Domenico" model. The uniform saturation model is, in fact, a lower bound on the seismic

velocity as a function of saturation (Mavko and Mukerji, 1998).

Coarse-Scale Saturation

Spatial fluctuations of wave-induced pore pressure corresponding to heterogeneities of saturation on scales larger than L_c will tend to persist during a seismic period and will not be described well by the effective fluid model. This case is known as patchy saturation, and over these large scales, it is no longer valid to replace the water-oil-gas mixture with a Reuss average fluid. Instead, when each of the phases is well separated over scales $> L_c$, the effective moduli of the rock can be estimated with the equation from Hill (1963).

$$\frac{1}{K+\frac{4}{3}\mu} = \frac{S_w}{K_{wsat}+\frac{4}{3}\mu} + \frac{S_o}{K_{osat}+\frac{4}{3}\mu} + \frac{S_g}{K_{gsat}+\frac{4}{3}\mu} \tag{3.8}$$

where K and μ are the average effective bulk and shear moduli of the rock that the wave "sees". K_{wsat}, K_{osat}, and K_{gsat} are the bulk moduli of the rock fully saturated with water, oil, and gas, respectively, and are computed by putting the water, oil, and gas moduli separately into Gassmann's equations. The Hill equation is an exact result when there are no spatial variations in the shear modulus. This model is appropriate when the rock is homogeneous, the saturation scales are larger than L_c, and spatial heterogeneities are due to fluids (since fluids have no effect on the shear modulus at seismic frequencies). This is the patchy saturation model, which is an upper bound on the seismic velocity as a function of saturation (Mavko and Mukerji, 1998).

Knight et al. (1995) studied the velocity dependence on saturation scale by linking reservoir heterogeneity to saturation heterogeneity in a reservoir, which assumes a state of capillary equilibrium. According to their assumption, regions (or patches) in the reservoir, of different lithologies will have different levels of saturation, as determined from their capillary pressure curves. They accounted for spatial variation in shear modulus, because of the direct link between lithology-variation and saturation-heterogeneity. In our approach, we do not assume a direct link between lithology-variation and saturation-heterogeneity. Since, at the field scales, capillary forces are very small compared to viscous and gravitational forces, we neglected the capillary forces in our study.

At the reservoir scale, capillary forces are several orders of magnitude smaller than viscous and gravitational forces. The viscous pressure drop over a length L is given by $\eta q L/k$, where η is the coefficient of viscosity, q is the flow rate, and k is the permeability. The capillary pressure is given by $2\gamma/r$, where γ is the coefficient of surface tension and r is the representative pore-throat radius. Therefore, the ratio of viscous to capillary forces is given by $N_c Lr/k$ where N_c is the capillary number, defined as:

$$N_c = \frac{\eta q}{r} \tag{3.9}$$

The typical values of the parameters discussed above are given in Table 3.1 (Lake, 1989). The ratio of viscous to capillary forces is on the order of 10^4. Similarly, we can compute the ratio of gravitational to capillary forces. The gravitational pressure is given by $\Delta\rho g L$, where $\Delta\rho$ is the fluid-density contrast and g is the gravitational constant. The ratio of gravity to capillary forces is given by $\Delta\rho g Lr/2\gamma$, which, for the numbers in Table 3.1, is on the order of 10^3. We therefore consider that, at the field scale, capillary forces are negligible.

Table 3.1: Comparing viscous, gravitational and capillary forces at the reservoir scale

Parameter	Symbol	Typical value
Coefficient of viscosity	η	$10^{-3} kg/m/s$
Flow rate	q	$10^{-5} m/s$
Coefficient of surface tension	γ	$5\text{x}10^{-2} N/m$
Length	L	$1000m$
Pore-throat radius	r	$5\text{x}10^{-5} m$
Permeability	k	$10^{-12} m^2$ (1 Darcy)
Capillary number	N_c	$10^{-5} - 10^{-7}$
Density contrast	$\Delta\rho$	$200 kg/m^3$
Gravitational constant	g	$10 m/s^2$
Viscous to capillary force ratio	$F_{v/c}$	$\approx 10^4$
Gravity to capillary force ratio	$F_{g/c}$	$\approx 10^3$

METHOD

For the present analysis we use a combination of the two approaches to model both the fine-scale and the coarse-scale saturations appropriately. We first use the uniform saturation model (Gassmann-Domenico equations) locally, to properly account for saturation variations $< L_c$, and then use the Hill equation to upscale the fine scale velocities to seismic scales. The steps in this approach are illustrated in Figure 3.10, and the steps are summarized below.

Figure 3.10 (a) shows a "typical" coarsely-gridded reservoir model that might be used by petroleum engineers in field scale flow simulations. The grid dimension is often $10m$ or larger. The simulator reports a single saturation value for the entire $10m$ x $10m$ block. Most often, we do not know the fluid distribution within this $10m$ x $10m$ block, and hence we have a problem deciding whether to use the effective fluid (uniform saturation) model or the Hill average (patchy saturation) model to predict velocities corresponding to the saturations (Step 2 (d)).

To explore this problem, our approach was to use a reservoir model much more finely gridded as our input to the flow simulator. The grid dimension was set equal to the critical diffusion length L_c, which for seismic frequency of about $50Hz$ and permeability of about $100mD$ is about $1m$. This length, L_c, is the finest scale we need to worry about, since any saturation heterogeneities smaller than this critical relaxation scale can be modeled using the isostress Reuss average fluid.

We performed the fine scale flow simulations using Eclipse, which is a fully implicit, three-phase, three-dimensional, general purpose black oil simulator. First, we obtained finely gridded saturation maps (at scale L_c), as shown in Figure 3.10 (b), as outputs of our flow simulations. Using the Gassmann-Domenico fluid substitution equations locally, we then calculated the seismic velocities within each tiny L_c x L_c simulator cell, as shown in Figure 3.10 (c). We assumed that the dry rock has the same velocity everywhere (at each cell), so that any heterogeneities in the velocity are caused by saturation changes only. Next, we upscaled the finely gridded velocities obtained in step (c) to the seismic resolution scale, which is about $50m$ x $20m$, as shown in Figure 3.10 (d), by applying the Hill average. Each seismic scale grid is now assigned a mean fluid saturation which is

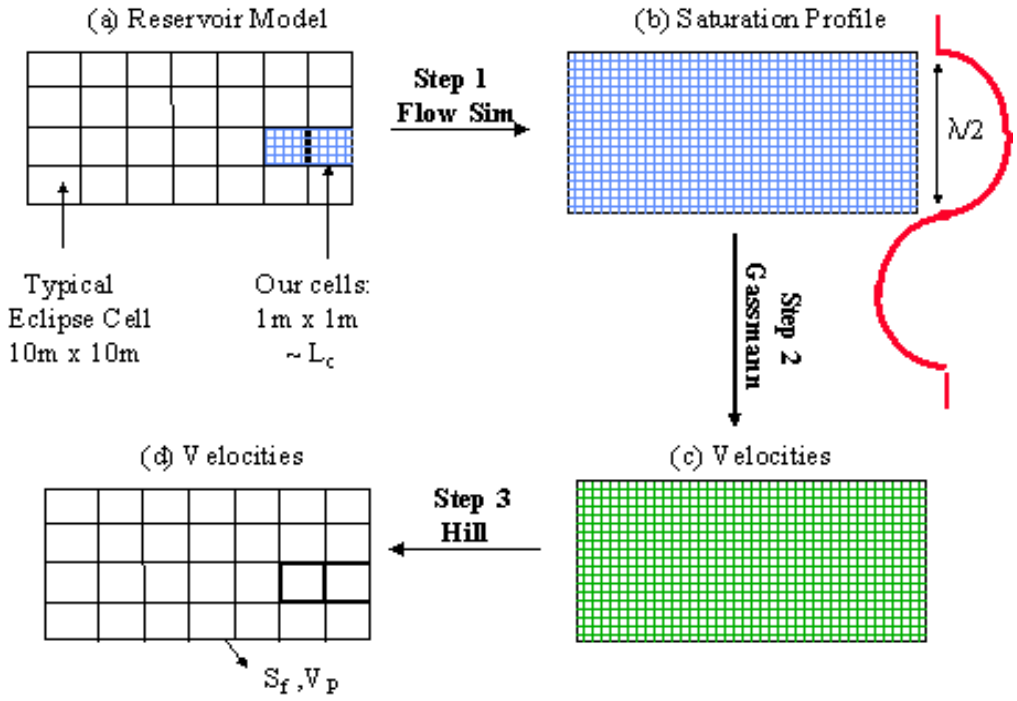

Figure 3.10: Schematic diagram of the approach used in this study to solve the problem of determining saturation scales.

simply a volumetric average of the fine-scale saturations, and a seismic velocity which is the Hill average of the finely gridded velocities, as illustrated in Figure 3.10 (d). We call this approach a Gassmann-Domenico-Hill fluid-substitution.

If, in certain scenarios, going through all the steps (a)-(b)-(c)-(d) gives the same results as going directly from (a) to (d), we can conclude that in those scenarios there are no significant variations in saturations larger tham L_c but smaller than the seismic resolution, and we need not worry about patchy saturation. However, if the results turn out to be different, then we need to consider using the patchy model, or some average of the two models.

In the next sections, we explore a few different production scenarios using the detailed Gassmann-Domenico-Hill approach to determine the cases when the uniform saturation model is a good approximation and when we should use the patchy saturation model.

EXAMPLES

We studied both primary production scenarios, i.e., gas coming out of solution when an oil-reservoir is produced, and secondary production scenarios, e.g., waterflooding and gas injection. For both kinds of scenarios, we tried to identify the reservoir and fluid parameters that were important in determining the scales of saturations. The reservoir parameters we studied are the relative permeability of the fluid phases in the reservoir, the wettability, the mobility ratios of the fluids, gravity effects, and the fine-scale permeability distributions in the reservoir. We did not study capillary pressure effects (Knight et al., 1995), since at the field scale, viscous and gravitational forces have much larger effects than capillary forces (Table 3.1). Table 3.2 shows the typical fluid properties that were used in the flow simulations.

Table 3.2: Fluid Properties.

Fluid Property	Water	Oil	Gas
Density (kg/m^3)	1000	800	9
Bulk Modulus (GPa)	2.25	1.00	10^{-4}
Viscosity (cp)	1.00	1.00	0.001

In the Eclipse flow simulations, we used two-dimensional permeability models as inputs, which we generated using simple stochastic simulations. We used a few different kinds of permeability models such as homogeneous models, simple layered models, log-normally distributed permeability model, and bimodal log-normal permeability models. Some of the permeability models, and the corresponding histograms of the permeability distribution are shown in Figure 3.11.

WATERFLOOD

We studied the saturation patterns obtained by waterflooding a water-wet reservoir, which was initially saturated with oil. Water was injected from the right, and oil was produced from the left. The saturation patterns obtained from the flow simulator were mapped onto

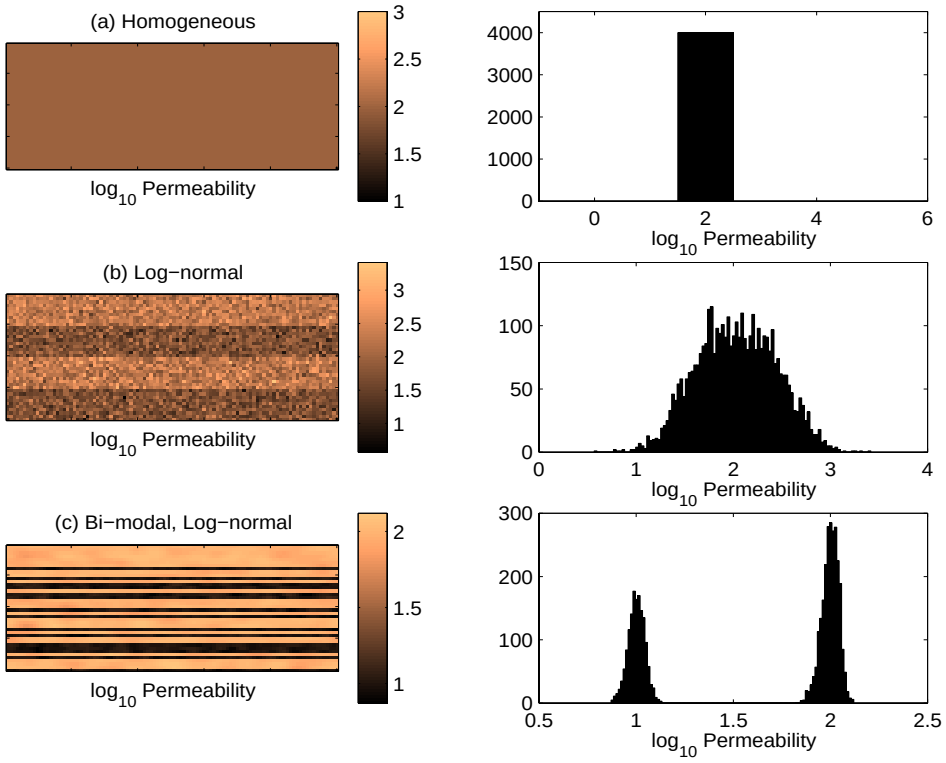

Figure 3.11: Some permeability models, and the corresponding histograms used in the flow-simulations. The unit of permeability is milli Darcy.

seismic velocities by using Gassmann's equation locally to calculate the velocity at each small flow-simulator cell and then by using Hill's equation to upscale the velocity, as outlined in the previous section.

Relative Permeability

An important parameter that affects the saturation scales is the relative permeability (k_r) of the fluids in the reservoir. The solid and dashed lines in Figure 3.12 show two different sets of k_r 's of oil and water in the reservoir. The dashed lines are simple, somewhat unrealistic, approximations to the relative permeabilities, which are sometimes used when accurate lab measurements of relative permeabilities are not available. The straight lines can give fairly reasonable results for engineering purposes even though they are simplified. The solid

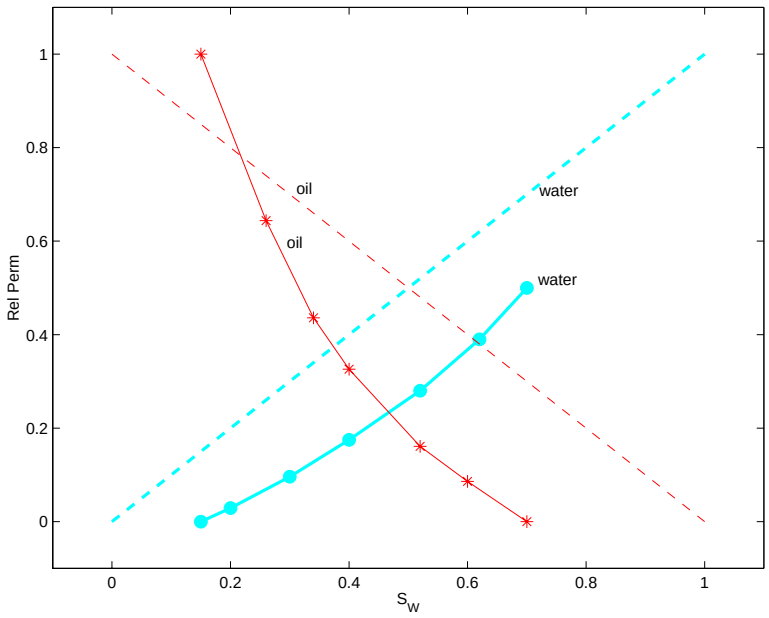

Figure 3.12: Two examples of relative permeability curves used in flow simulations.

non-linear lines are nearer to commonly measured k_r curves. For our purpose, the most important difference between these two sets of curves is that the dashed k_r curves indicate zero residual oil (or irreducible oil) and zero connate water, while the solid curves indicate finite amounts of residual oil and connate water. The relative permeability of a phase is typically a function of saturation of that phase in the rock. These relations are inputs to the flow simulator. Relative permeabilities are usually measured on cores in the laboratory.

Figure 3.13 (a) shows a vertical cross-section of the saturation distribution in the reservoir, obtained by using the solid k_r curves, from Figure 3.12 with a residual oil saturation (S_{OR}) of 0.3. Figure 3.13 (b) shows the saturation profile obtained using k_r curves very similar to the solid k_r curves, but with an S_{OR} of 0.2. Figure 3.13 (c) shows the saturation profiles obtained using the dashed k_r curves from Figure 3.12, with S_{OR} of zero.

We observe in Figure 3.13 (a) that the maximum water saturation never goes above 0.7. This is because the residual oil saturation is 0.3, which is the minimum amount of oil that can be left behind in any of the cells. In Figure 3.13 (c) however, we find pixels of 100% water, since there is no residual oil and complete production is possible. The corresponding

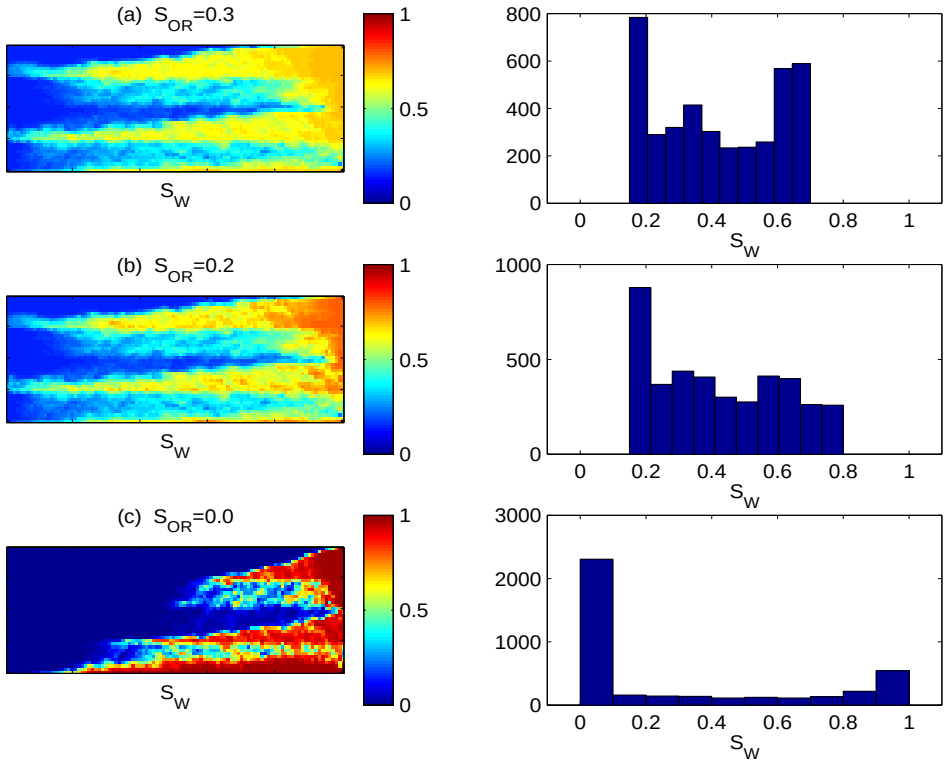

Figure 3.13: Waterflood: Water-saturation profiles and corresponding histograms obtained using three different sets of relative permeability curves, each with a different amount of residual oil (S_{OR}).

seismic velocities are computed using Gassmann followed by the Hill average, and plotted in Figure 3.14.

Figure 3.14 shows that knowledge of flow simulation results can reduce the uncertainty in interpreting the seismic signatures of fluid saturations. The triangles correspond to the flow simulators using dashed relative permeability curves in Figure 3.12, which indicate that there is no residual oil in the reservoir. We can see that these points fall throughout the region between the patchy and uniform bounds. It is useful to recall that the bounds describe the envelope of all possible fluid distributions lying between the saturation extremes of 100 % oil and 100 % water.

Flow simulations made with more realistic relative permeabilities, for example the solid

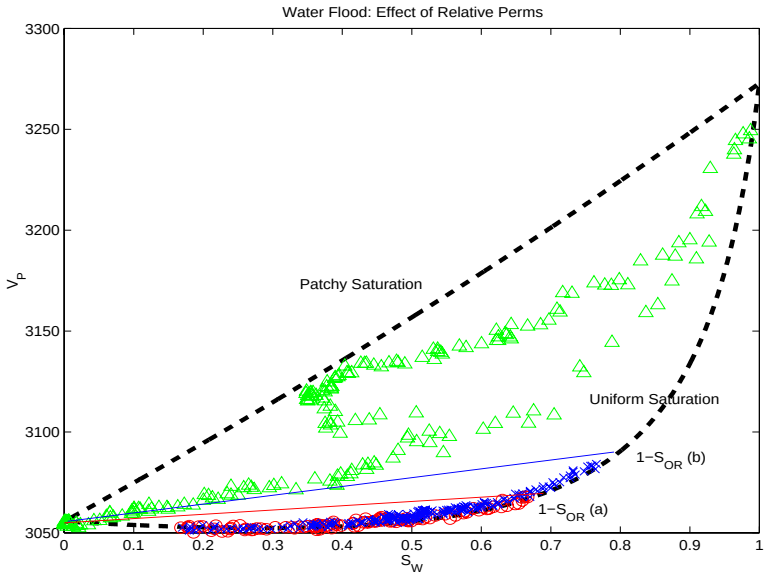

Figure 3.14: Waterflood: Velocity (m/s) versus water-saturation for the saturation profiles in Figure 3.13. The circles correspond to saturation profile (a), crosses correspond to (b), and triangles correspond to (c).

lines shown in Figure 3.12, yield the values represented by the circles in Figure 3.14, corresponding to the saturation profile in Figure 3.13 (a). In this case, the residual oil saturation is 0.7. All the circles n Figure 3.14 fall between narrower bounds, called the modified patchy bounds, and represent the much narrower envelope of possible fluid distributions between saturation limits of 100 % oil and 70 % water.

This new and narrower bound can be computed using the following steps. First, we compute the moduli, or velocities, corresponding to the residual oil and the residual (or connate) water points. We call these moduli K_{or} and K_{wc}, and the corresponding velocities V_{or} and V_{wc}, and compute them using Gassmann's equations:

$$\frac{K_{wc}}{K_{min} - K_{wc}} = \frac{K_{dry}}{K_{min} - K_{dry}} + \frac{K_{f1}}{\phi(K_{min} - K_{f1})} \tag{3.10}$$

where $\frac{1}{K_{f1}} = \frac{S_{wc}}{K_w} + \frac{1-S_{wc}}{K_{oil}}$, which gives the bulk modulus of the fine-scale mixture of water and oil at the connate water saturation. Similarly, we can compute the moduli at the residual

oil saturation:

$$\frac{K_{or}}{K_{min} - K_{or}} = \frac{K_{dry}}{K_{min} - K_{dry}} + \frac{K_{f2}}{\phi(K_{min} - K_{f2})} \tag{3.11}$$

where $\frac{1}{K_{f2}} = \frac{1-S_{or}}{K_w} + \frac{S_{or}}{K_{oil}}$, which gives the bulk modulus of the fine-scale mixture of water and oil at the residual oil point. Since Gassmann's equations predict no change in shear modulus with change in the fluid, $\mu = \mu_{dry}$ for all values of saturation. We now use Hill's equation to calculate the modified patchy upper bound for saturations between S_{wc} and $1 - S_{or}$, at the intermediate saturation values. Thus for any water saturation S_w, the modified patchy modulus is given by

$$\frac{1}{K_{MP} + \frac{4}{3}\mu} = \frac{S_{f1}}{K_{wc} + \frac{4}{3}\mu} + \frac{S_{f2}}{K_{or} + \frac{4}{3}\mu} \tag{3.12}$$

where $S_{f1} = S_w + S_{or} - 1/S_{wc} + S_{or} - 1$, and $S_{f2} = 1 - S_{f1}$. K denotes bulk modulus, μ denotes shear modulus, ϕ denotes porosity, and S denotes saturation. The subscript "min" refers to the grain, "wc" refers to connate water, and "or" refers to residual oil. We also define the fluids $f1$ and $f2$, where $f1$ corresponds to a mixture of water and oil, where the volume fraction of water is the amount of connate water saturation, and the rest is oil. Similarly, $f2$ is also a mixture of water and oil which has a volume fraction of oil equal to the residual oil saturation, and the rest is water.

All the P-wave velocities corresponding to the calculated moduli, can, of course, be computed using the equation $V = \sqrt{\frac{K+\frac{4}{3}\mu}{\rho}}$, where ρ is the rock bulk density.

Another example of velocities is obtained by using a residual oil saturation of 0.8. These velocities are plotted as crosses in Figure 3.14. Again, these crosses fall within the bounds defined by the uniform saturation curve and the modified patchy curve. In Figure 3.14, the modified upper bound corresponding to a residual oil of 0.8 is indicated by the blue line, while the modified upper bound corresponding to a residual oil of 0.7 is indicated by the red line.

Wettability

Next, we examine the effect of wettability of the rock on the saturation scales. We repeat the same waterflooding with the same initial conditions, but now we consider the case

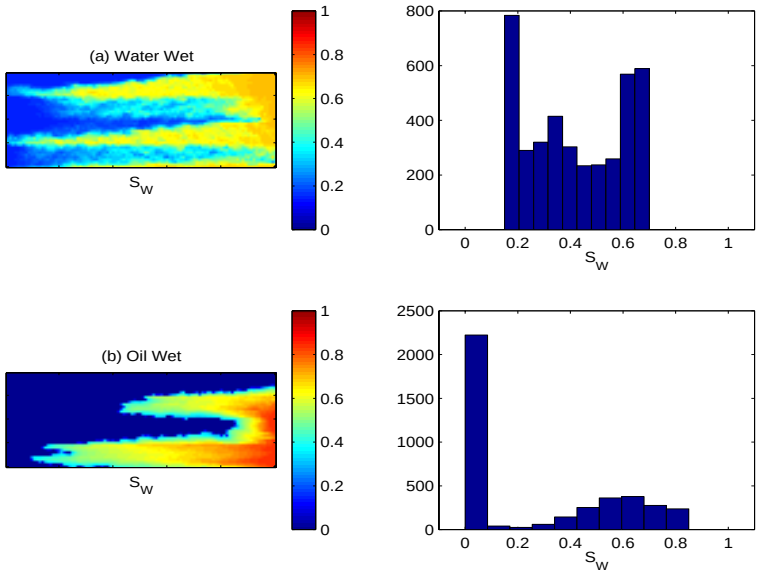

Figure 3.15: Waterflood: Water-saturation profiles and corresponding histograms for a water-wet and an oil-wet rock.

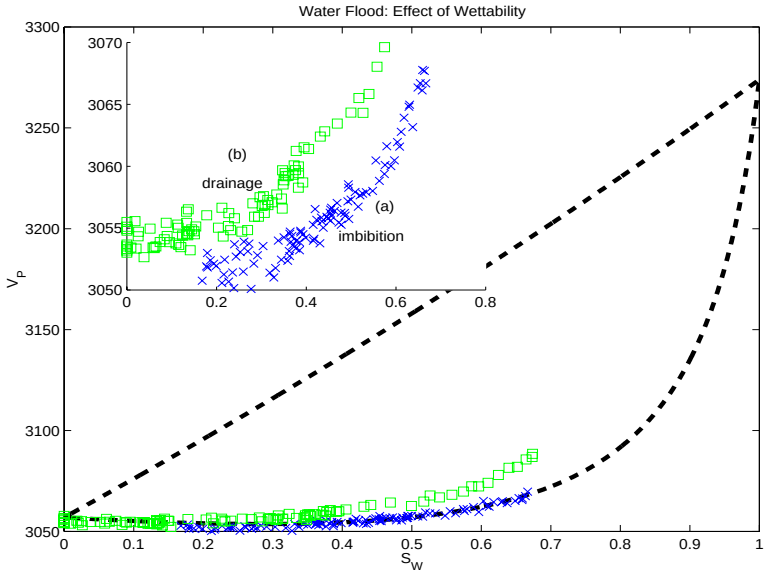

Figure 3.16: Waterflood: Velocity (m/s) versus water-saturation for the saturation profiles in Figure 3.15. Squares correspond to oil-wet rock, and crosses correspond to water-wet rock.

where the reservoir rock is oil-wet.

The wettability of the rock affects the relative permeability curves. Waterflooding an oil-wet rock is a "drainage" mechanism according to the convention of Petroleum Engineering literature, while waterflooding a water-wet rock is "imbibition". The result of waterflooding an oil-wet reservoir is shown in Figure 3.16.

From Figure 3.15, we observe that waterflooding an oil-wet rock, i.e., drainage, yields higher velocities (indicated by the squares) than velocities obtained by waterflooding a water-wet rock, i.e., imbibition (indicated by crosses). These results conform to experimental results obtained by both Knight et al. (1995) and Cadoret (1993), in which the saturation tended to be patchy during drainage, and uniform during imbibition. One main reason for a similar observation in our flow simulations is that the residual oil is typically lower in an oil-wet rock. Therefore, the modified patchy bound for the oil-wet rock is closer to the patchy bound. Typical residual oil saturations for water wet rocks are 30-40%, while for oil-wet rocks they may be as low as 10%. However, in oil-wet rocks, the low relative permeability of oil at high values of oil-saturation results in a drop in the production rate in the early stages of production. Therefore, waterflooding of oil-wet reservoirs is not economically worthwhile and is never performed in practice.

Mobility Ratios

The mobility ratio (MR) is a function of the relative permeabilities (k_r) and the viscosities (η) of the fluid phases in the reservoir.

$$MR = \frac{k_{rw}^{max}\eta_{oil}}{k_{ro}^{max}\eta_{w}} \tag{3.13}$$

We selected a very low residual oil saturation (0.02) in order to widen the separation of the bounds and exaggerate the sensitivity to the MR. We then studied the effect of the mobility ratio on the saturation scales. We changed the mobility ratio (MR) by changing the viscosity of oil in Equation 3.13. Figures 3.17 and 3.18 show the effect of mobility ratio on the saturation scales. The velocities for a low MR ($MR = 5$) fall towards the patchy curve, and those for a high MR ($MR = 50$) fall toward the uniform saturation curve. Increasing the mobility ratio gradually moves the seismic velocities from the patchy curve

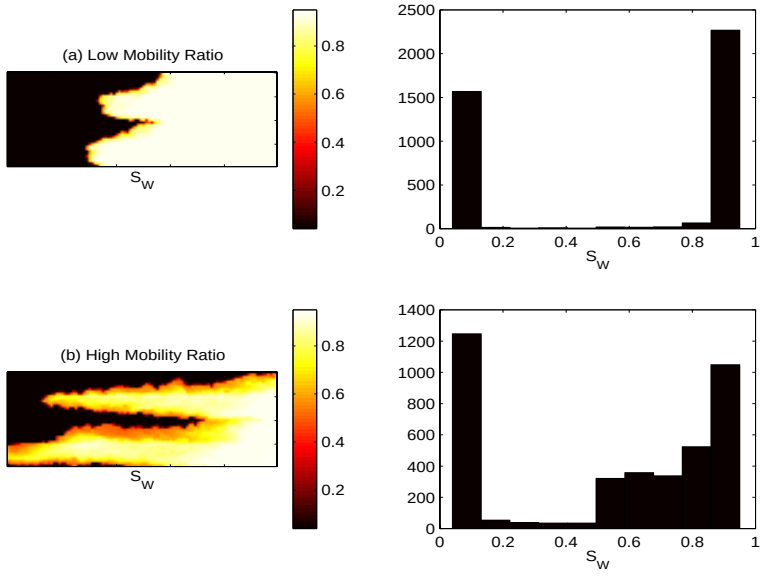

Figure 3.17: Waterflood: Water-saturation profiles and corresponding histograms for a low mobility ratio (MR=5), and a high mobility ratio (MR=50).

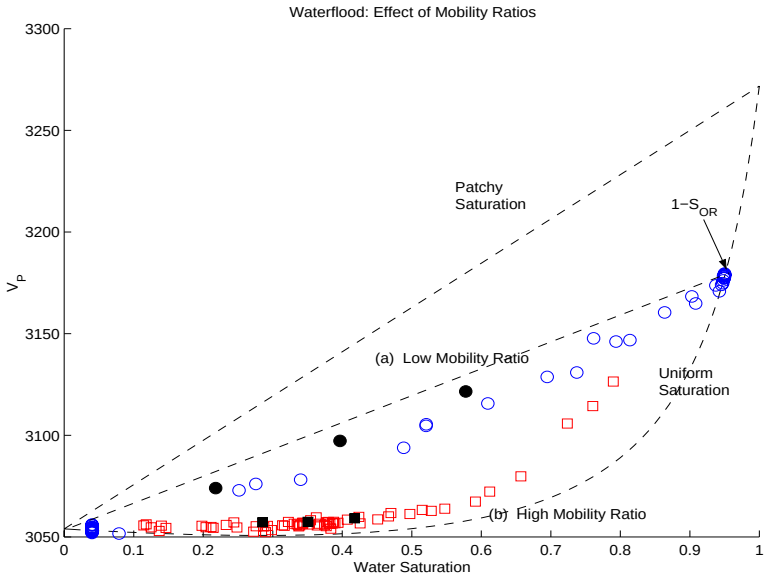

Figure 3.18: Waterflood: Velocity (m/s) versus water-saturation for the saturation profiles in Figure 3.17 Circles correspond to the low MR (a) and squares to the high MR (b).

towards the uniform saturation curve. However, this effect can be observed only for very low residual oil saturations. For higher residual oils, the bounds fall so close together, that the MR effect becomes invisible. We can conclude that mobility ratio is not very important unless the residual oil is less than 0.05.

Waterflood: Conclusions

From our studies of waterflooding an oil reservoir we conclude that for most cases, the uniform saturation model is a close enough approximation for residual oil saturation of greater than 0.05. For residual oils saturation of less than 0.05, the wettability and mobility ratios determine the saturation scales. If $S_{or} < 0.05$, we can expect patchy saturation in oil-wet rocks, or at high mobility ratios ($MR >\approx 50$).

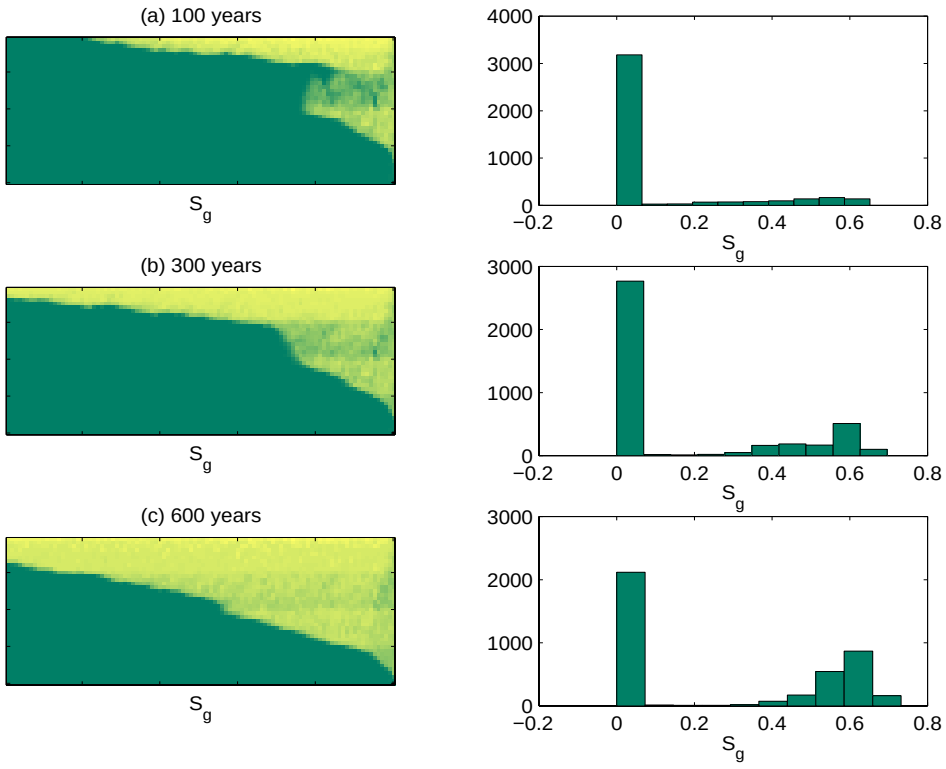

Figure 3.19: Gas injection: Gas-saturation profiles and corresponding histograms for three time-steps.

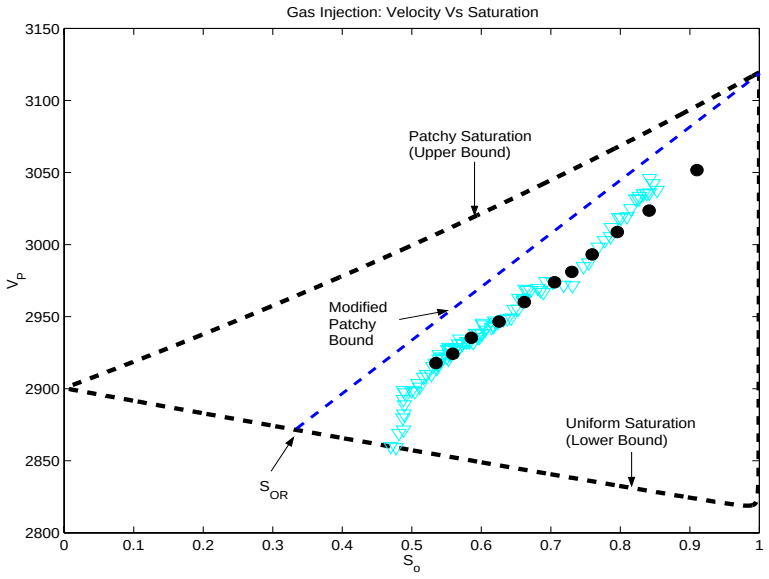

Figure 3.20: Gas injection: Velocity (m/s) versus gas-saturation for the saturation profiles in Figure 3.19. The triangles are vertical averages, while the filled circles are averages over the whole block, corresponding to various time-steps.

GAS INJECTION

In this section, we discuss a different secondary production scenario, i.e., gas injection. The reservoir is initially saturated with oil, as in the the previous section. Gas is injected into the reservoir from an injection well on the right, and oil is produced at the left.

Figure 3.19 shows the saturation patterns and histograms of the saturation maps obtained at different time-steps during gas injection. The large density contrast between the fluids plays a significant role in determining the saturation scales. Being much lighter than the oil, gas stays at the top of the reservoir, forming a gas cap. We see from the histograms in Figure 3.19 that there are large patches of pure oil and almost pure gas, which indicates seismically "patchy" behavior. In the case of gas injection, the injected fluid is the non-wetting phase, and this process is therefore a drainage mechanism.

Figure 3.20 shows the seismic velocities obtained from the saturation maps. The pixel velocities are computed using Gassmann's equations locally, and the velocities are upscaled using Hill's equation. The dry-rock velocities are, as before, assumed to be the same at all

pixels. The saturation range is spanned by computing the average saturations at different time-steps, as well as at different distances from the fluid front.

Relative Permeability

The residual oil saturation again narrows the bounds, and thus reduces the uncertainty in saturation scales. Figure 3.20 shows the lower uniform saturation bound, the upper patchy saturation bound, and the modified patchy bound for $S_{or} = 0.3$. The Hill average velocities computed from the saturation profiles in Figure 3.19 lie between the narrower bounds. The triangles correspond to vertical averages at various time-steps and at various distances from the front. The filled circles are spatial averages over a seismic pixel ($50m$ x $20m$) at various time-steps.

In case of gas injection, the bounds narrow down, but they do not collapse as in case of waterfloods, because the residual (or connate) saturation of gas, which is the softer of the two fluids, is always zero.

Wettability

Wettability is not a significant issue in the case of gas injection into oil, because gas is always the non-wetting phase. Gas injection is therefore always a drainage mechanism, since oil, which is the wetting fluid, is being drained out.

Mobility Ratios

The mobility ratio MR for gas injection is defined as

$$MR = \frac{k_{rg}^{max}\eta_{oil}}{k_{ro}^{max}\eta_{gas}} \tag{3.14}$$

where k_r are the relative permeabilities and η are the viscosities. We changed the mobility ratio by changing the oil viscosity. A high mobility ratio corresponds to very viscous oil.

We examine the effect of mobility ratio on seismic velocities versus saturation. Figures 3.21 (a) and (b) show the saturation profiles for different mobility ratios. In Figure 3.21 (a),

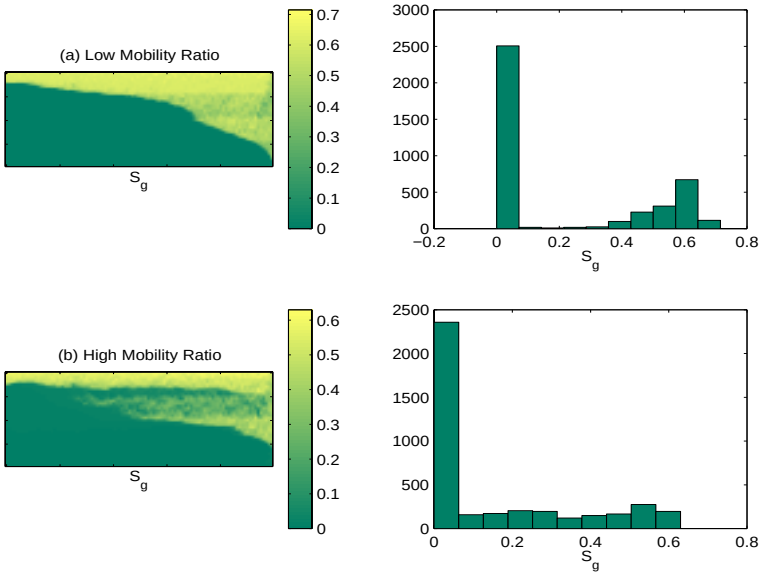

Figure 3.21: Gas injection: gas-saturation profiles and corresponding histograms for two different mobility ratios: (a) Low, MR=1, and (b) High, MR=500.

which corresponds to a mobility ratio $MR = 1$, we see that there is a distinct formation of a gas cap. The saturation histogram shows a clear separation between a patch of oil and a patch of gas. In Figure 3.22, the circles correspond to the velocities computed from the saturation profile in Figure 3.21 (a). These points show a linear behavior with saturation, and fall closer to the patchy saturation bound than the uniform saturation bound.

Figure 3.21 (b) shows the saturation profile for gas injection into a very viscous oil, i.e., when the mobility ratio is extremely high ($MR = 500$). From the saturation profile, as well as the histogram of the saturation, we observe that there are many intermediate saturations. The corresponding velocities are plotted in Figure 3.22 as squares and fall closer to the uniform saturation bound.

These figures show two extreme cases. Intermediate values of MR cause the velocity versus saturation points to fall between these two extreme cases. The MR has to increase or decrease by a factor of 50 to make an observable shift in the velocity versus saturation curve. We conclude that the sensitivity of the velocity to mobility ratio is very low.

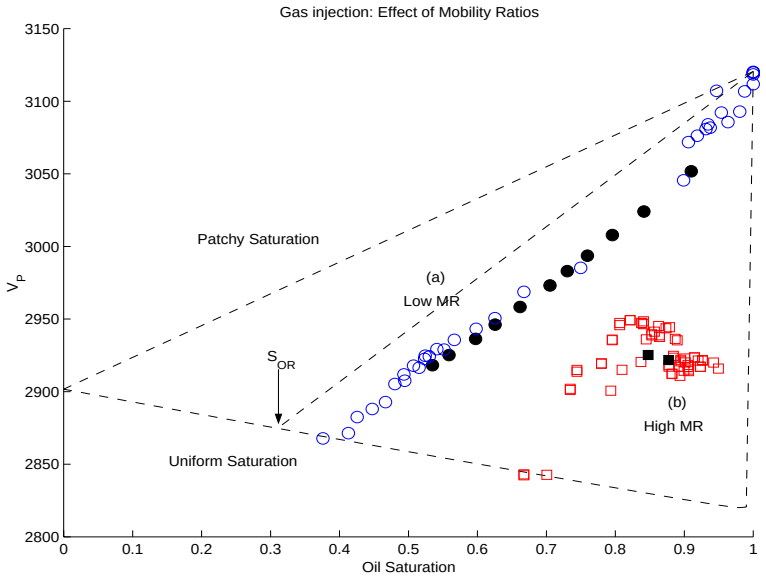

Figure 3.22: Gas injection: Velocity (m/s) versus gas-saturation for the saturation profiles in Figure 3.21. Circles correspond to the low mobility ratio (a), and the squares correspond to the high mobility ratio (b). Open symbols indicate vertical averages, and filled symbols indicate volumetric averages.

Gas Injection: Conclusions

We conclude that gas injection easily gives rise to patchy saturation, because gravitational forces cause the gas to form sub-resolution gas-caps above the oil in the reservoir. Uniform saturation was generated in a gas-injection scenario only under unrealistic conditions such as abnormally high mobility ratio and unusually high contrast in the permeability.

The patchy saturation model, modified by the residual oil saturation, gives a much better approximation than the uniform saturation model. We can calculate this new modified upper bound using the same steps and equations shown in the waterflood scenario, except that here, instead of water properties, we use gas properties. In addition, the value of residual gas is zero. Therefore, the modified patchy bound can be calculated for various values of the gas saturation S_g using the following equations:

$$\frac{K_{gs}}{K_{min} - K_{gs}} = \frac{K_{dry}}{K_{min} - K_{dry}} + \frac{K_{gas}}{\phi(K_{min} - K_{gas})} \tag{3.15}$$

$$\frac{K_{or}}{K_{min} - K_{or}} = \frac{K_{dry}}{K_{min} - K_{dry}} + \frac{K_{f2}}{\phi(K_{min} - K_{f2})} \tag{3.16}$$

where $\frac{1}{K_{f2}} = \frac{1-S_{or}}{K_{gas}} + \frac{S_{or}}{K_{oil}}$. K denotes bulk modulus, μ denotes shear modulus, ϕ denotes porosity, and S denotes saturation. The subscript "min" refers to the grain, "gs" refers to gas saturated, and "or" refers to residual oil.

We can calculate the modified patchy upper bound using the Hill average:

$$\frac{1}{K_{MP} + \frac{4}{3}\mu} = \frac{S_{f1}}{K_{gs} + \frac{4}{3}\mu} + \frac{S_{f2}}{K_{or} + \frac{4}{3}\mu} \tag{3.17}$$

where $S_{f1} = \frac{S_{gas}+S_{or}-1}{S_{or}-1}$, and $S_{f2} = 1 - S_{f1}$.

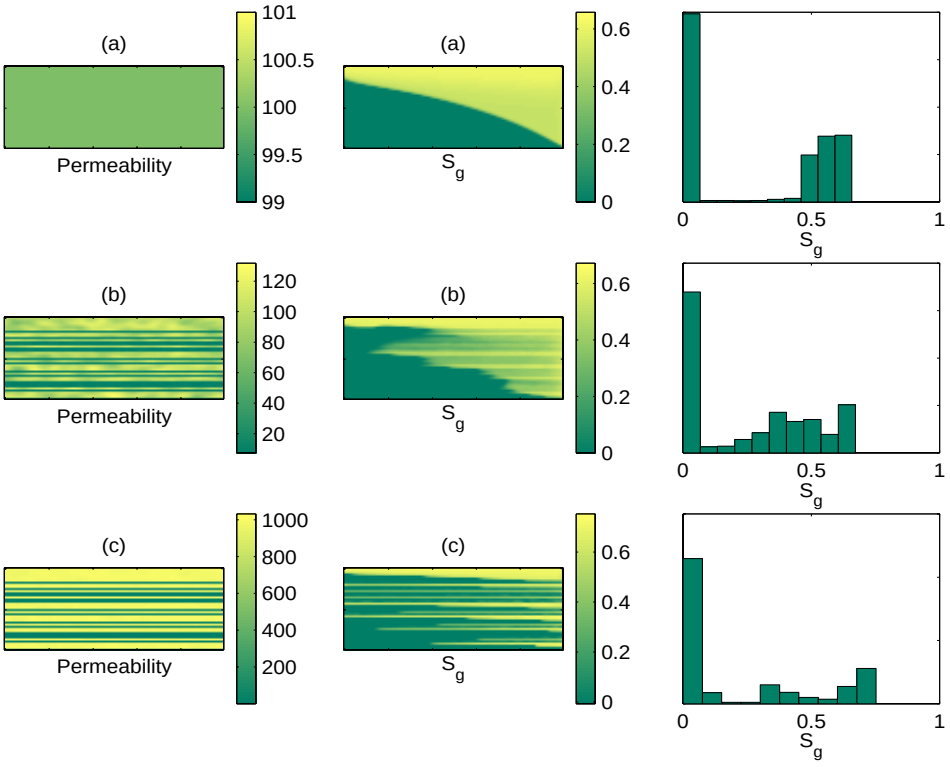

Figure 3.23: Gas injection: Water-saturation profiles and corresponding histograms for three different permeability models.

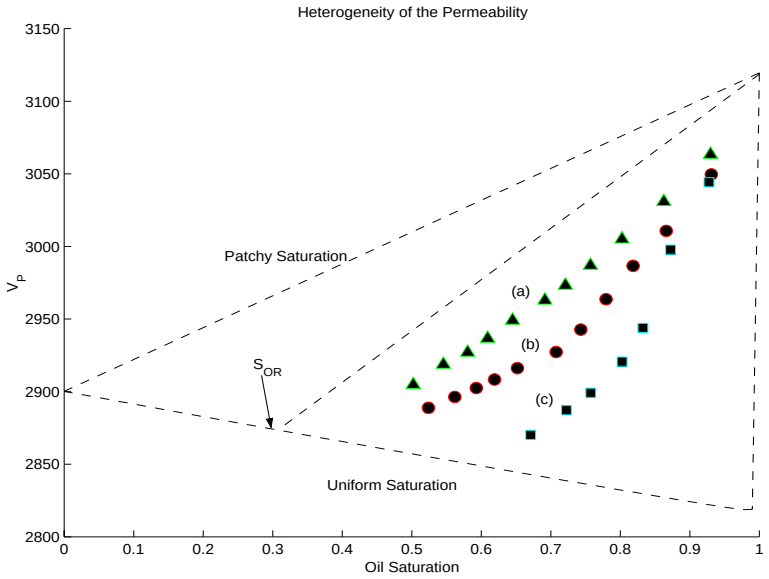

Figure 3.24: Gas injection: Velocity (m/s) versus gas-saturation for the saturation profiles in Figure 3.23. Triangles correspond to the models (a), circles correspond to (b), and squares correspond to (c) in Figure 3.23.

Fine-Scale Permeability Distribution

We investigated whether or not the fine-scale permeability distribution has an effect on the saturation scales. We used different permeability models to study its effect on saturation scales, and we show the results of these tests for gas injections.

Figure 3.23 shows three different permeability models with three different degrees of heterogeneity. The first model, (a), is a homogeneous permeability model with the average permeability of 100 mD. The second model, (b), is a layered sequence of high and low permeabilities, with a permeability ratio of about 100 between the high and low permeability regions. The third model, (c), has the same spatial structure as the second model, but the ratio of the high to the low permeability is 10,000. The corresponding gas-saturation profiles for exactly the same reservoir conditions are shown alongside each permeability model. The histograms represent the frequency distribution of the pixels of gas-saturation.

Seismic velocities computed for the three different saturation profiles are plotted in Figure 3.24. The velocity-saturation relationship obtained from the permeability model in

Figure 3.23 (a), which is denoted by the triangles in Figure 3.24, lies close to the patchy saturation curve. This indicates that when the when the scale of the heterogeneity of the permeability is much larger that the characteristic diffusion length, the resulting saturation scale is also large. The velocities corresponding to saturations obtained by flow-simulating the permeability models in Figure 3.23 (b) and (c), denoted by the circles and squares respectively, fall more towards the uniform saturation curve. This indicates that finer scales of permeability heterogeneity lead to finer scales of saturation. The squares in Figure 3.24 fall below the circles, indicating that a larger contrast in the permeability causes the saturation scale to be finer. However, the sensitivity of saturation scales to the permeability heterogeneity is quite low, compared to other parameters such as the residual fluid saturations and the fluid density contrasts.

GAS OUT OF SOLUTION

We studied the effect of saturation scales on seismic velocity in a primary production scenario when gas comes out of solution as a result of pressure drop in the reservoir. Figure 3.25 shows the flow simulator outputs of oil and gas saturation profiles. Three different permeability models were used. In Figures 3.25 (a), (b), and (c), the reservoirs were all initially saturated with a live oil i.e., an oil containing dissolved gas. Oil was pumped out from a vertical producer located in the center of the reservoir. Figure 3.25 (c) shows prominent coning effects where the well is located.

In all the saturation profiles of Figure 3.25 we observe that gas-caps form at the top of the higher permeability layers. However, there are small gas bubbles present in the oil that have not yet begun to move upwards. The presence of these gas bubbles may not be immediately obvious, but careful examination of the color scales, or of the histograms corresponding to the saturation profiles show non-zero values of S_g, which indicates the presence of gas bubbles. These gas bubbles are a fine-scale distribution of gas in the reservoir, and this distribution dominates the effect of the coarse-scale gas-caps. The velocity modeling, shown in Figure 3.26, shows that the velocity-saturation relationship follows the uniform saturation curve.

Since there are bubbles present at a fine scale in the reservoir, we are essentially mixing

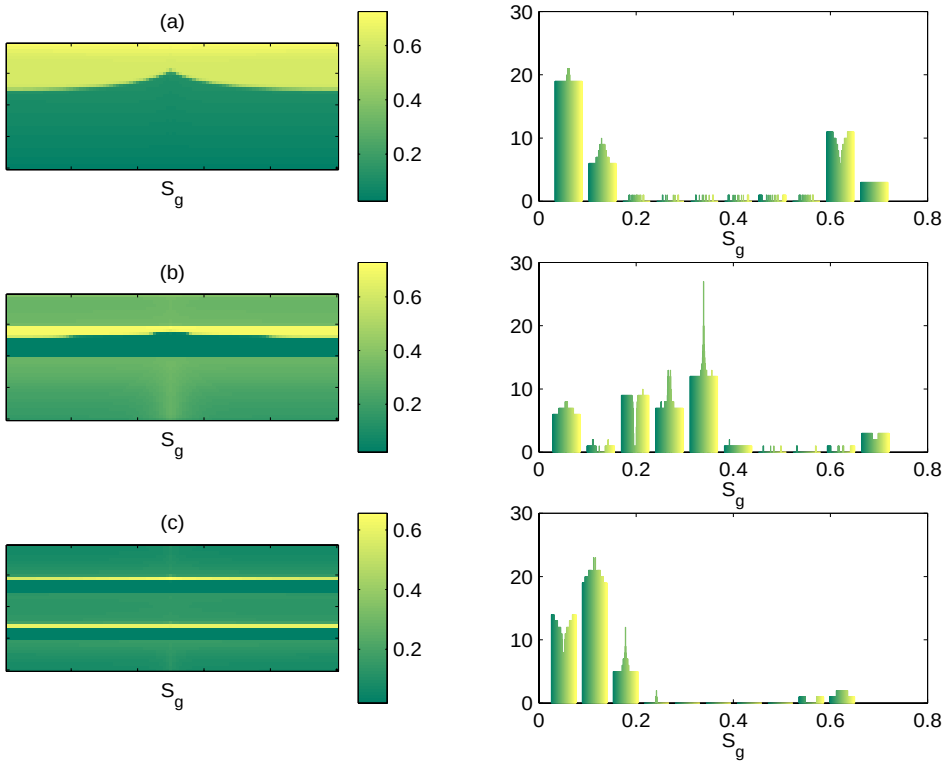

Figure 3.25: Gas out of solution: Gas-saturation profiles and corresponding histograms for three different permeability models.

the gas caps with a very “bubbly” (soft) oil which has a low velocity, in contrast to the gas injection scenario, which used a pure (stiff) oil. The velocities do not fall near the upper (patchy) bound, because the stiffer end member at the high oil saturation end of the curve is no longer the original stiff oil.

CONCLUSIONS

Flow simulations have helped us to understand which reservoir parameters control the scales of saturation. Patchy saturation has been mostly verified in laboratory measurements, and in well logs. Our study shows that we can also expect patchy behavior at the seismic scale. This chapter’s most important conclusion is that when gas is injected into

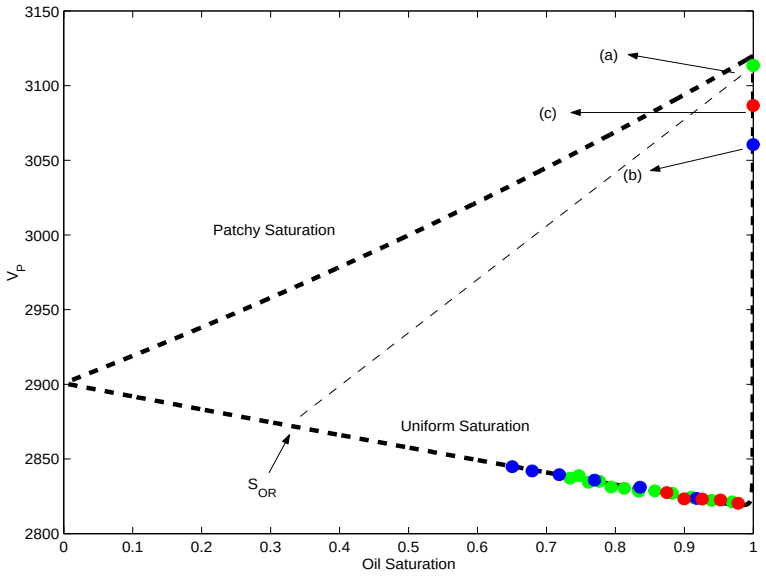

Figure 3.26: Gas out of solution: Velocity (m/s) versus gas-saturation for the saturation profiles in Figure 3.25.

oil-reservoirs, gravitational forces dominate, leading to the formation of sub-resolution gas-caps and hence causing patchy saturation at field scales. In this chapter, we also conclude that the uniform saturation model is appropriate for most waterfloods and for primary production scenarios when gas comes out of solution.

In their laboratory experiments, Knight and Cadoret observed uniform saturation during imbibition, and patchy saturation during drainage. It is interesting to note our flow simulations lead to similar conclusions, i.e., imbibition (waterflooding a water-wet reservoir) leads to uniform saturation, while drainage (gas injection) leads to patchy saturation. However, the underlying physical mechanisms leading to the result are different in the two cases. In the lab-scale measurements capillary forces dominate, while in the field-scale simulations gravitational and viscous forces dominate in determining the saturation scales.

Another important conclusion is that knowing the residual saturations of the fluid components in the reservoir narrows the uncertainty in saturation scales by a large amount. The values of the residual saturation can be used to modify the upper patchy bound so that it lies closer to the lower bound. The residual saturation thus constrains the seismic velocity. We call the new upper bound the modified patchy bound. The modified patchy bound can

be calculated using equations (3) - (6) and (10) - (12) in the chapter. This bound gives a much better approximation of the velocity-saturation response in cases of gas injection and is also a valid upper bound for waterfloods and other production scenarios, given the respective values of residual saturation. Other factors that also affect the saturation scale, but to a smaller degree, are wettability of the rock, the mobility ratios of the fluids, and the permeability distribution in the reservoir.

Chapter 4

A RESERVOIR MONITORING CASE STUDY

ABSTRACT

The goal of this chapter is to quantitatively interpret and analyze time-lapse seismic data to better understand sub-surface fluid saturations and saturation scales. We present a case study of a time-lapse seismic survey in which water and gas were injected into an oil-producing reservoir. Repeat seismic surveys were collected to monitor the subsurface fluids. In this study, we show that the sub-resolution spatial distribution of fluids can impact the seismic response. Although there is a good *qualitative* match between the fluid changes predicted by the flow simulator and the fluid changes interpreted from the seismic, the simulator predicts very smooth saturation profiles, which do not *quantitatively* match the time-lapse seismic changes. We find that *downscaling* of smooth saturation outputs from the flow simulator to a more realistic patchy distribution was required to provide a good quantitative match with the near and far offset time-lapse data, even though the the fine details in the saturation distribution were below seismic resolution. We downscaled the smooth saturations from the simulator by incorporating high spatial frequencies from the well logs, while constraining them to the total mass balance predicted by the flow simulator and varying only the vertical spatial distribution. The computed seismic response of the downscaled saturation distributions matched the real time-lapse seismic much better than the saturation distributions taken directly from the simulator.

INTRODUCTION

Time-lapse interpretation is the process of relating observed changes between repeat seismic surveys to changes in pore fluid saturations. Barr (1973) introduced the idea of seismically monitoring subsurface changes in fluid properties due to injection of waste materials in disposal wells. He based the proposal on changes in the reflection coefficient that would arise as a result of fluid substitution. Nur (1982) proposed the use of repeat seismic surveys to monitor the process of enhanced oil recovery, specifically during steam injection, to recover heavy oil. Since then, several case studies have been reported in which time-lapse seismic surveys were conducted to monitor subsurface fluid changes (Greaves and Fulp, 1987, Pullin et al., 1987, Eastwood et al., 1994, Johnston et al., 1998).

So far, many of the interpretations of time-lapse data have been limited to qualitative before-after comparisons. Sonneland et al. (1997) describe the successful monitoring of oil-water movement in the Gulfaks field in the Norwegian North Sea, where fluid distribution changes before and after production match with flow simulation results, but only qualitatively. Watts et al. (1996) report a time-lapse analysis where synthetic seismic modeling showed a good qualitative agreement with field seismic data. In their study, there was an 8 % change in Poisson's ratio due to fluids, but quantitative differential AVO techniques, while suggested, were not actually pursued. Johnston et al. (1998) reported that differences in seismic impedance and the pattern of flat spots could be interpreted in terms of changing fluids, but again, qualitatively.

Quantitative interpretation of time-lapse data poses several challenges, mostly due to the non-unique response of seismic to fluid changes. In many cases, correct interpretation cannot be made without additional information to constrain the seismic interpretation. Reservoir flow simulation can play a significant role in constraining the inherent non-uniqueness in seismic signatures, because time-lapse seismic interpretation can be validated through comparison to flow simulation results and reservoir engineering concepts.

An important issue regarding the role of flow simulation in seismic reservoir monitoring is the simulator grid size. It is always desirable to have the flow simulation grid as fine as possible to capture the details of reservoir heterogeneity and the spatial saturation distribution. For practical considerations, there is always a compromise between the desire to capture the details and the availability of computational resources. Consequently, flow simulation results are always spatial averages over large blocks. Proper rock physics conversion of fluid changes to seismic changes always requires some estimate of fluid changes at much smaller scales, and may require refinement of the simulator models.

Some time-lapse studies have reported variations between flow simulation results and observed seismic changes, indicating that improvement of coarsely gridded simulator models was desirable. He et al. (1998) described an integrated time-lapse seismic inversion project in a water-driven and gas cap expansion sand reservoir. The project involved reservoir description, reservoir flow simulation, and comparison of observed and predicted seismic impedance differences between 1985 and 1992, and required update of the porosity of the initial reservoir model. Johnstad et al. (1995) reported a monitoring study where

changes in the seismic signature could be interpreted to show approximately the gas front configurations. However, there were some mismatches between the seismic results and flow simulation results, indicating a need for model refinement.

The goal of this chapter is to quantitatively interpret and analyze time-lapse seismic data to better understand sub-surface fluid saturations and saturation scales. We present a case study of a time-lapse seismic survey in which water and gas were injected into an oil-producing reservoir. Repeat seismic surveys were collected to monitor the subsurface fluids. In this monitoring case study, we show that coarsely gridded simulator predictions of saturation changes do not quantitively match the time-lapse seismic. We also show that downscaling of the smooth simulator saturations to a more realistic patchy distribution is required to provide a quantitative match with the near and far offset time-lapse data.

The reservoir sands that we studied in this chapter are Triassic-Jurassic in age, deposited in a fluvial alluvial environment. The reservoir is characterized by a range of fluvial styles ranging from isolated channel sands to braided sheetlike belts. This highly heterogeneous environment results in significant challenges for efficient oil recovery by water and gas injection.

It has been shown in the previous chapters and also by various authors, that sub-resolution scales of fluid distribution may affect the changes in seismic observables (Mavko and Mukerji, 1998, Sengupta and Mavko, 1998). In this chapter we combine coarse-scale saturation changes from the flow-simulator with fine-scale well logs to quantitatively model AVO signatures caused by production related fluid changes.

We generated synthetic CDP gathers from the original and fluid-substituted V_P, V_S, and density data from well logs. These synthetic CDP gathers were used to estimate the changes in differential AVO attributes which were then compared to the changes in differential AVO attributes seen in the field data. At first, we used Gassmann's (1951) fluid substitution recipe and saturation distributions taken directly from flow simulators, but obtained a poor quantitative match with the time-lapse AVO data. We then downscaled the simulator-predicted saturations by introducing more realistic spatial roughness to the saturation changes modeled after the variability observed in the well logs. This yielded a much better quantitative match to the time-lapse AVO attributes.

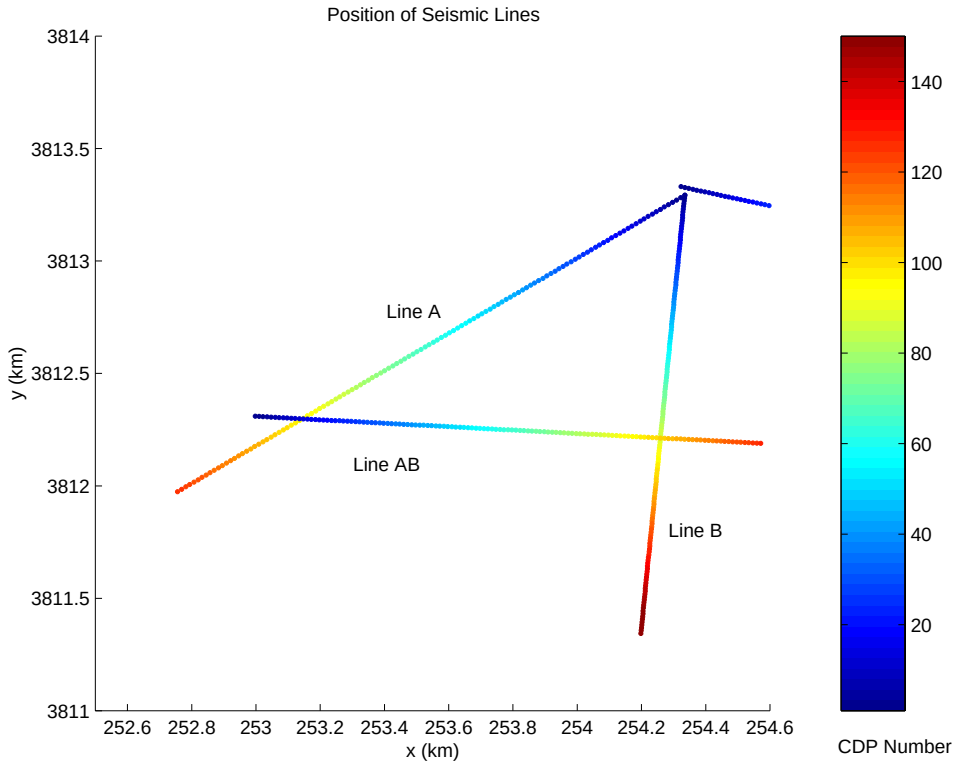

Figure 4.1: Map view showing positions of seismic lines A, B, and AB. The horizontal projection of well A lies along seismic line A, and the horizontal projection of well B lies along seismic line B. Well A intersects line AB near CDP 10 and well B intersects line AB near CDP 101. The flow-simulator profile (shown later in Figure 4.9) lies in the same vertical plane as the seismic line AB.

AVAILABLE DATA

Seismic data from two surveys, 1983 and 1997, were used in this study. Near offset (5-15^o), mid offset (15-25^o), and far offset (20-30^o) stacks, as well as full stacks were available for both surveys. Figure 4.1 shows the position of the seismic lines A, B, and AB. The injector well A lies approximately in the plane of seismic line A, and the producer well B lies approximately in the plane of seismic line B. Well A intersects seismic line AB near CDP 10, and well B intersects seismic line AB at CDP 101.

Figures 4.2 shows the repeat seismic data of line AB, and the projections of wells A and B on the seismic section AB. The injector well A intersects line AB near CDP 10, at a depth of 2.5 seconds, and the producer well B intersects line AB at CDP 101, at a depth

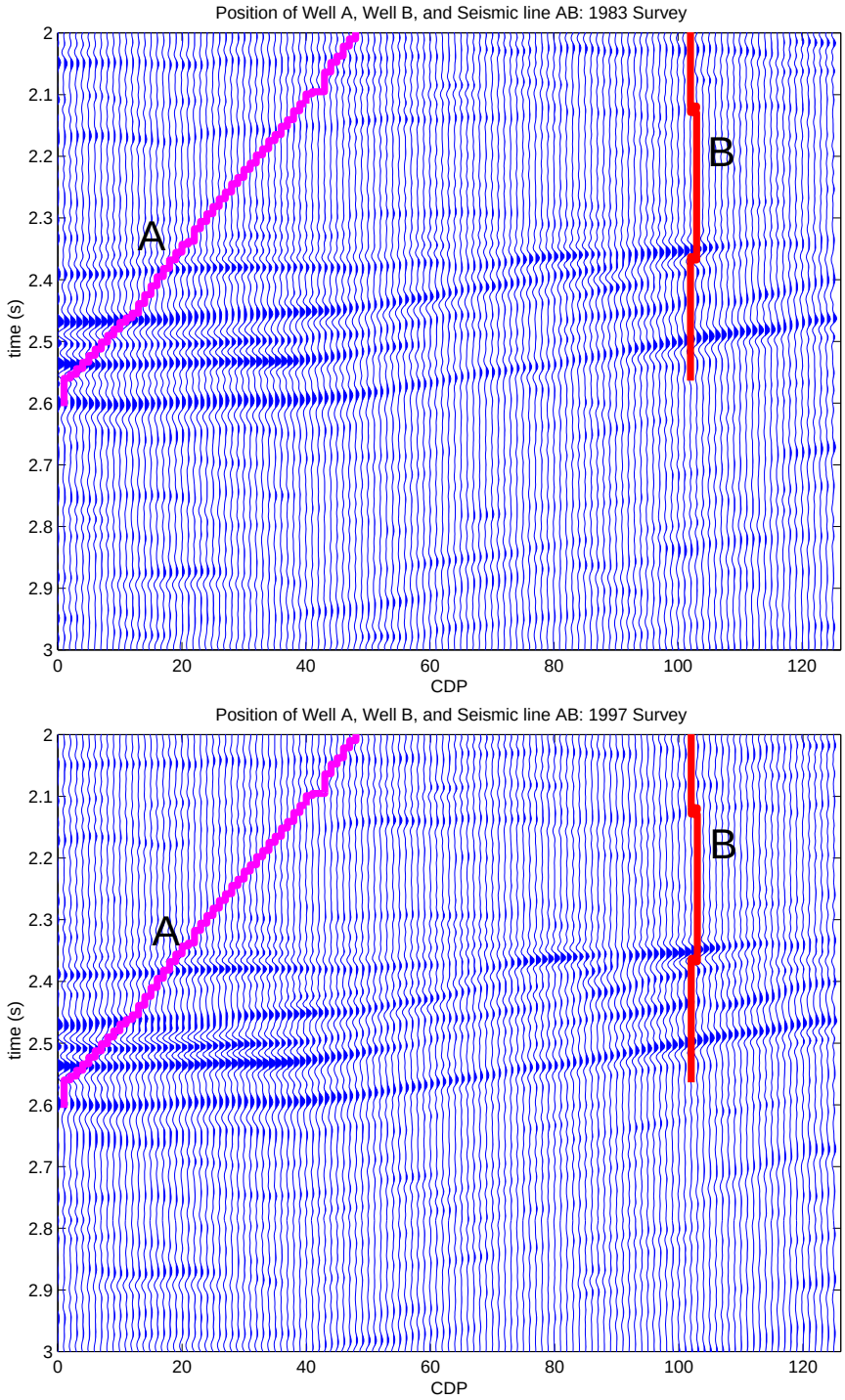

Figure 4.2: Well A, well B, and seismic line AB: 1983 and 1997 surveys. Wells A and B lie out of the plane, but intersect the seismic line at CDPs 10 and 101 respectively.

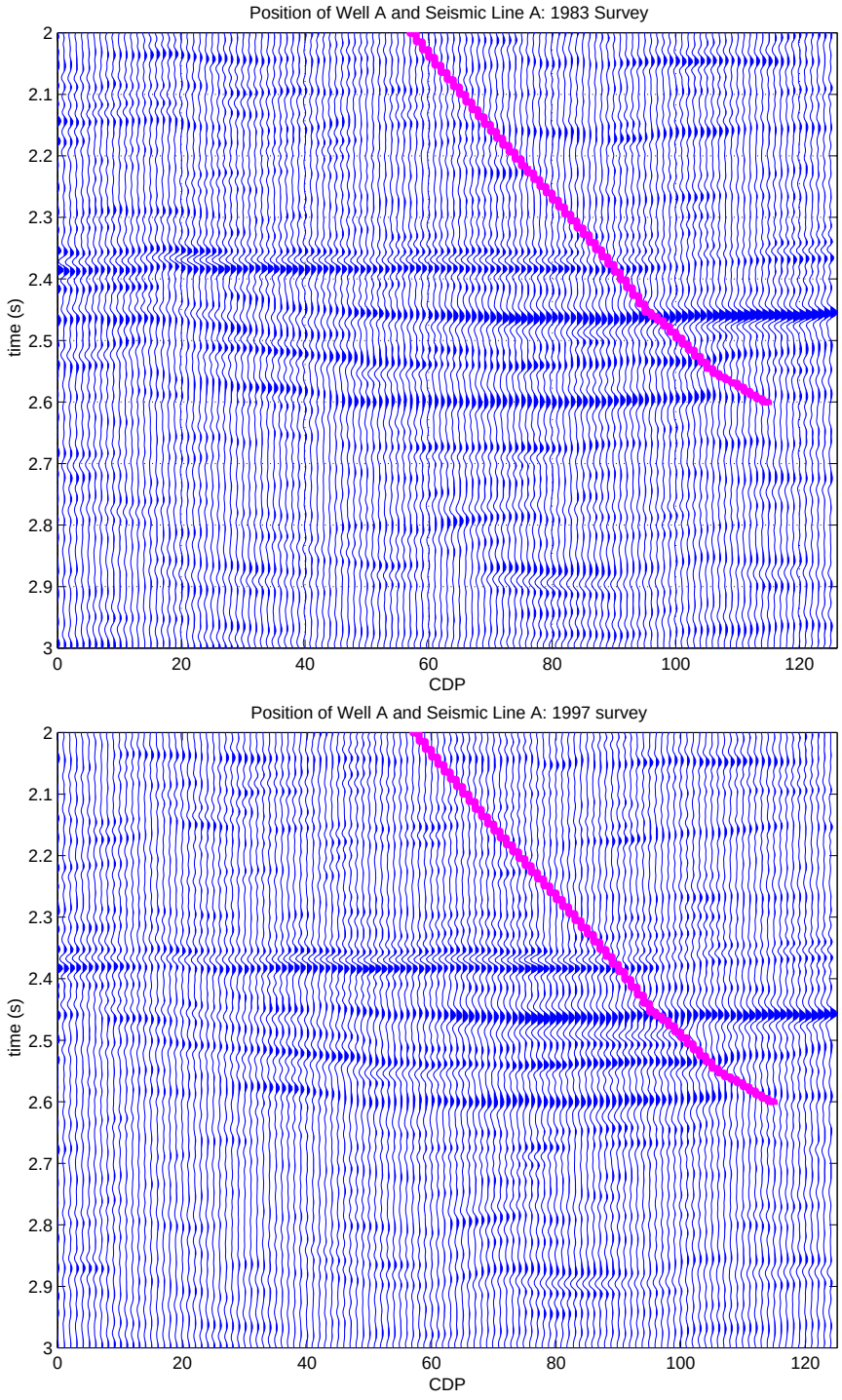

Figure 4.3: Well A and seismic line A: 1983 and 1997 surveys. Well A lies in the plane of seismic line A.

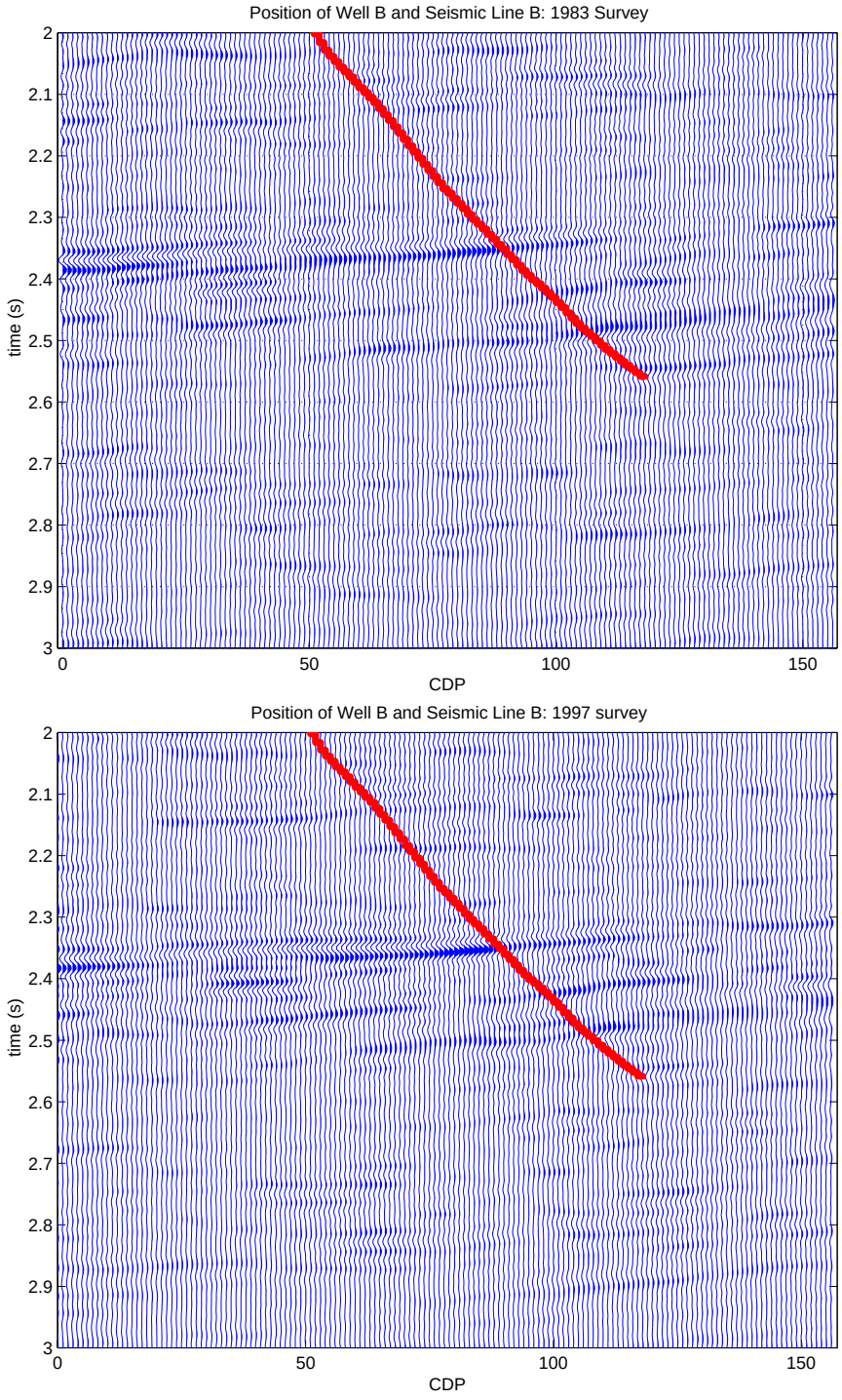

Figure 4.4: Well B and seismic line B: 1983 and 1997 surveys. Well B lies in the plane of the seismic line B.

of 2.4 seconds. Figure 4.3 shows the near offset stacks for the repeat surveys along line A, and also the position of the well A relative to seismic line A. Figure 4.4 shows the well position and seismic data for well B and seismic line B.

We computed the difference sections of seismic amplitude attributes from the before (1983) and after (1997) partially stacked data. Figure 4.5 shows the seismic differences for all three partial stacks of seismic line AB. Since subsurface fluid changes can cause traveltime differences between the repeat seismic surveys, straightforward differencing of the wiggle traces will give rise to spurious signatures. In order to eliminate these spurious signatures, we computed the root mean square (RMS) amplitude of each partial stack over a moving window of 50 milliseconds. In this case, mostly amplitude changes are observed, so subtraction is appropriate. The difference stacks shown in Figure 4.5 are the differences between the RMS amplitudes computed on the 1983 and 1997 surveys. We observe time-lapse changes in RMS amplitude near both the wells A and B in Figure 4.5, while there appears to be little or no change between the wells. We compute time-lapse differential AVO attributes from the near offset ($5^o - 15^o$) and mid offset ($15^o - 25^o$) field data of 1983 and 1997. (The far offset ($20^o - 30^o$) data files were not available for some of the seismic lines.) The time-lapse attribute we computed is the percent change in root mean square (RMS) amplitude:

$$\Delta_{RMS} = 100 \frac{A_{RMS}(1997) - A_{RMS}(1983)}{A_{RMS}(1983)} \tag{4.1}$$

We compare these attributes computed from real data with modeled attributes in later sections of this chapter.

Figure 4.6 shows the frequency spectra of the near and mid offset seismic data from the repeat surveys in line AB. We observe that the frequency content of the near and mid offset data, as well as the before and after surveys is consistent, with a frequency band of 10 to 60 Hz.

Well log data are available from well A, (which intersects seismic lines A and AB) and well B (which intersects seismic lines B and AB). Well logs of porosity, shale volume fraction, permeability, water saturation, density, and V_P are available in both wells A and B. However, V_S is available only in well B. Fluid substitution in

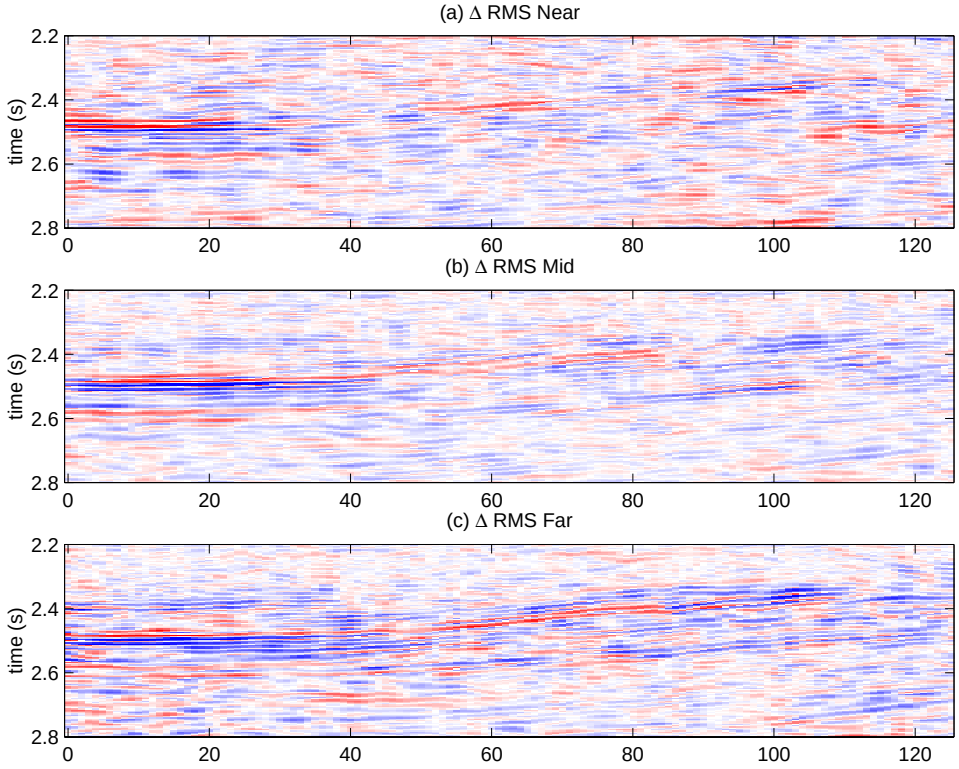

Figure 4.5: Line AB: Difference of RMS amplitudes between the 1983 and 1997 surveys in the near (5-15^o) and mid (15-25^o) offset stacks.

the absence of V_S involves various approximations and assumptions (Mavko et al., 1995, Greenberg and Castagna, 1992). Since well B contains all the information required for Gassmann's fluid substitution recipe, it is more reliable for fluid substitution predictions, and was therefore considered the key well in this study.

Figure 4.7 shows data from the producer well B. The well log data represent initial, i.e., pre-production conditions of the reservoir, when there was no gas in the reservoir. The zone of interest in this well is between the depths of 2340 and 2440 meters. This figure shows that the reservoir consists of heterogeneous sand-shale layers. As expected, the reservoir sands have high porosity and low water saturation (S_w), while the shales have low porosity and high water saturation. The oil saturation ($S_o = 1 - S_w$), sand volume fraction (1-V_{shale}), and the porosity (ϕ) are quite well correlated.

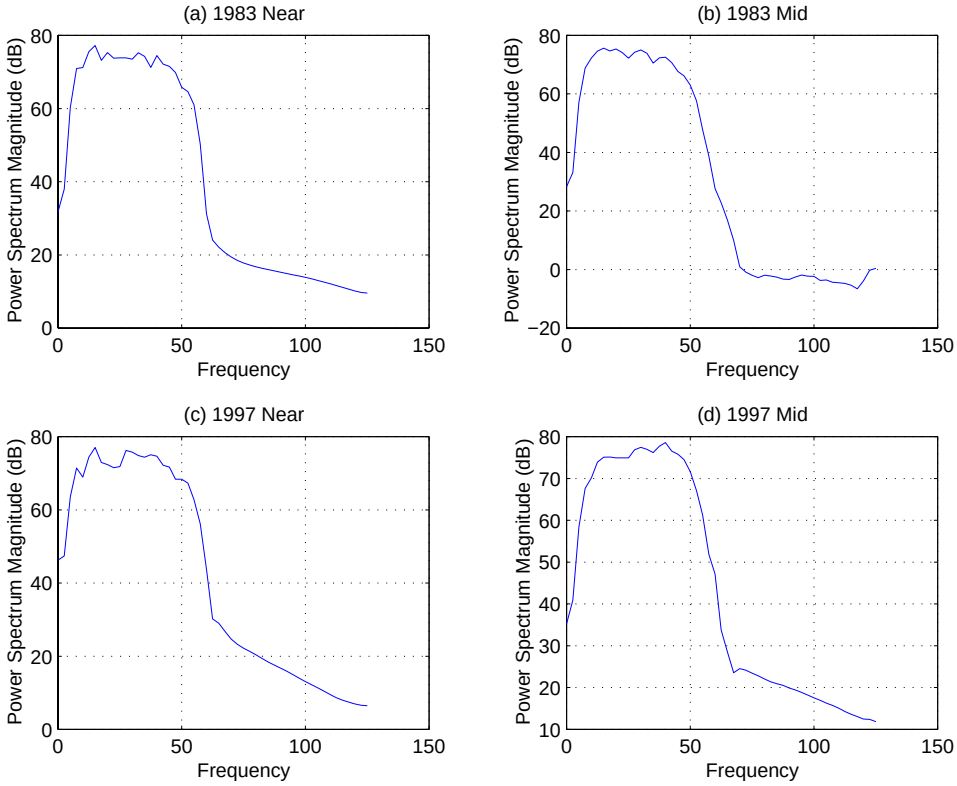

Figure 4.6: Power spectra of the real seismic data from line AB.

Figure 4.8 shows data from well A, which is the injector well. The depth of interest in this well lies between 2500 and 2600 meters. Data from well A also correspond to pre-production conditions when there was no gas in the reservoir. Like well B, well A shows that the sands have high porosity and low S_w, while the shales have low porosity and high S_w, indicating a good correlation between the sand volume fraction, the porosity, and the oil saturation. The V_S log was not available in well A, and was generated using a multivariate regression between the V_P, V_S, ϕ, and V_{shale} of well B to predict V_S from V_P, ϕ, and V_{shale} in well A.

Fluid properties at the reservoir conditions are tabulated below.

A 100 meter thick section of the reservoir **flow simulation data**, aligned approximately along the plane of seismic line AB was available. The flow simulation data consist of the input model parameters: porosity, permeability, and initial water and gas saturations, as

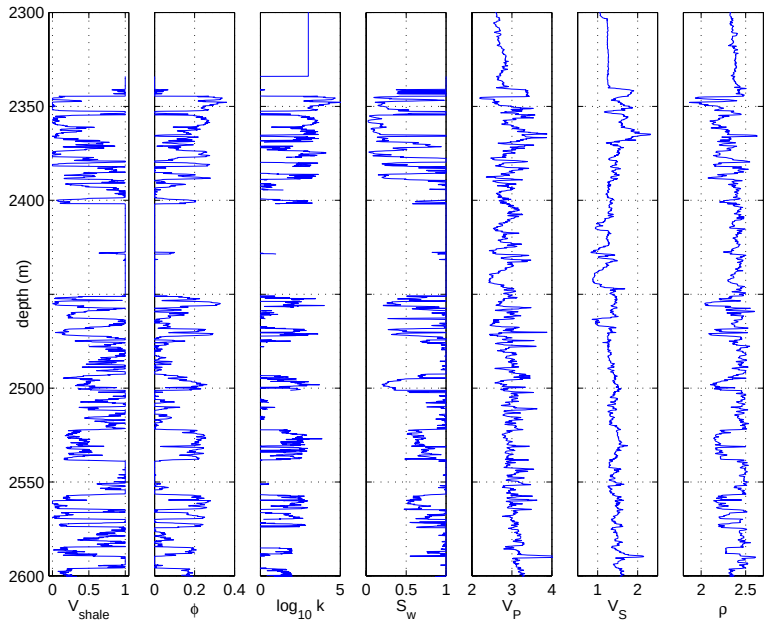

Figure 4.7: Log data from the producer well B.

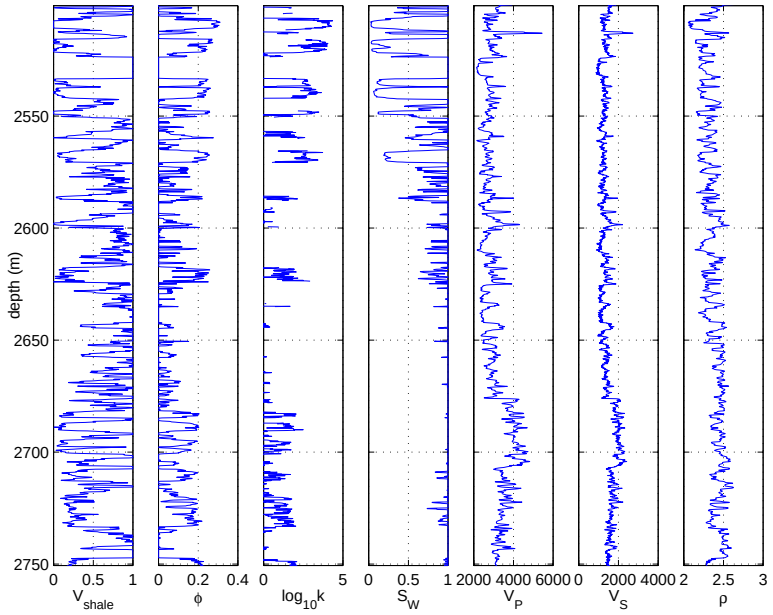

Figure 4.8: Log data from the injector well A. V_S was unavailable in this well, and was generated using a multivariate regression calibrated to well B.

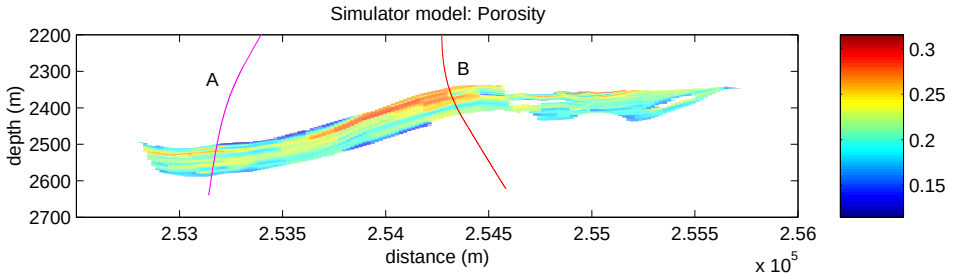

Figure 4.9: Section of porosity model input to the flow-simulator and along seismic line AB, along with the positions of injector well A and producer well B.

well as the outputs: the final water and gas saturation profiles. Figure 4.9 shows the flow simulator model of porosity, along with the position of wells A and B. The simulator model

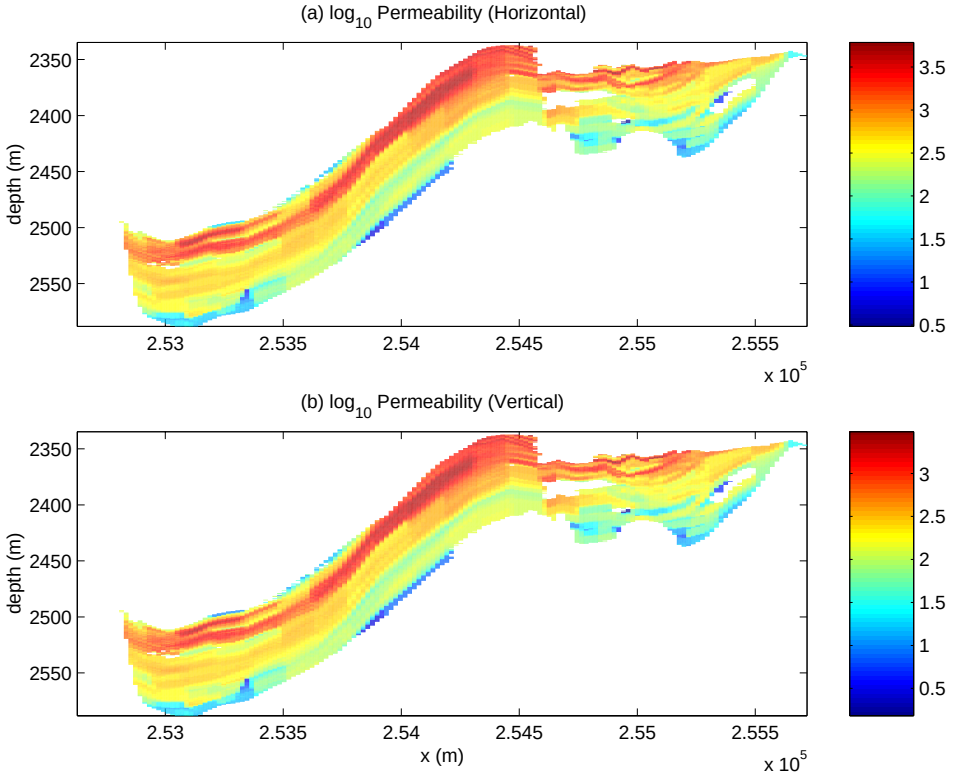

Figure 4.10: Flow-simulator permeability model.

Table 4.1: Fluid properties at the reservoir conditions

Fluid	Density (ρ) kg/m^3	Bulk modulus (K) GPa
Water	1000	2.25
Oil	750	1.20
Gas	70	0.06

extends further to the right than the seismic line. Figure 4.10 shows model of the horizontal and vertical permeability input to flow simulator.

The initial and final water saturations are shown in Figure 4.11, and the initial and final gas saturations are shown in Figure 4.12. As these figures show, both water and gas were injected into the reservoir from the left (well A). However, we expect the effect of gas injection to dominate the seismic response, based on the analyses in previous chapters, because gas is highly compressible compared to both oil and water. Our impedance inversion results, which we present in the next section, confirm this expectation. Comparing the final gas saturation profile in Figure 4.12 with Figure 4.5, we can qualitatively observe that large seismic differences are observed where the the simulator predicts large accumulations of gas, specifically near the wells A and B. In a later section in this chapter we discuss the quantitative relations between the simulator results and the observed seismic changes.

SYNTHETIC SEISMIC MODELING OF FLUID CHANGES WITHOUT USING FLOW SIMULAT OR OUTPUTS

We modeled “before” and “after” synthetic seismograms and compared the time-lapse differential AVO attributes defined in Equation (4.1) to the attributes derived from the field seismic data using the following steps:

- statistically extracted a wavelet from the field seismic data (The frequency spectrum of the extracted wavelet shown in Figure 4.13 shows a good match with the frequency spectrum of the real seismic (Figure 4.6)

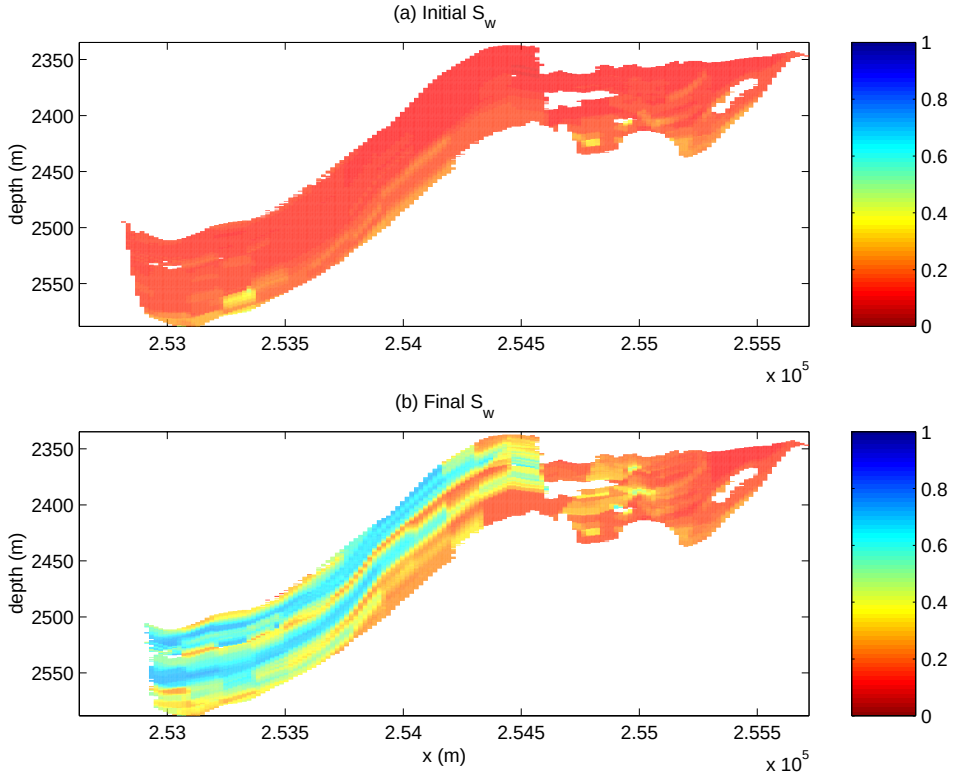

Figure 4.11: Initial and final water saturation from the flow-simulator. Water is injected from the left.

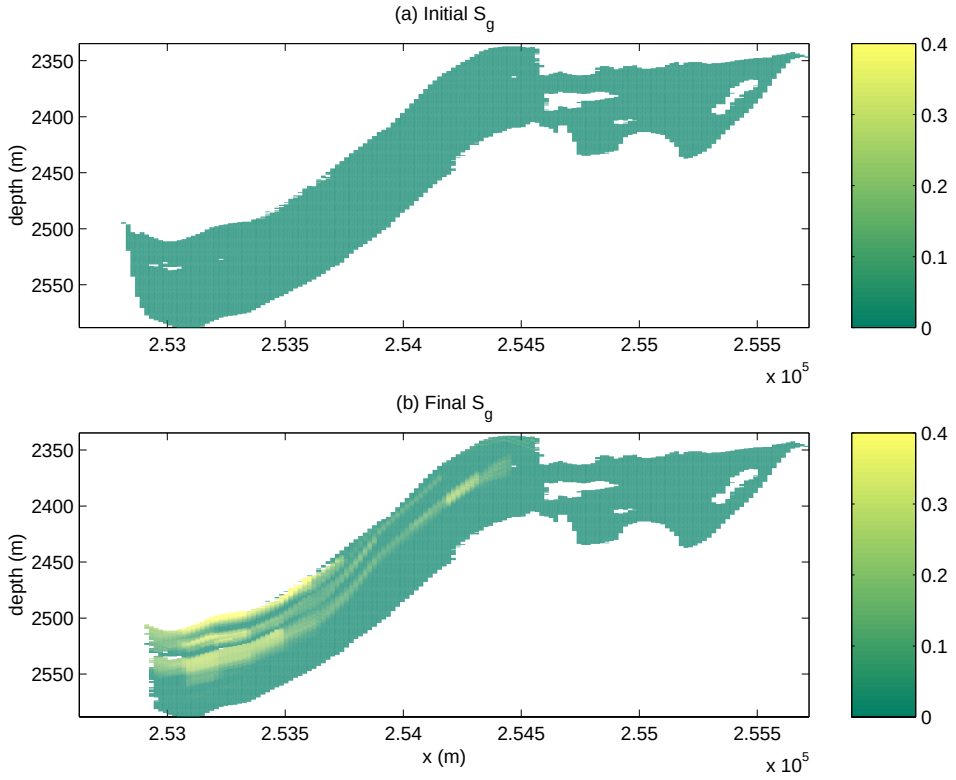

Figure 4.12: Initial and final gas saturation from the flow-simulator. Gas is injected from the left.

- generated synthetic seismograms as a function of offset angle from the original well logs
- independent of any flow simulator results, we introduced varying thicknesses of gas in the well logs, assuming that injected gas replaces the oil in the high porosity, high permeability zones in the well logs
- performed fluid substitution in the well logs to replace the original oil saturations with the gas saturations shown in Figure 4.14 (where light blue represents oil and red represents injected gas)
- generated synthetic seismograms as a function of offset angle from the fluid-substituted well logs

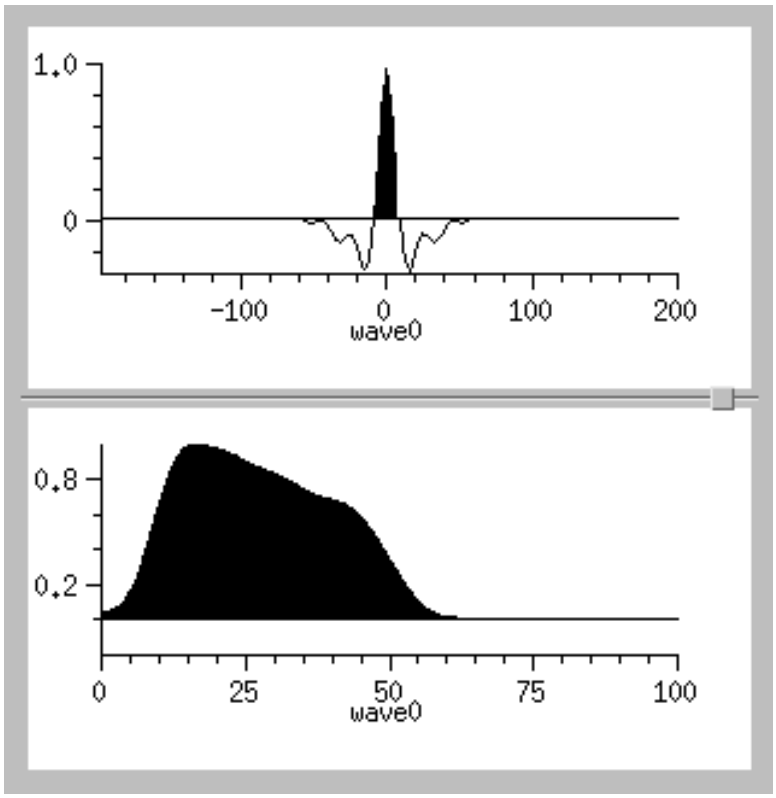

Figure 4.13: Top panel: wavelet extracted from the real seismic data and used in generating synthetic seismograms. Bottom panel: power spectrum of the extracted wavelet.

- computed time-lapse differential AVO attributes from the “before” and “after” synthetic seismograms
- compared real time-lapse differential AVO attributes with the synthetic time-lapse differential AVO attributes.

From this exercise, we found that the total vertical thickness of gas can greatly impact the time-lapse seismic signatures. Figure 4.15 shows the time-lapse attributes (defined in Equation (4.1)) derived from the field data, plotted along with the synthetic time-lapse seismic attributes. The pink dots represent seismic data from line AB near well B, while the blue dots represent seismic data from seismic line B near well B. Each model is labeled with the corresponding gas thickness. The error bars on the model prediction correspond

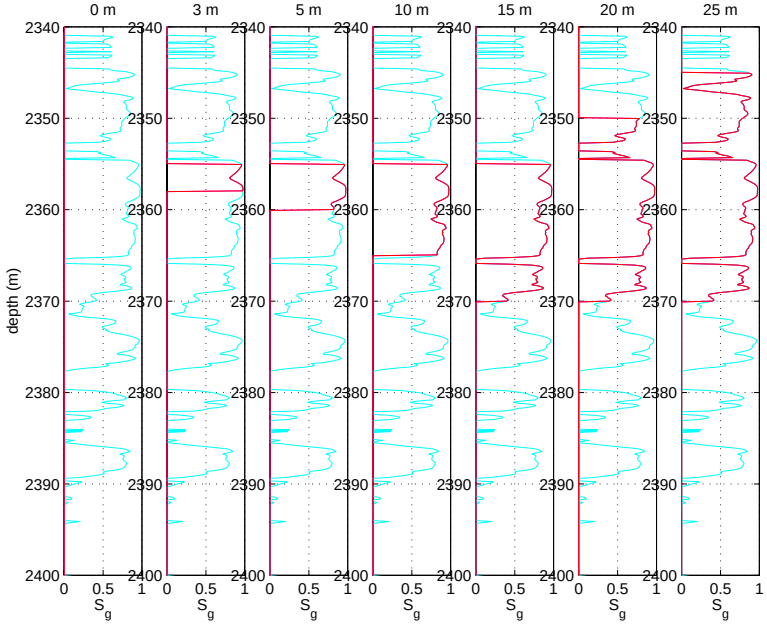

Figure 4.14: Saturation profiles used in synthetic seismic modeling. The light blue curves indicate oil saturation, and the red curves indicate gas saturation.

to the uncertainty in synthetic seismic attributes due to lack of information about spatial distribution and total amount of gas, and is explained in more detail in the next paragraph. This figure shows that the magnitudes of the near and mid amplitudes are correlated with the thickness of the gas zone, but with considerable overlap. The estimated uncertainty due to variable spatial scales, arangements, and relative amounts of fluids is very large, as indicated by the error bars in the modeled attributes.

The uncertainty in the interpretation of the seismic signature is demonstrated in Figure 4.16, which shows how sub-resolution saturation scales and spatial arrangements can affect the seismic reflectivity. Figure 4.16 also shows that the seismic reflectivity is very sensitive to the total thickness of gas in the reservoir. The reflectivities were computed from synthetic normal-incidence seismograms of stochastically simulated sub-resolution saturation distributions in the well logs. Each realization of spatial gas distribution was simulated by drawing from a binomial distribution with a given probability, and a given scale of saturation. For example, for a saturation scale of 5 meters, the well log was divided into vertical 5-meter zones, and each zone was assigned a value of zero or one by drawing from the

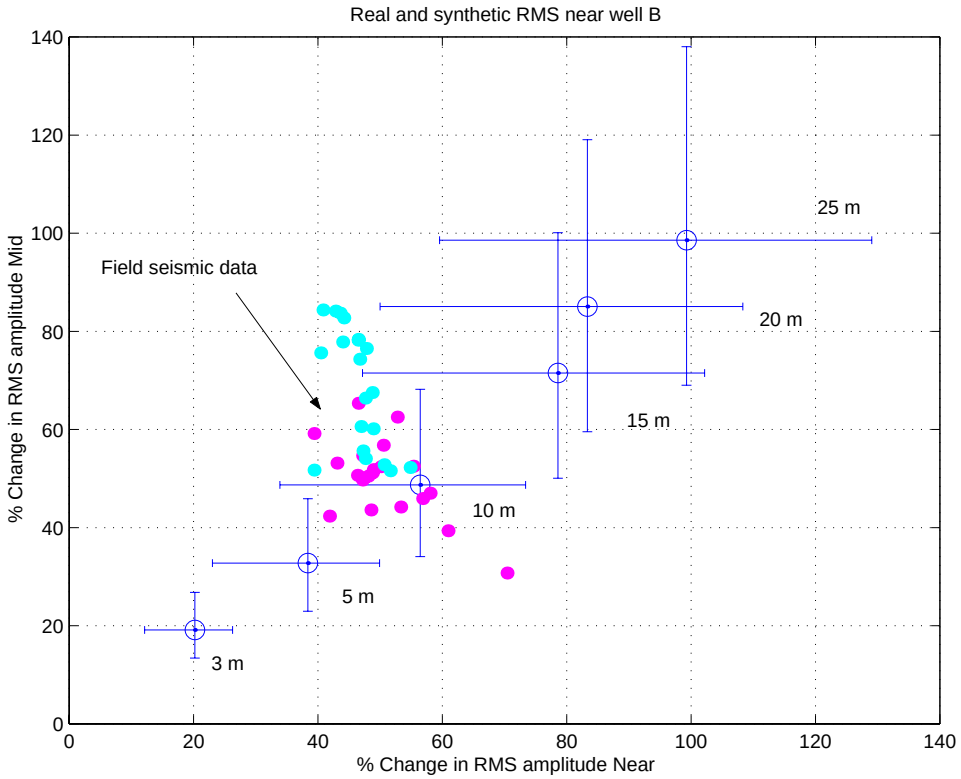

Figure 4.15: Cross plot of real (pink and blue dots) and synthetic (open circles with error bars) time-lapse differential AVO attributes. The synthetic attributes are computed from CDP gathers generated from fluid substitution in well logs. The models show the sensitivity of the amplitude change on both near and mid stacks to total thickness of gas.

binomial distribution. The sand layers in each zone that was assigned a value of one were fluid-substituted with gas. Fluid substitution was always done at the log sampling. The corresponding synthetic seismograms were computed, and for each seismogram, the amplitude at the top of the reservoir was picked. The three different saturation scales in Figure 4.16 correspond to mean thicknesses of individual gas layers: 5 m ($\lambda/10$), 1 m ($\lambda/50$), and 0.2 m ($\lambda/250$), where λ is the seismic wavelength. We do not consider larger saturation scales, because at about $\lambda/5 - \lambda/4$, the individual patches would begin to get resolved, and then it would be any more sub-resolution uncertainty, which is the focus here. The circles, squares, and stars in Figure 4.16 correspond to the three sub-resolution scales, and the three lines are best-fit polynomials that describe the trend of reflectivity corresponding to

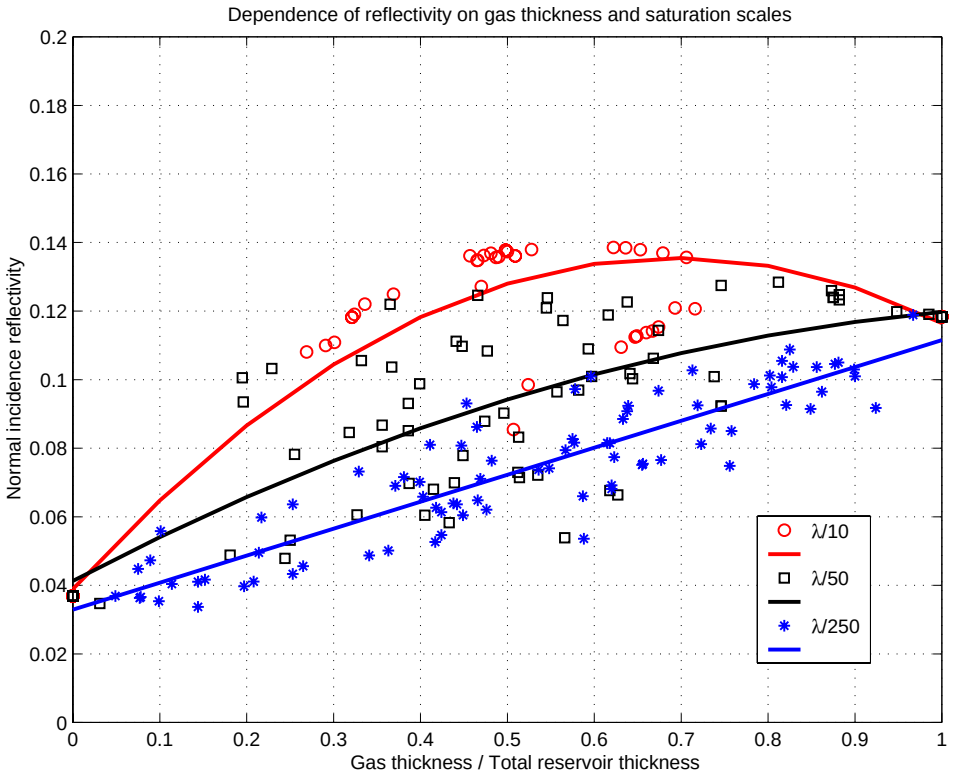

Figure 4.16: Normal incidence reflectivity versus normalized total gas thickness. Saturation scales introduce non-uniqueness in seismic interpretation. Three different sub-resolution saturation scales, defined by the mean thickness of individual gas layers: 5 m ($\lambda/10$), 1 m ($\lambda/50$), and 0.2 m ($\lambda/250$), where λ is the seismic wavelength. The lines correspond to best-fit polynomials around the points for each saturation scale.

the respective saturation scale. At each scale, the scatter represents the variability or uncertainty due to different stochastic spatial arrangements of the gas layers. In this exercise, the total amount of gas in the reservoir is unconstrained, and therefore, the uncertainty in the interpretation of saturation changes is very large with a coefficient of variation (standard deviation (σ)/ mean(μ)) equal to 30 %. This coefficient of variation was used for the error bars in Figure 4.15. In the next section, we show how results from the flow simulator can constrain the saturation changes in the reservoir, and thus help to reduce uncertainty in the seismic interpretation.

SYNTHETIC SEISMIC MODELING OF FLUID CHANGES INCORPORATING FLOW SIMULAT OR RESULTS

We computed the time-lapse differential AVO attributes defined in Equation (4.1) from the "before" and "after" partial stacks of the seismic data. We then simulated the observed changes in these attributes using the following steps:

- extracted a wavelet from the real seismic data (shown in Figure 4.13)
- generated synthetic seismograms as a function of offset angle from the original logs from well B
- extracted saturation profiles from the flow simulator
- performed fluid substitution in the well logs to replace the original fluids with the new fluids predicted by the simulator
- generated synthetic seismograms as a function of offset angle from the fluid-substituted well logs (shown in Figure 4.17)
- computed time-lapse differential AVO attributes from the "before" and "after" synthetic seismograms
- compared real time-lapse differential AVO attributes with the synthetic time-lapse differential AVO attributes.

Fig 4.18 shows the AVO signature of the gas sands at the top of the reservoir. We observe a class III type behavior where the near offset reflectivity has a small negative value, and the magnitude of the reflection coefficient increases with offset.

Figure 4.19 shows the time-lapse attributes computed from real seismic traces around well B denoted by the pink and blue dots. The pink dots correspond to seismic data from line AB, while the blue dots correspond to data from line B. Figure 4.19 also shows a cross plot of the synthetic Δ RMS for the "near" (5-15^o) versus the "mid" (15-25^o) offsets.

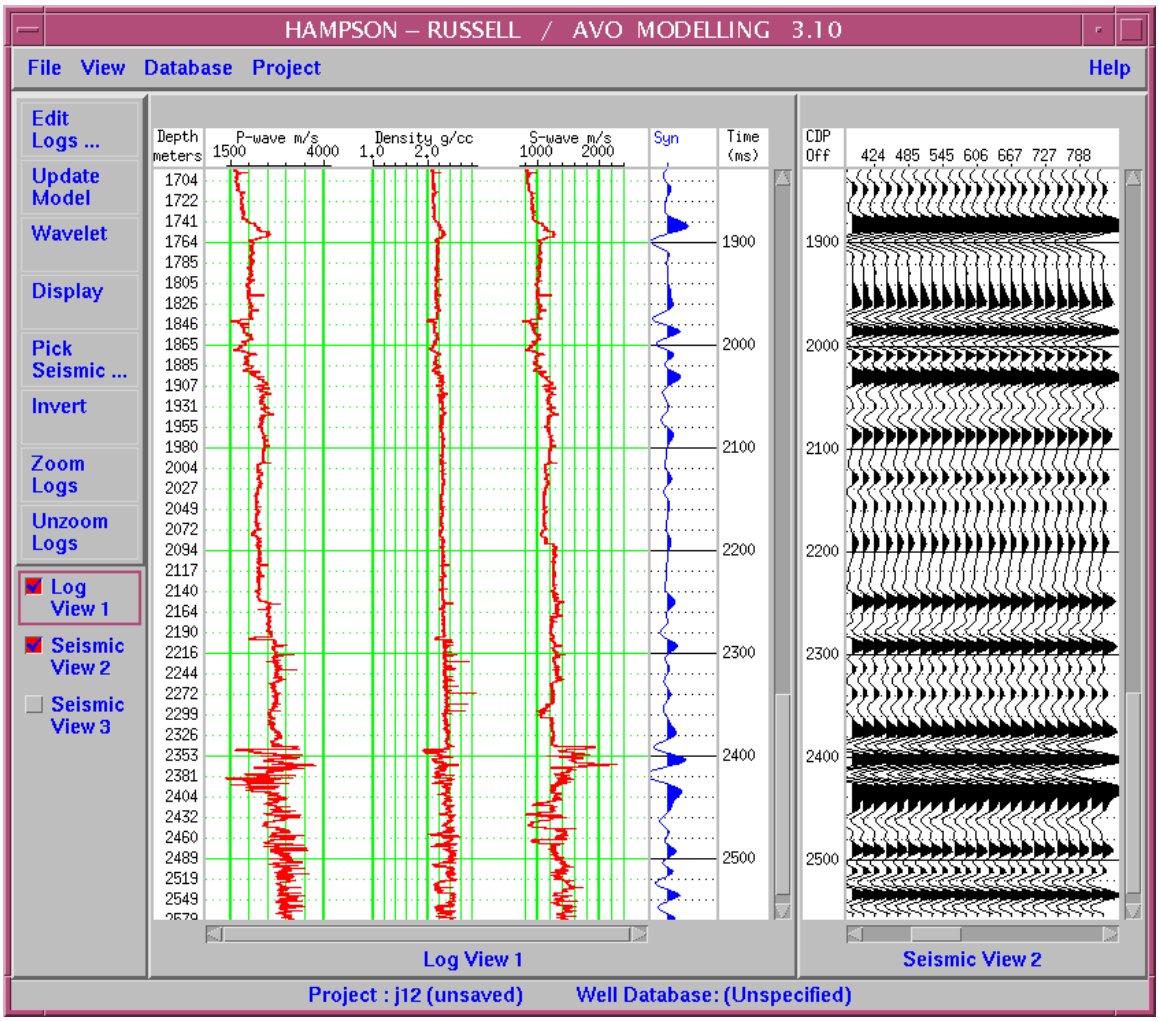

Figure 4.17: Logs from well B and corresponding synthetic gathers.

The modeling results shown in Figures 4.19 and 4.26 represent computations corresponding to smooth saturation profiles from the flow simulator. The error bars correspond to 1 standard deviation of the amplitude variation with offset around the amplitude of the mean offset angle. The variation in the amplitudes with angle corresponds to $5^o - 15^o$ in case of the near offsets and $15^o - 25^o$ in case of the mid offsets. This is a very low estimate of the actual uncertainty, because it takes only the amplitude variation into account, but

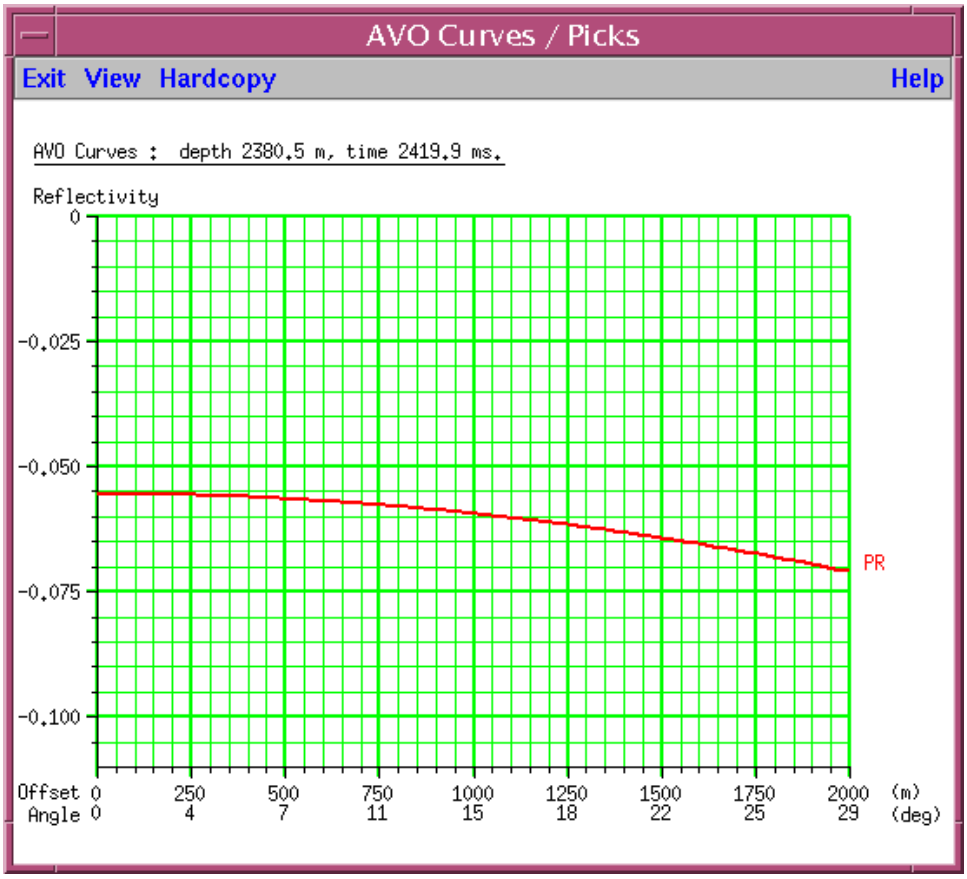

Figure 4.18: AVO signature at the top of the reservoir.

does not account for uncertainties due to spatial arrangements or saturation scales. We observe that there is a mismatch between the observed attributes and the attributes computed from smooth simulator-scale saturations. In the next section, we show how artificially smooth saturation distributions predicted by the flow simulator output provide one possible explanation for the mismatch.

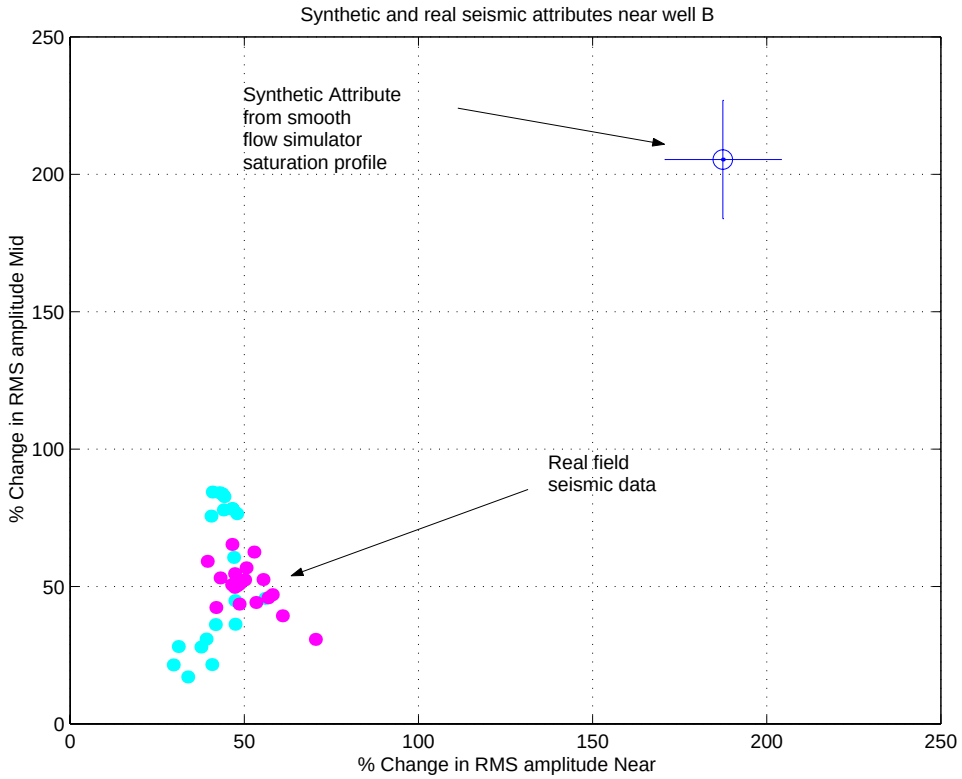

Figure 4.19: Cross plot of real and synthetic time-lapse differential AVO attributes near well B.

COMPARING FLOW SIMULATOR MODEL WITH WELL LOG DATA

Figure 4.20 shows the permeabilities (k), porosities, and initial water saturations from the well log B and the flow simulator model. In Figure 4.20, the panel labelled S_g/o corresponds to the final gas saturation from the simulator, the initial oil saturation in the well. The purpose of this display is to compare the vertical roughness observed in the well data with the simulator model. It is easy to observe that the simulator properties are much smoother than the well log properties in well B. The well log data show a much higher vertical resolution (or roughness) than the simulator model. The original well log was sampled at 0.1 meters, while the simulator is sampled at 0.5 meters. The smooth property is not just

a matter of coarser sampling.

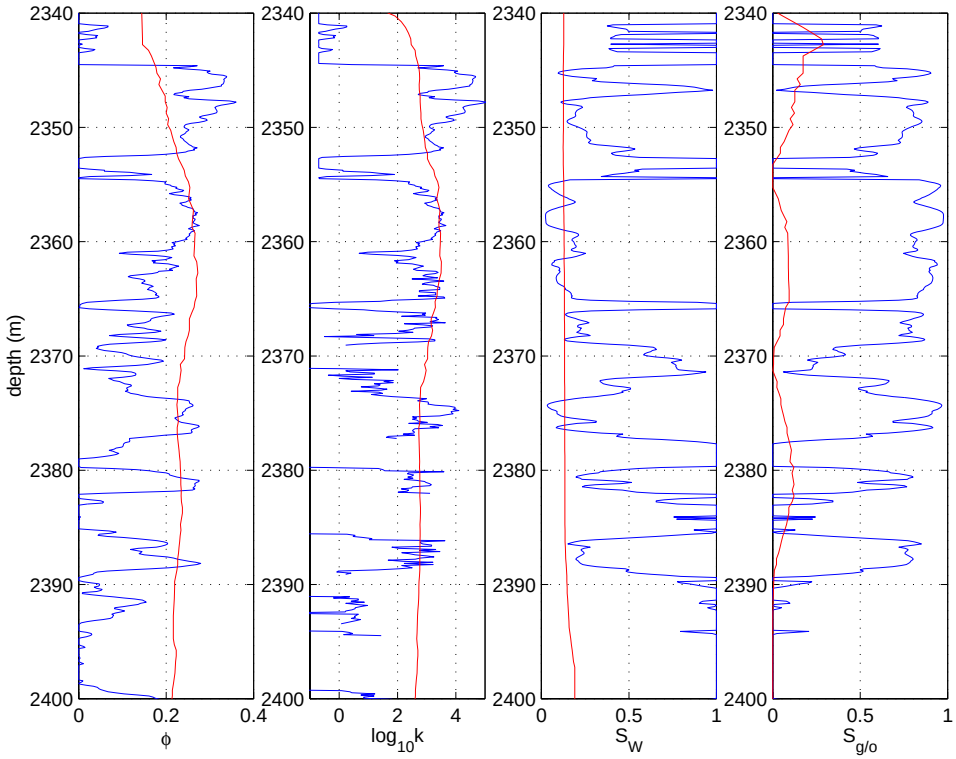

Figure 4.20: Comparing well-log and simulator properties: The red (smooth) curves correspond to the flow simulator, while the blue (rough) curves correspond to the well log B. Left to right: ϕ=Porosity, k=permeability, S_W=water saturation, and S_g/o = simulator gas saturation and well log oil saturation.

The flow simulator model is smooth compared to the well log for various reasons. The simulator model is obtained by estimating volumetric averages around the well, which introduces some amount of spatial smoothing. In order to increase computational efficiency in running the flow simulations, reduction in spatial sampling becomes necessary, and is done by upscaling the well log properties. Excessive spatial smoothing, however, adversely impacts seismic modeling and interpretation, as we demonstrate in this section.

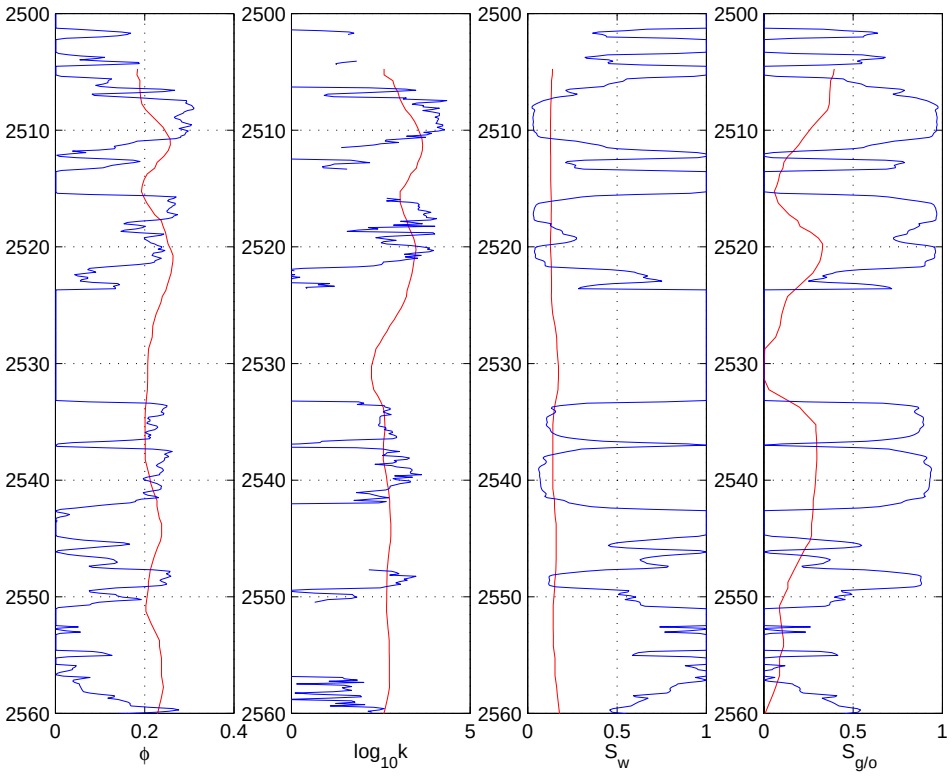

Figure 4.21: Comparing well-log and simulator properties: The red curves correspond to the flow simulator, while the blue curves correspond to log data from well A. Left to right: ϕ=Porosity, k=permeability, S_W=water saturation, and S_g/o = simulator gas saturation and well log oil saturation.

DOWNSCALING SATURATIONS

One reason for the mismatch between the real seismic attributes and the synthetic attributes could be fine scale spatial saturation heterogeneities that lie below the resolution of the flow simulator blocks. As discussed in detail in Chapter 3, seismic waves are affected not only by pore fluid saturation, but also by the spatial distribution of the saturation. We present a strategy for constraining subresolution saturation scales by integrating smooth flow-simulator predicted saturations and high spatial frequencies from well logs with near, mid, and far offset time-lapse seismic data.

Figure 4.20 shows that the simulator model of the permeabilities, porosities, and initial fluid saturations are much smoother than the same properties computed from the well logs,

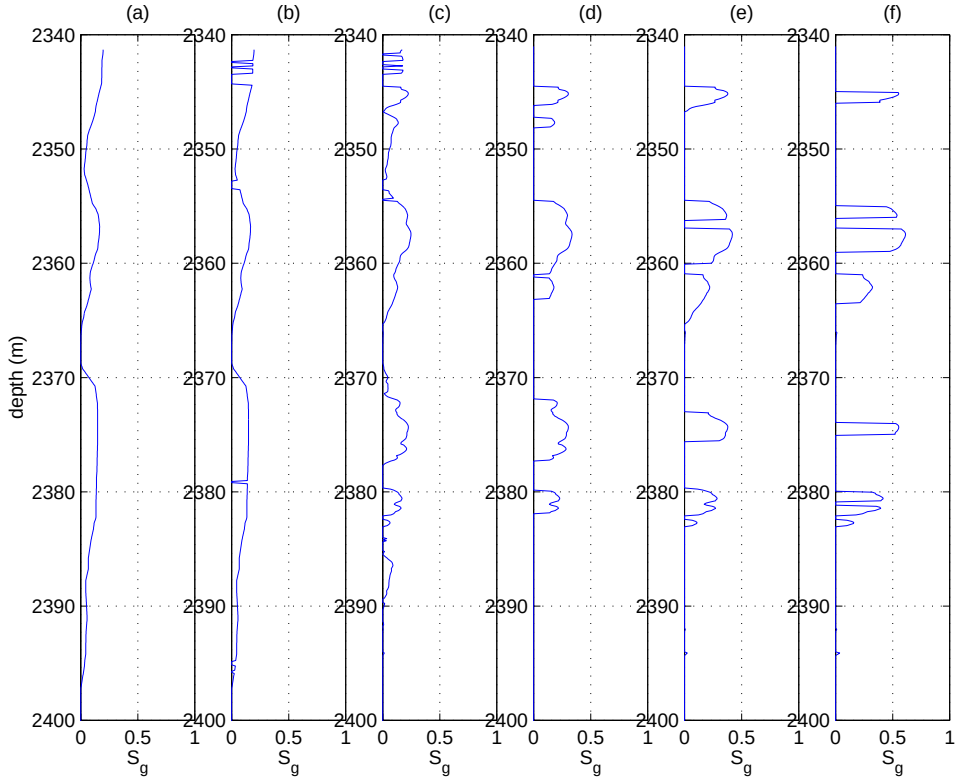

Figure 4.22: Downscaling saturations from the flow simulator: (a): S_g taken from the simulator, (b), (c), (d), (e), (f): Estimations of downscaled S_g.

as we remarked in the previous section. We therefore downscaled the saturations from the simulator using the well log saturations, as shown in Figure 4.22. We assumed that the overall integrated mass balance was reasonably well estimated by the flow simulator output but that the fine-scale distribution of gas was excessively smoothed out spatially.

Figure 4.22 shows the original (smooth) profile of the gas saturation (S_g) taken directly from the simulator, and five estimates of the downscaled S_g, which we computed using the simulator S_g, combined with the initial oil saturation (1-S_w) from well log B. We assumed that the gas is most likely to replace the oil in the high porosity, high permeability sands, which show a high initial oil saturation. From left to right, these saturation profiles show an increasing amount of downscaling. In the downscaling process, we constrained each saturation profile to the total mass of gas (as well as oil and water) predicted by the

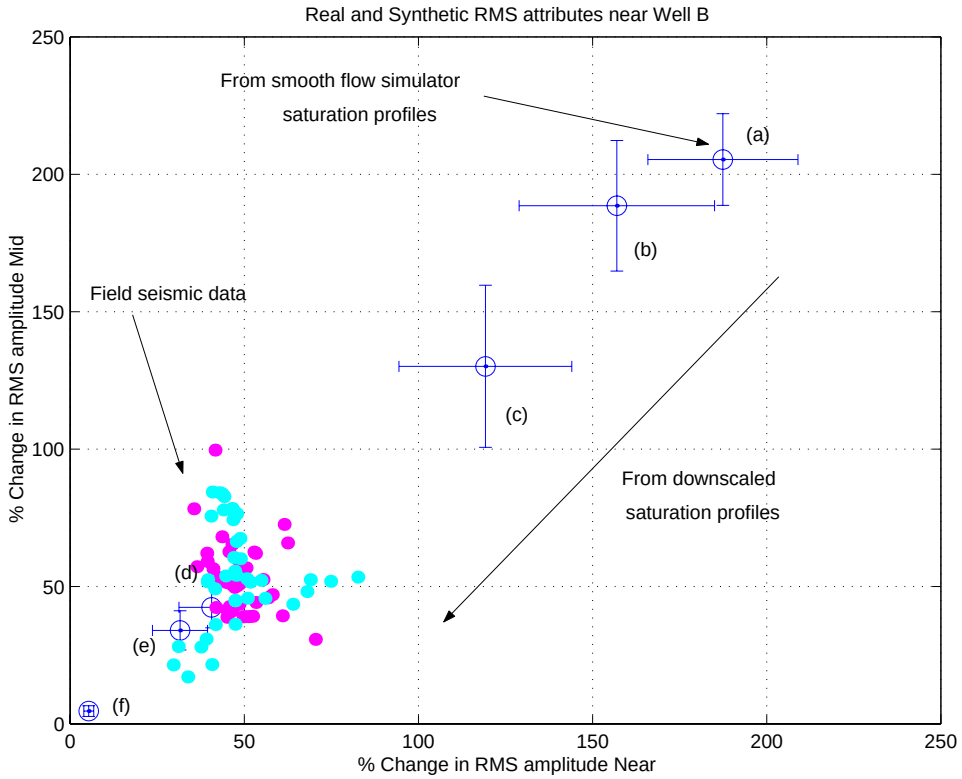

Figure 4.23: Cross plot of time-lapse differential AVO attributes from real data around well B, and from synthetics corresponding to smooth and downscaled saturation profiles. Smooth profiles taken directly from the flow simulator do not match the seismic data. Downscaled models show a much better match.

simulator.

$$\sum_{2400m}^{2340m} S_g \phi \delta t = \sum_{2400m}^{2340m} S_{g_{sim}} \phi_{sim} \delta t_{sim} \tag{4.2}$$

The downscaling can be done using various criteria. The scheme chosen here was as follows. First, zones corresponding to zero effective porosity were set to zero gas saturation in the smooth flow simulator profile. This step gives us profile (b). The assumption here is that there will not be any appreciable gas injection into zones of zero effective porosity. Profile (c) was obtained by scaling profile (b) by the high resolution S_o profile at the well. This is based on the assumption stated above that gas is most likely to replace the oil. Profiles (d) to (f) are obtained by successive hierarchical thresholding of profile (c). These successively downscaled profiles show an increasing amount of patchiness from left to right. The

thresholding can be based on various rock physics parameters such as porosity, V_{shale} or high resolution permeability. Other schemes of downscaling could include spatial spectral domain renormalization or wavelet-transform based multiresolution data fusion.

We performed fluid substitution in well B using the downscaled saturations shown in Figure 4.22. Model (b) corresponds to the simulator saturation profiles but with fluid substitution introducing the vertical roughness in the well porosity. Therefore, fluid substitution is not done at the zero effective porosity regions of the well logs. We observe in Figure 4.23 that honoring the vertical heterogeneity in the well porosity decreases the mismatch between the real and the synthetic seismic. The time-lapse differential AVO attributes for the five downscaled saturations labeled (b), (c), (d), (e), and (f) in Figure 4.23 correspond to the similarly labeled saturation profiles in Figure 4.22. The results for profile (d) capture reasonably well the actual observed seismic signature. Model (f) probably overestimates the amount of patchiness in the saturation.

CALIBRATION AT WELL B

The points in Figure 4.24 correspond to the total gas thickness versus the corresponding synthetic near-offset seismic attribute. Only the models that closely matched the real seismic data and honored the heterogeneity in the well (i.e., the downscaled saturation profiles) were used in this calibration. A linear least square fit, also shown in Figure 4.24 was used to estimate the gas thickness away from well B from the Δ RMS time-lapse seismic atttribute only.

Figure 4.25 shows the gas thickness predicted by the flow simulator along seismic line AB (blue curve), along with the seismic prediction of the gas thickness (thick red curve) along line AB. We notice that the seismic always predicts a lower total gas thickness than the flow simulator. Figure 4.25 shows that the least square estimation of the gas thickness from the seismic predicts a maximum gas thickness of about 39 meters near CDP 20, which corresponds to the location of well A. In this estimation, we did not use any data from well A. We only used the seismic attribute calibrated to modeling in well B. The upper and lower bounds correspond to 2 standard deviations ($\pm$ 7 meters) around the least square estimate.

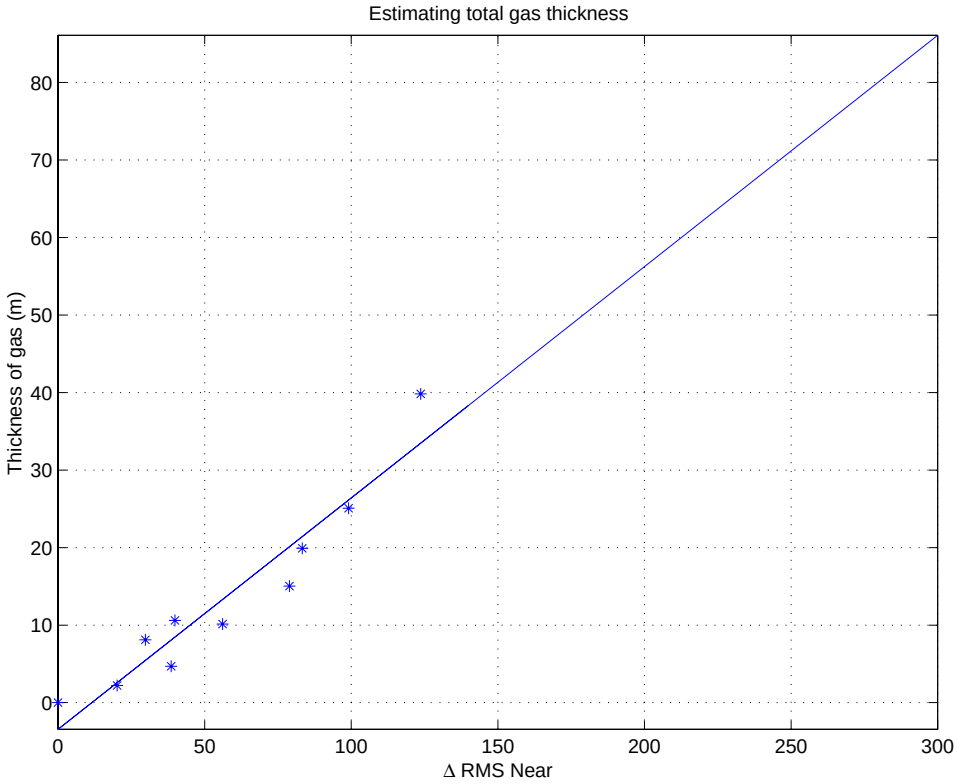

Figure 4.24: Least square regression of total gas thickness from downscaled saturation profiles with the corresponding Δ RMS attributes at well B, used to estimate the gas thickness away from well B.

VALIDATION AT WELL A

Figure 4.26 shows real seismic attributes around well A denoted by dots, and synthetic seismic attributes at well A denoted by the error bars. The pink dots correspond to traces from seismic line AB near well A, and the blue dots correspond to traces from seismic line A near well A.

In this section, we model synthetic seismic attributes using data from well A. We repeated exactly the same procedure as described in the case of well B. However, since V_S was not available in well A, we used a multivariate regression calibrated to well B to generate a V_S log in well A. Using smooth saturation profiles taken directly from the flow simulator, we computed synthetic time-lapse AVO attributes near well A. Figure 4.26 shows

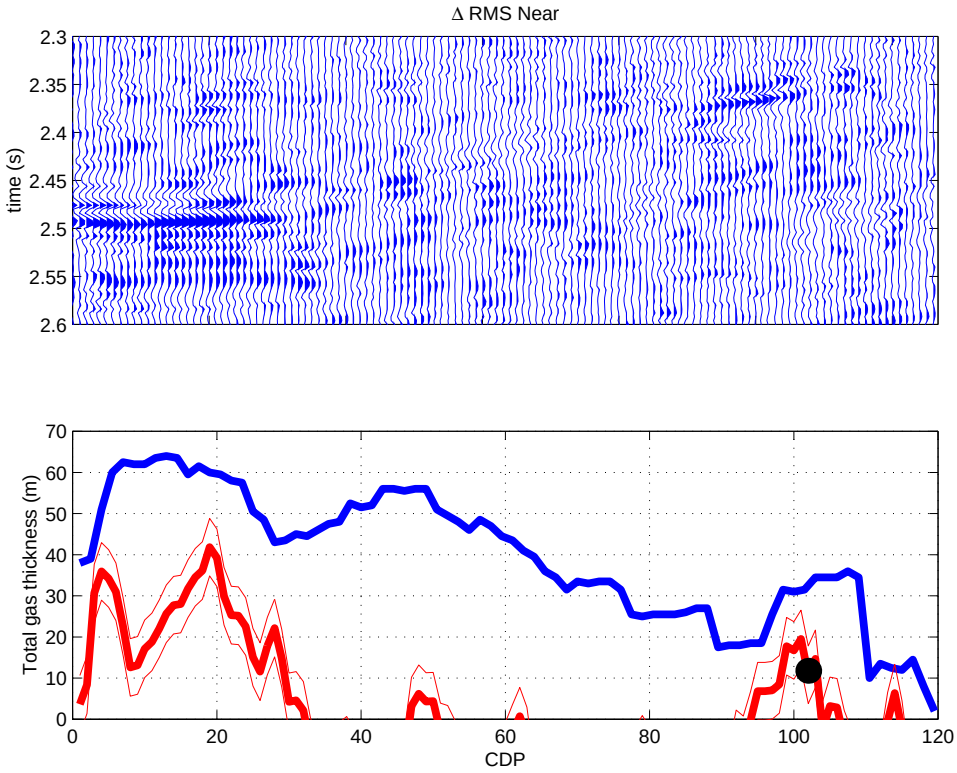

Figure 4.25: Top panel: Near-offset Δ RMS along seismic line AB. Bottom panel: The blue curve represents the simulator-predicted gas thickness along line AB, while the thick red curve represents the gas thickness estimated from the seismic data, calibrated to modeling at well B. The black dot corresponds to the thickness obtained by seismic modeling at well B. The thin red curves correspond to errors in the seismically estimated gas thickness, corresponding to two standard deviations around the linear regression in Figure 4.24.

that as in the case of well B, we obtain a mismatch between real and synthetic attributes when we use smooth saturation profiles taken directly from the flow simulator. Figure 4.21 shows the comparison between the well log data and the flow simulator model. As before, we observe that the flow simulator model is very smooth compared to the well log data, and does not contain the vertical heterogeneity observed in the well logs.

Again, downscaled the saturations to perform fluid substitutions in well A followed by synthetic seismogram modeling. Figure 4.27 shows the downscaled saturations, and Figure 4.28 shows the corresponding real and synthetic seismic attributes of the profiles labelled (a), (b), and (c). Model (b) corresponds to fluid substitution using the simulator saturation

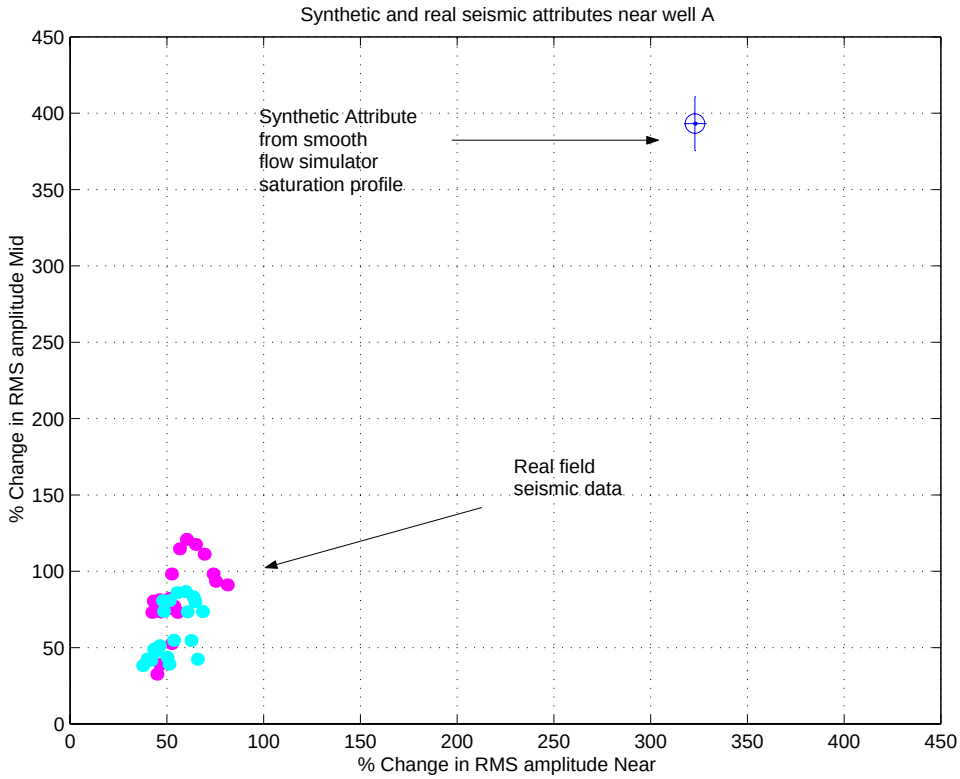

Figure 4.26: Cross plot of real and synthetic time-lapse differential AVO attributes near well A. Note the mismatch between the synthetic and the real data, which may be due to the artificially smooth saturation profiles predicted by the flow simulator.

profiles, but introducing the vertical roughness in the well porosity. This effectively leads to introduction of fine-scale spatial heterogeneity, because the well porosity is much more heterogeneous than the simulator porosity. Model (c) corresponds to downscaled saturation profile using the initial well log S_o.

In well A, honoring the heterogeneity observed in the well porosity has a much larger impact on the seismic response near well A. This is because there is a very large mismatch between the well porosity and the simulator porosity near well A, as seen in Figures 4.20 and 4.21. The downscaled saturation profile (model (c) in Figure 4.27) that best matches the seismic data at well A corresponds to a total gas thickness of 44 meters, which is very close to the gas thickness predicted by the least square estimate calibrated to well B (39 meters). This value of 44 meters is almost equal to the net sand thickness at well A, which is

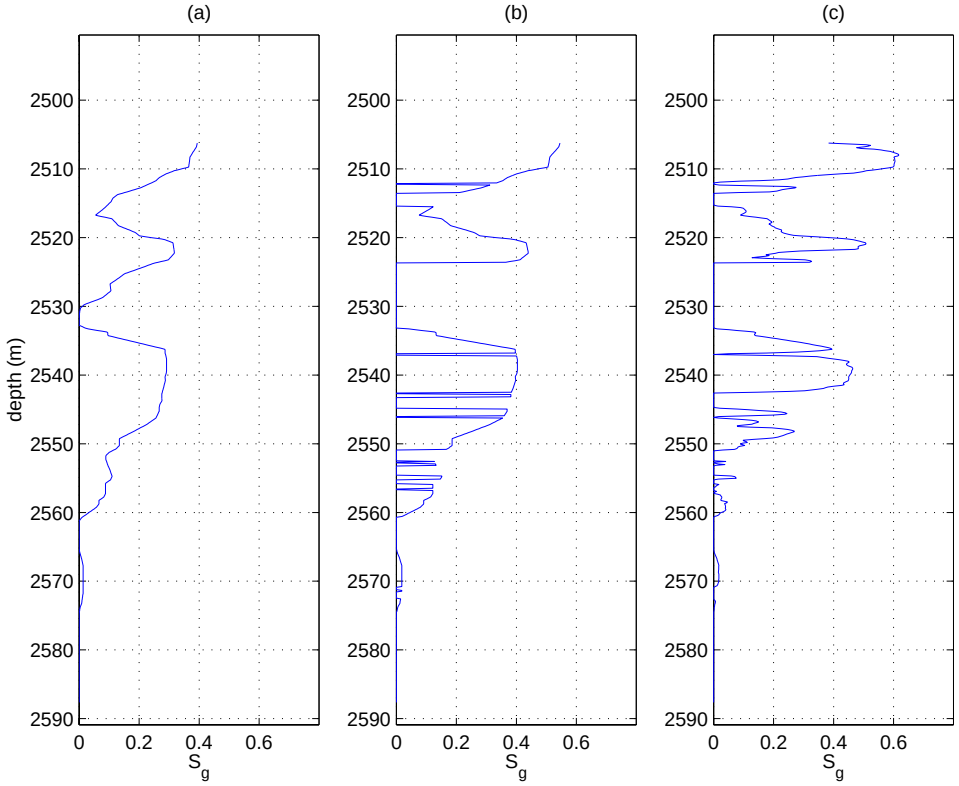

Figure 4.27: Downscaling saturations from the flow simulator: (a): S_g taken from the simulator, (b), (c): Estimations of downscaled S_g.

46 meters. The simulator predicts a thickness of 60 meters at well A which is unreasonable because the total sand thickness is on ly 46 meters. Figure 4.29 shows the validation of the estimated gas thickness at well A. We observe that while the flow simulator predicts a large thickness of gas between wells A and B, the time-lapse seismic predicts that the gas thickness is very low (less than 5 meters) between the wells. This prediction assumes that the heterogeneity between the wells is approximately similar to the heterogeneity at the wells.

CONCLUSIONS

Our goals in this study, as in most time-lapse studies, were to

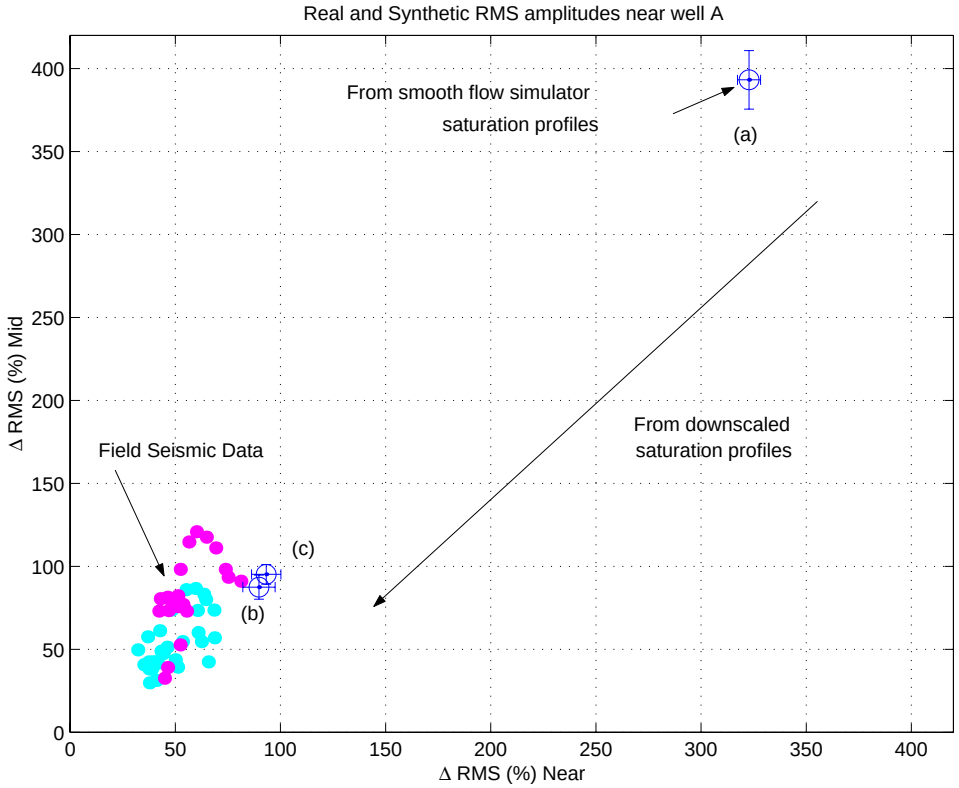

Figure 4.28: Cross plot of time-lapse differential AVO attributes from real seismic data around well A, and from synthetics corresponding to smooth and downscaled saturation profiles.

- link flow simulation with seismic modeling and interpretation
- interpret time-lapse seismic signatures in terms of production-related saturation changes.

From this study, we find that

- a good **qualitative** match exists between simulator predicted saturation changes and observed seismic changes for this dataset
- correct **quantitative** interpretation of time-lapse seismic attributes in terms of saturation changes requires downscaling of the smooth saturations predicted by the flow simulator.

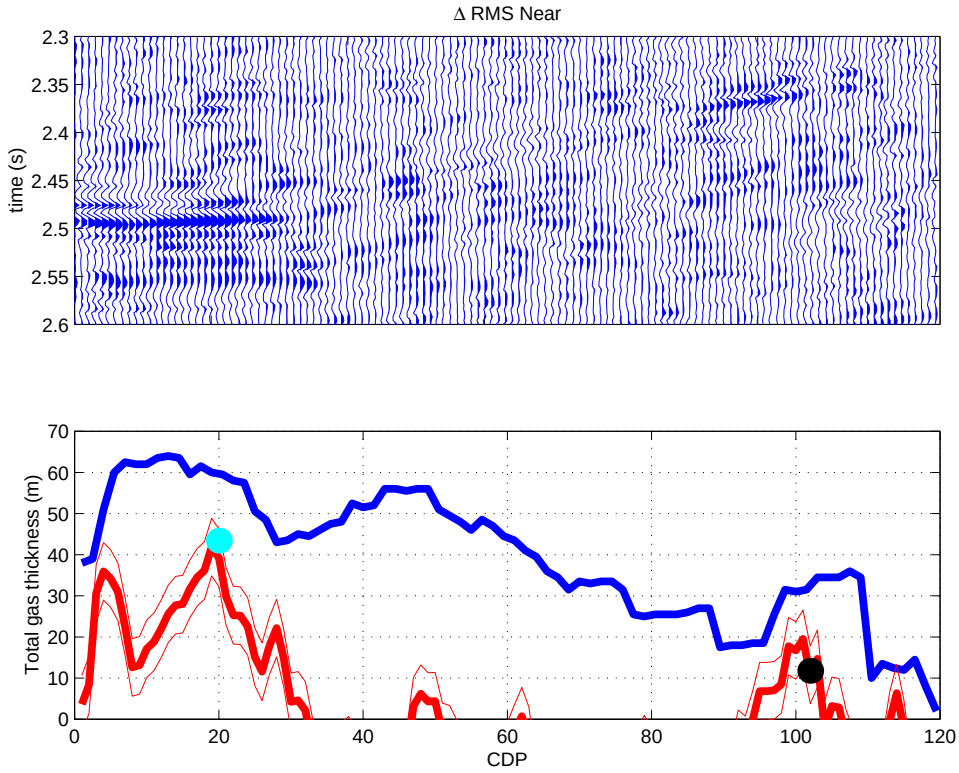

Figure 4.29: Top panel: Near-offset Δ RMS along seismic line AB. Bottom panel: The blue curve represents the simulator-predicted gas thickness along line AB, while the thick red curve represents the gas thickness estimated from the seismic data, calibrated to modeling at well B. The thin red curves correspond to errors in the seismically estimated gas thickness, corresponding to two standard deviations around the linear regression in Figure 4.24. The blue dot shows that seismic modeling at well A yield an estimate of gas thickness that is close to the value predicted from well B.

Fluid substitution, i.e., predicting seismic signatures of saturation changes, definitely is sensitive to the saturation scales. In this exercise we found that downscaling of smooth saturation outputs obtained from the flow simulator to a more patchy distribution was required to provide a good quantitative match to the time-lapse differential AVO signatures, even though the fine details in the saturation distribution were below seismic resolution. Of course, there are many issues in seismic acquisition and processing repeatability that impact amplitudes and their interpretations. Nevertheless, the seismic response is significantly affected by the subresolution saturation heterogeneities which can be estimated from well logs but are not present in the unrealistically smooth flow simulator outputs.

In this monitoring case study, the seismic response enables the estimation of saturation scales which are finer than the flow simulation blocks. This study demonstrates the feasibility of using seismic and well log data to constrain sub-block saturation scales, unobtainable from flow simulation alone. This important result has the potential to significantly impact and enhance the applicability of seismic data in reservoir monitoring. Interdisciplinary integration of *seismic* measurements and *rock physics* with multiphase *fluid flow* helps to reduce uncertainties in sub-resolution spatial fluid distributions, and as a result, reduces uncertainties in interpreting seismic attributes for reservoir management.

APPENDIX: ACOUSTIC IMPEDANCE AND ELASTIC IMPEDANCE FROM INVERSION OF T IME-LAPSE SEISMIC

We inverted the time-lapse seismic data from line AB to obtain impedance sections, shown in Figure 4.30. The impedance inversion was done using a commercial package, and is based on least square minimization and 1-dimensional trace by trace, normal incidence convolutional modeling. We inverted the near offset sections to obtain the before and after acoustic impedances (AI), and the mid offset ($15^o - 20^o$) sections to obtain the before and after elastic impedances (EI). The elastic impedance is a far-offset, angle dependent, impedance like attribute that implicitly includes shear wave information (Mukerji et al., 1998).

The cross plots in Figure 4.31 show the AI and EI from the well logs, plotted along with the AI and EI from the seismic. A good match is observed between the seismic and the log impedances. Well A was not used in the inversion, and yet the seismic impedance around well A shows a good match with the log impedance.

The AI-EI cross plot in Figure 4.32 shows that there is an overall decrease in the impedance due to production in the reservoir zone. Since injection of gas into oil causes a reduction in the seismic impedance, we infer that that gas injection dominates the time-lapse seismic signature. We also observe that the traces near the injector well A show a larger production-related reduction in both the acoustic and elastic impedances, while the traces near producer well B show smaller reduction in the impedances. This is perfectly understandable, at least qualitatively, because there is more gas near the injector well A than near the producer well B.

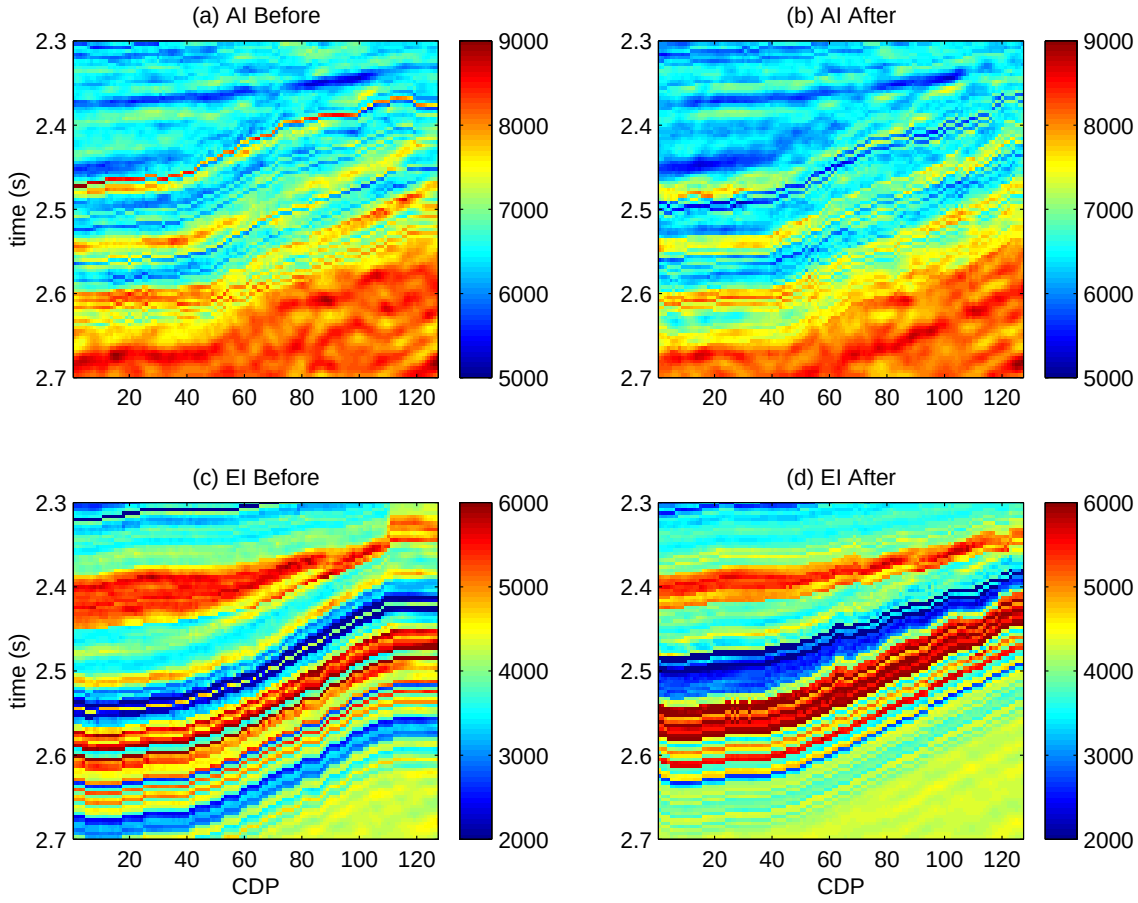

Figure 4.30: Acoustic and elastic impedance sections obtained from impedance inversion of the time-lapse data in line AB.

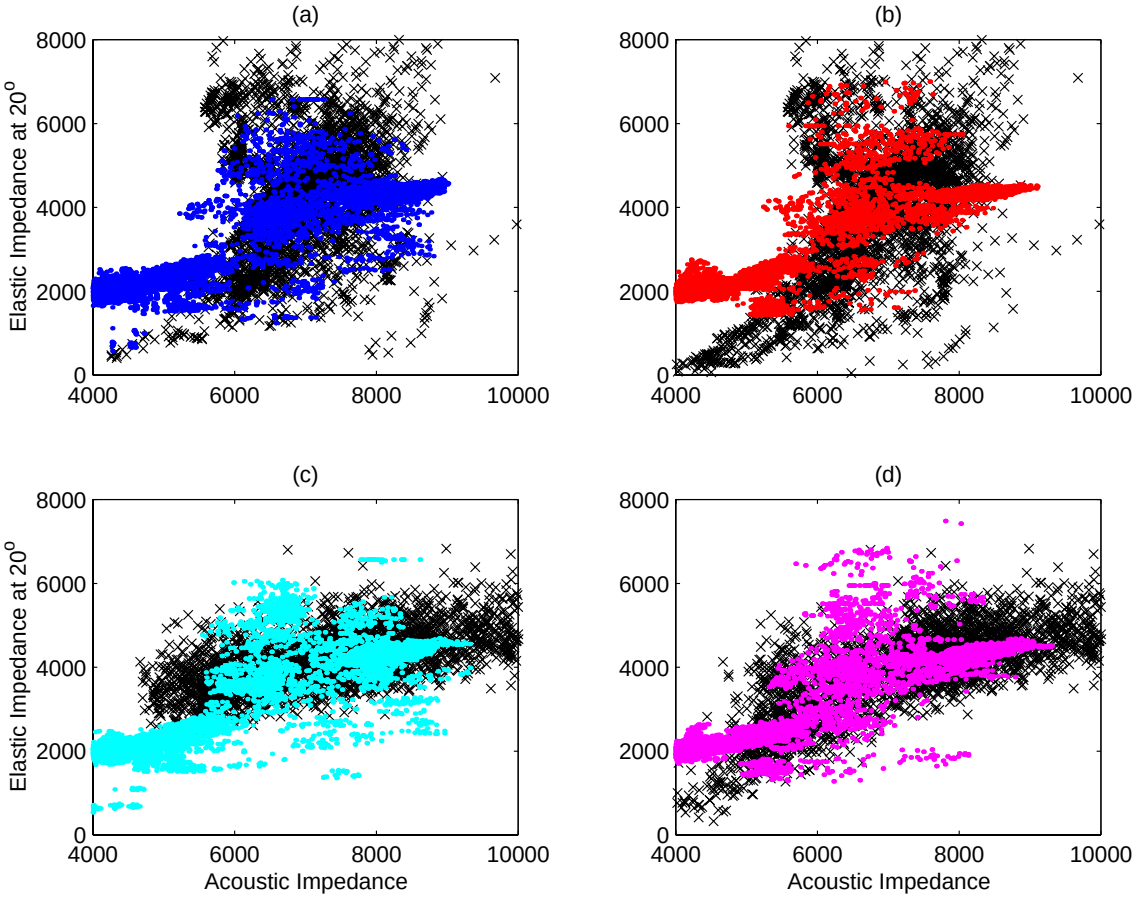

Figure 4.31: Well log impedances plotted along with seismic impedances from line AB. The well impedances are plotted with the black crosses, and the seismic impedances are plotted with the colored dots. (a) Well B, 1983 survey (before), (b) Well B, 1997 survey (after), (c) Well A, 1983 survey (before), (d) Well A, 1997 survey (after). Well log data is available only for the pre-production case. The post-production well log impedances are computed using fluid substitution and saturations from the simulator.

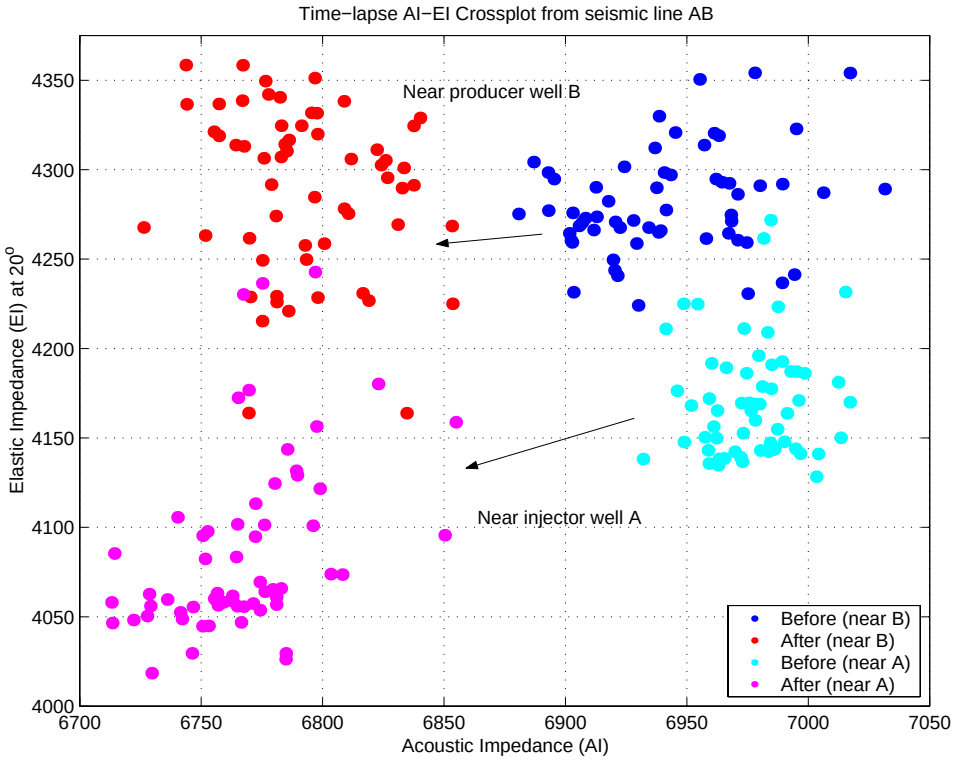

Figure 4.32: Cross-plot of acoustic and elastic impedances (corresponding to Figure 4.30) shows an overall reduction in seismic impedance at the reservoir, indicating that gas injection dominates the time-lapse seismic response.

Bibliography

Akbar, N., Mavko, G., Nur, A., and Dvorkin, J., 1994, Seismic signatures of reservoir transport properties and pore fluid distribution: Geophysics, **59**, 1222–1236.

Aki, K., and Richards, P., 1980, Quantitative seismology: Theory and methods: W.H. Freeman and Co., San Francisco.

Barr, F., 1973, Feasibility study of seismic-reflection monitoring system for underground waste-material injection sites: American Association of Petroleum Geologists Bulletin, **57**, 1591–1592.

Batzle, M., and Wang, Z., 1992, Seismic properties of pore fluids: Geophysics, **57**, 1396–1408.

Batzle, M., 1995, Fluid effects on bright spot and avo analysis: Expanded Abstracts, 65th Ann. Internat. Mtg., Soc. Expl. Geophys., 890–893.

Berryman, J., and Milton, G., 1991, Exact results for generalized gassmann's equation in composite porous media with two constituents: Geophysics, **66**, 1950–1960.

Biot, M., 1956, Theory of propagation of elastic waves in a fluid saturated porous solid. i. low frequency range and ii. higher-frequency range: J. Acoust. Soc. Am., **23**, 168–191.

Brown, R., and Korringa, J., 1975, On the dependence of the elastic properties of a porous rock on the compressibility of the pore fluid: Geophysics, **40**, 608–616.

Cadoret, T., 1993, Effect de la saturation eau/gaz sur les proprétés acoustiques des roches: Ph.D. thesis, University of Paris.

Castagna, J., and Swan, H., 1997, Principles of avo crossploting: The Leading Edge, **16**, no. 4, 337–342.

Castagna, J., Batzle, M. L., and Kan, T. K., 1993, Rock physics – the link between rock properties and AVO response:, *in* Offset-Dependent Reflectivity Soc. Expl. Geophys., Investigations in geophysics, 135–171.

Domenico, S., 1976, Effect of brine-gas mixture on velocity in an unconsolidated sand reservoir: geo, **41**, 882–894.

Duda, R., and Hart, P., 1973, Pattern classification and scene analysis: John Wiley & Sons, Inc., New York.

Dutta, N., and Odé, H., 1979, Attenuation and dispersion of compressional waves in fluid-filled porous rocks with partial gas saturation (white model)–part i: Biot theory, part ii: Results: geo, **44**, 1777–1805.

Dvorkin, J., and Nur, A., 1993, Dynamic poroelasticity: A unified model with the squirt and the biot mechanisms: Geophysics, **58**, 524–533.

Dvorkin, J., Nolen-Hoeksema, R., and Nur, A., 1994, The squirt-flow mechanism: macroscopic description: Geophysics, **59**, 428–438.

Eastwood, J., Lebel, P., Dilay, A., and Blakeslee, S., 1994, Seismic monitoring of steam-based recovery of bitumen: The Leading Edge, **13**, no. 4, 242–251.

Gassmann, F., 1951, $\ddot{U}$ber die elastizit$\ddot{a}$t poroser medien: Vier. der Natur. Gesellschaft, **96**, 1–23.

Geertsma, J., and D.C., S., 1961, Some aspects of elastic wave propagation in fluid-saturated porous solids: Geophysics, **26**, 169–181.

Greaves, R., and Fulp, T., 1987, Three-dimensional seismic monitoring of enhanced oil re covery process: Geophysics, **52**, 1175–1187.

Greenberg, M., and Castagna, J., 1992, Shear-wave velpcity estimation in porous rocks: Theoretical formulation, preliminary verification and applications: Geophys. Prosp., **40**, 195–209.

Gurevich, B., and Zyrianov, V., 1995, Seismic attenuation in finely-layered porous rocks : Cumulative effect of fluid flow and scattering: Expanded Abstracts, 65th Ann. Internat. Mtg., Soc. Expl. Geophys., 874–877.

Han, D.-H., 1986, Effects of porosity and clay content on acoustic properties of sandstones and unconsolidated sediments: Ph.D. thesis, Stanford University.

Hashin, Z., and Shtrikman, S., 1963, A variational approach to the elastic behavior of multiphase materials: J. Mech. Phys. Solids, **11**, 127–140.

He, W., Guerin, G., Anderson, R., and Mello, U., 1998, Time-dependent reservoir characterization of the lf sand in the south eugene island 330 field, gulf of mexico: The Leading Edge, **17**, no. 10, 1434–1438.

Hill, R., 1952, The elastic behavior of crystalline aggregate: Proc. Physical Soc., London, **A65**, 349–354.

Hill, R., 1963, Elastic properties of reinforced solids: some theoretical principles: J. Mech. Phys. Solids, **11**, 357–372.

Hilterman, F., 1998, Rock property framework for comprehending deep-water seismic response, proceedings GSH, 1998 spring symposium, 14th ann. SEG Gulf coast tech. mtg.: SEG, Houston.

Johnstad, S., Seymour, R., and Smith, P., 1995, Seismic reservoir monitoring over the oseberg field during the period 1989-1992: First Break, **May**, 169–183.

Johnston, D., McKenny, R. S., Burkhart, T. D., and Luyties, B., 1998, Time-lapse seismic analysis of the north sea fulmar field: 30th Annual Offshore Technology Conference, Offshore Technology Conference, 93–96.

Kennet, B., 1983, Seismic wave propagation in stratified media: Cambridge University Press, Cambridge.

King, M., 1966, Wave velocities in rocks as a function of change in overburden pressure and pore fluid saturants: Geophysics, **31**, 50–73.

Knight, R., Dvorkin, J., and Nur, A., 1995, Seismic signatures of partial saturation: Expanded Abstracts, 65th Ann. Internat. Mtg., Soc. Expl. Geophys., 870–873.

Lake, L., 1989, Enhanced oil recovery: Prentice-Hall, Inc., New Jersey.

Marion, D., Mukerji, T., and Mavko, G., 1994, Scale effects on velocity dispersion: From ray to effective medium theories in stratified media: Geophysics, **59**, no. 10, 1613–1619.

Mavko, G., and Jizba, D., 1991, Estimating grain-scale fluid effects on velocity dispersion in rocks: Geophysics, **56**, 1940–1949.

Mavko, G., and Mukerji, T., 1998, Bounds on low-frequency seismic velocities in partially saturated rocks: Geophysics, **63**, 918–924.

Mavko, G., and Nolen-Hoeksema, R., 1994, Estimating seismic velocities in partially saturated rocks: Geophysics, **59**, 252–258.

Mavko, G., and Nur, A., 1975, Melt squirt in the asthenosphere: J. Geophys. Res., **80**, 1444–1448.

Mavko, G., Chan, C., and Mukerji, T., 1995, Fluid substitution: Estimating changes in v_p without knowing v_s: Geophysics, **60**, 1750–1755.

Mavko, G., Mukerji, T., and Dvorkin, J., 1998, Rock physics handbook: Cambridge University Press, Boston.

Mukerji, T., and Mavko, G., 1994, Pore fluid effects on seismic velocity in anisotropic rocks: Geophysics, **59**, 233–244.

Mukerji, T., Mavko, G., Mujica, D., and Lucet, N., 1995, Scale-dependent seismic velocity in heterogeneous media: Geophysics, **60**, 1222–1233.

Mukerji, T., Jørstad, A., Mavko, G., and Granli, J., 1998, Near and far offset impedance: Seismic attributes for identifying lithofacies and pore fluid: Geophysical Research Letters, **25**, no. 24, 4557–4560.

Mukerji, T., Takahashi, I., Gonzalez, E., and Mavko, G., 2000, Rock physics diagnistics and modeling of p-p and p-s seismic attributes in the alba field: Expanded Abstracts, 70th Ann. Internat. Mtg., Soc. Expl. Geophys.

MurphyW.F., I., 1984, Acoustic measures of partial gas saturation in tight sandstones: J. Geophys. Res., **89**, 11549–11559.

Nur, A., and Simmons, G., 1969, The effect of saturation on velocity in low porosity rocks: Earth and Planetary Sciences Letters, **7**, 183–193.

Nur, A., Mavko, G., Dvorkin, J., and Gal, D., 1995, Critical porosity: the key to relating physical properties to porosity in rocks: Expanded Abstracts, 65th Ann. Internat. Mtg., Soc. Expl. Geophys., 878.

Nur, A., 1982, Seismic imaging in enhanced recovery: 3rd Joint SPE/DOE Symposium on Enhanced Oil Recovery, 99–109.

O´Connell, R., and Budiansky, B., 1977, Viscoelastic properties of fluid-saturated cracked solids: J. Geophys. Res., **82**, 5719–5735.

Packwood, J., and Mavko, G., 1995, Seismic detection of multiphase fluid distribution in reservoirs: Expanded Abstracts, 65th Ann. Internat. Mtg., Soc. Expl. Geophys., 910–913.

Pullin, N., Matthews, L., and Hirsche, K., 1987, Techniques applied to obtain very high resolution 3-d seismic imaging at an athabasca tar sands thermal pilot: The Leading Edge, **6**, no. 12, 10–15.

Reuss, A., 1929, Berechnung der fliessgrenzen von mischkristallen auf grund der plastizitatsbendingung fur einkristalle: Zeitschrift fur Angewandte Mathematik und Mechanik, **9**, 49–58.

Rutherford, S., and Williams, R., 1989, Amplitude-versus-offset variations in gas sands: Geophysics, **54**, 680–688.

Sengupta, M., and Mavko, G., 1997, Reducing uncertainties in saturation scales using fluid flow models: 1997 fall meeting, Amer. Geophys. Union., 678.

Sengupta, M., and Mavko, G., 1998, Reducing uncertainties in saturation scales using fluid flow models: Expanded Abstracts, 68th Ann. Int. Meeting, Soc. Expl. Geophys., 1012–1015.

Sengupta, M., and Mavko, G., 1999, Sensitivity analysis of seismic fluid detection: Expanded Abstracts, 69th Ann. Int. Meeting, Soc. Expl. Geophys., 180–183.

Sengupta, M., Mavko, G., and Mukerji, T., 1996, Seismic detectability of heterogeneous saturations: 1996 fall meeting, Amer. Geophys. Union., 736.

Sengupta, M., Rai, C., and Sondergeld, C., 1998, Sensitivity studies in forward avo modeling: Expanded Abstracts, 68th Ann. Int. Meeting, Soc. Expl. Geophys., 204–207.

Sengupta, M., Mavko, G., and Mukerji, T., 2000, Integrating time-lapse seismic and flow simulation to map saturation changes: A reservoir monitoring case study: Expanded Abstracts, 70th Ann. Int. Meeting, Soc. Expl. Geophys.

Sonneland, L., Veire, H. H., Raymond, B., Signer, C., Pedersen, L., Ryan, S., and Sayers, C., 1997, Seismic reservoir monitoring on gullfaks: The Leading Edge, **16**, no. 09, 1247–1252.

Thomsen, L., 1993, Weak anisotropic reflections:, *in* Offset-Dependent Reflectivity Soc. Expl. Geophys., Investigations in geophysics, 103–111.

Thomsen, L., 1995, Elastic anisotropy due to aligned cracks in porous rock: Geophysics, **43**, no. 6, 805–829.

Wang, Z., and Nur, A., 1988, Effect of temperature on wave velocities in sands and sandstones with heavy hydrocarbons: SPE, Reservoir Engineering, Soc. Pet. Eng., 158–164.

Watts, G., Jizba, D., Gawith, D., and Gutteridge, P., 1996, Reservoir monitoring of the magnus field through 4-d time-lapse seismic analysis: Petroleum geoscience: Petroleum Geoscience, **2**, 361–372.

White, J., 1975, Computed seismic speeds and attenuation in rocks with partial gas saturation: Geophysics, **40**, 224–232.

Winkler, K., 1983, Frequency dependent ultrasonic properties of high-porosity sandstones: J. Geophys. Res., **88**, 9493–9499.